

INVESTIGATION OF HIGH REYNOLDS NUMBER PIPE FLOW

CoLaPIPE EXPERIMENTS

Von der Fakultät für Maschinenbau, Elektrotechnik und
Wirtschaftsingenieurwesen der Brandenburgischen Technischen
Universität Cottbus-Senftenberg zur Erlangung des akademischen
Grades eines

Doktors der Ingenieurwissenschaften

genehmigte Dissertation vorgelegt von

Diplom-Ingenieur

Franziska König, geb. Zimmer

geboren am 19.02.1983 in Wolfen, Deutschland

Vorsitzende: Prof. Dr.-Ing. habil. Sabine Weiß (BTU C-S, Deutschland)

Gutachter: Prof. Dr.-Ing. Christoph Egbers (BTU C-S, Deutschland)

Gutachter: Assoc. Prof. Alessandro Talamelli (Universita' di Bologna, Italien)

Tag der mündlichen Prüfung: 27.05.2015

Abstract

Investigations of high Reynolds number pipe flow is up to now a great challenge due to the complex mechanisms which appear in pipe flow turbulence. Hence, suitable experimental facilities are necessary to resolve turbulent dynamics and therewith to provide the knowledge for the understanding of such a simple shear flow. For this reason the recent thesis deals with conceptual design and setup of a new high Reynolds number pipe test facility further on named CoLaPipe - Cottbus Large Pipe. It also comprises first investigations on pipe flow obtained from the new CoLaPipe, which can be classified into 1.) calibration measurements to put the facility into service and 2.) continuative measurements to provide experimental results helping to understand pipe flow.

The first results within the CoLaPipe show that this new experimental facility is suitable to investigate turbulence at high Reynolds numbers, where this conclusion can be drawn from intensive investigations on the development length of the flow either for natural and artificial transition. From further experiments on the evaluation of the wall friction velocity using different estimation methods great difficulties and variations in the calculated values are obtained. These deviations are directly related to the scaling behavior of the mean and fluctuating velocity, which is also shown within this thesis and intensively discussed.

Among the discussion of the setup of the new CoLaPipe and the first experimental results this thesis contains a broad literature review with the focus on high and very high Reynolds numbers. Nevertheless, pipe flow at low and moderate Reynolds numbers is described as well.

Kurzzusammenfassung

Untersuchungen an Rohrströmungen bei hohen Reynoldszahlen sind bis heute eine große Herausforderung aufgrund der komplexen Mechanismen die innerhalb turbulenter Rohrströmung auftreten. Daher ist es notwendig geeignete Experimente zu etablieren, um turbulente dynamische Prozesse aufzulösen und somit das Wissen zur Verfügung zu stellen diese vollständig zu verstehen. Aufgrund dessen beschäftigt sich die vorliegende Dissertation mit der Konzeptionierung und dem Aufbau eines neuen Rohrwindkanals mit dem Fokus auf hohen Reynoldszahlen. Diese neue Anlage wird als CoLaPipe bezeichnet, was sich von Cottbus Large Pipe ableitet. Außerdem umfasst diese Arbeit erste experimentelle Untersuchungen und Ergebnisse, die sich unterteilen lassen in 1.) Kalibrationsmessungen zur Inbetriebnahme sowie 2.) weiterführende Messungen.

Die ersten Ergebnisse der CoLaPipe zeigen, dass die neu konzipierte und aufgebaute Anlage geeignet ist um Untersuchungen zur Turbulenz bei großen Reynoldszahlen durchzuführen. Diese Aussage kann anhand intensiver Studien zum Verhalten der Einlaufänge in Rohrströmungen bei verschiedenen Randbedingungen, hier natürliche und erzwungene Transition, bestätigt werden. Weiterführende Experimente zur Bestimmung der Wandschubspannung unter Einbeziehung verschiedener Methoden hat gezeigt, dass an dieser Stelle große Schwierigkeiten und damit Abweichungen der Ergebnisse auftreten. Das wiederum spiegelt sich direkt im Skalierungsverhalten der Hauptströmungs- und Schwankungsgeschwindigkeit wieder, was detailliert in dieser Arbeit diskutiert wird.

Neben der Einführung der neuen CoLaPipe and der Diskussion der ersten Ergebnisse beinhaltet diese Dissertation eine umfassende Literaturrecherche mit dem Fokus auf hohen und sehr hohen Reynoldszahlen. Doch zum Verständnis von Rohrströmungen sind die Mechanismen und Dynamiken der kleinen und mittleren Reynoldszahlen ebenso wichtig und finden daher zusätzlich große Beachtung.

Acknowledgement

I wish to thank, first and foremost, my PhD supervisor Prof. Dr.-Ing. Ch. Egbers. His guidance and scientific support have made this thesis possible. I also gratefully acknowledge Assoc. Prof. A. Talamelli for being the second reviewer. His experience on pipe flow enriches this work in extraordinary way.

Many thanks are to all my colleagues at LAS. Especially, the outstanding technical support, in person of H.-J. Pflanz and H.-J. Wengler. My time at LAS was highlighted as well through the office community with Sandy and Norman Dahley, who were always loyal friends. Thank you for the endless hours spending together and giving me the motivation for further work on this project. Many thanks are to Birgit Futterer, with whom experience my work and mind was always advanced. She is, until now, a role model and the friendly conversations and afternoons together with our families are remaining memories. I also want to thank V. Motuz, T. Seelig, S. Merbold, A. Krebs, F. Zaussinger and Lothar Jehring for their openness with respect to knowledge, technical understanding and helpfulness. Finally, I want to say that it was a great honor for me to work together with El-Sayed Zanoun. He had the challenging idea of building up the greatest pipe flow experiment over the world and he gave me the possibility to accomplish this challenge under his guidance.

To all my friends and companions: many thanks for cheerful hours, trips and barbecue's. It is always a pleasure staying with you even when these times were rare in the past.

An immense part on the success of this work is primarily due to the absolute support and understanding of my beloved parents. They gave me the background for my studies and were always with me during this time taking period of my life. Additionally, I want to thank my little sister Ina for her support whenever I needed it.

Last but by no means least I want to thank my precious husband Mike for the incessantly understanding during our long lasting relation. It was not always easy and funny, but we decided to go together on the same path and I'm sure that we will think this way for the rest of our life. I'm very grateful additionally that we got your little sunshine Paul and Tim. They are the most delightful and incredible presents I have ever got. Thank you my beloved family. You gave and give me the feeling of warmth and love needed to finish this work.

Contents

List of Figures	viii
List of Tables	xi
Nomenclature	xii
Abstract	xv
1 Preamble	1
1.1 Introduction	1
1.2 Motivation	3
1.3 Preliminary Work	5
1.3.1 Experimental Setup	6
1.3.2 Measurement Techniques	6
1.3.3 Results	7
2 Literature Review	10
2.1 The Onset of Sustained Turbulence	12
2.2 Moderate Reynolds Number Range	23
2.3 High and Very High Reynolds Numbers - An Approach to Nature	35
2.4 Numerical Approach to Turbulence in Pipe Flow	39
3 Theoretical Analysis and Background	45
3.1 Governing Equations	45
3.2 General Aspects on Pipe Flow	50
3.2.1 Laminar Pipe Flow	51
3.2.2 Laminar-to-Turbulent Transition	52
3.3 The Structure of the Turbulent Boundary Layer	53
3.3.1 The Viscous Sublayer	55
3.3.2 The Buffer Layer	56
3.3.3 The Logarithmic Region of the Boundary Layer	57
3.3.4 The Outer or Core Region of the Boundary Layer	58

4	The Design Process of the CoLaPipe	60
4.1	Pipe Test Sections	60
4.1.1	Flow Development	62
4.1.2	Surface Roughness	63
4.1.3	Diameter Accuracy	63
4.1.4	Straightness and Alignment	64
4.1.5	Test Pipe Connections	65
4.2	Settling Chamber	66
4.2.1	Inlet Contraction	69
4.2.2	Cooling System	70
4.3	Blower Unit	72
4.4	Final Setup of CoLaPipe	73
5	Measurement Techniques and Data Acquisition System	76
5.1	Pressure Measurements	76
5.1.1	Measurement of Ambient Pressure	76
5.1.2	Measurement of Static Pressure	77
5.2	Temperature Measurement	80
5.3	Velocity Measurements	80
5.3.1	Basic Principal	80
5.3.2	Hot-Wire Calibration	81
5.3.3	Application at CoLaPipe	82
5.4	Data Acquisition	83
5.5	Quantification of Measurement Uncertainties	84
5.6	Determination of Fluid Flow Properties	85
5.7	Accurate Positioning of HWA Probes	88
5.7.1	Application of Optical Method to CoLaPipe	89
6	Results	91
6.1	Boundary Conditions	91
6.1.1	Inlet Flow Conditions	91
6.1.2	Pressure Distribution	93
6.1.3	Transition Scenario	95
6.2	Development Length - Natural Transition Case	97
6.3	Development Length - Artificial Transition Case	100
6.4	Estimation of Wall Shear Stress	105
6.4.1	Mean Pressure Gradient Method	105
6.4.2	Viscous Sublayer Profile Method	109
6.4.3	Clouser Chart Method	112

6.5	Comparison of Different Methods	115
6.6	Mean Velocity Scaling	117
6.7	Scaling of Fluctuating Velocity	121
6.7.1	Spatial Resolution Correction	126
7	Summary and Outlook	129
7.1	Summary	129
7.2	Outlook	130
	References	133

List of Figures

1.1	Overview of recent pipe test facilities.	5
1.2	Schematic setup of preliminary pipe test facility. From [116].	6
1.3	Pipe centerline statistics. From [116].	8
1.4	Presentation of inner scaled mean velocity profiles. From [116].	9
2.1	Osborne Reynolds' revolutionary experiment. From [85].	10
2.2	Experimental results performed by Reynolds [85] in 1883. From [85].	11
2.3	Schematic setup of the long pipe test facility in Manchester. From [36].	12
2.4	A log-log plot of the stability curve. From [36].	13
2.5	Comparison of streak patterns. From [37].	14
2.6	Velocity field of a traveling wave transient for $Re = 3 \times 10^3$. From [38].	15
2.7	Schematic of pipe facility. From [79].	16
2.8	Schematic view of flow control procedure. From [79]	16
2.9	Results regarding reverse transition. From [79].	17
2.10	Schematic setup of the pipe test facility. From [39].	18
2.11	Probability distribution of lifetimes. From [39].	19
2.12	Control mechanism. From [41].	20
2.13	Mean lifetime of a puff before decaying or splitting. From [4].	22
2.14	Mean velocity profiles. From [27].	23
2.15	Variance profiles. From [27].	24
2.16	Higher-order statistical moments for $Re_c = 7 \times 10^3$. From [27].	26
2.17	Axial mean velocity profile as a function of y^+ . From [27].	27
2.18	Pipe test facility for moderate Reynolds numbers. From [21].	28
2.19	Overview of mean velocity profiles. From [21].	28
2.20	Representation of premultiplied spectra for two different scaling. From [53].	29
2.21	Premultiplied spectra for $Re_c = 115.4 \times 10^3$. From [53].	30
2.22	The dimensionless wavelength of the very large-scale motion. From [53].	31
2.23	Schematic setup for "puff splitting" investigations. From [76].	32
2.24	Development of slug for two different Reynolds numbers. From [76].	33
2.25	Development of a puff for two different Reynolds numbers. From [76].	34

2.26	Schematic setup of the SuperPipe. From [108].	35
2.27	Velocity profiles in inner variables. From [110].	36
2.28	Representation of differing scaled mean velocity profiles. From [109].	37
2.29	Recalculation of <i>SuperPipe</i> data. From [67].	38
2.30	Representation of the second-order moment. From [71]	38
2.31	Lifetime distribution for different Reynolds numbers. From [29].	40
2.32	Numerical discovery of traveling wave solutions. From [104].	41
2.33	Numerical results. From [44].	43
2.34	DNS and experimental results for mean velocity profiles. From [106].	44
3.1	General cylindrical coordinate system for pipe flow.	46
3.2	Schematic representation of velocity profiles.	51
3.3	Overview of intermittency factor γ for different Re. From [89] [[90]	52
3.4	Schematic overview of the structure of turbulent boundary layer.	53
3.5	Schematic representation of various boundary layer regions.	54
3.6	Plot of normalized mean velocity profile. From [83].	56
4.1	Sketch of the CoLaPipe.	61
4.2	Surveying devices.	64
4.3	Overview on alignment of sub-construction and blower unit.	65
4.4	Schematic of flange.	66
4.5	Connection of pipe test section through an adhesive bond.	67
4.6	Sketch of the settling chamber.	68
4.7	Numerical simulation supporting the design procedure for the contraction ($Re_m = 13650$).	69
4.8	Cooling system of CoLaPipe.	71
4.9	Centrifugal blower with accessories.	73
4.10	Corners with guide vanes, settling chamber and inlet contraction.	74
4.11	Blower and cooling unit.	74
4.12	Cooling unit with accessories and piping system.	75
4.13	Rear view of the test facility from the blower and cooling unit.	75
5.1	Pipe test section with pressure tapings.	77
5.2	The contraction unit with pressure tapings.	78
5.3	The settling chamber with pressure tapings.	79
5.4	Scheme of CTA.	81
5.5	Details of the ex-situ calibration unit.	82
5.6	HWA calibration curve.	83
5.7	Traverse mechanism with independently moving components.	84

5.8	Schematic wire orientation in the CoLaPipe test section.	85
5.9	Schematic of mirror effect.	89
6.1	Turbulence intensity at pipe entrance.	92
6.2	Velocity profiles at pipe inlet.	93
6.3	Pressure distribution along pipe axis.	94
6.4	Different tripping devices for investigations of air as working medium. . .	96
6.5	Former pipe facility (open wind tunnel).	98
6.6	Development of statistical quantities along pipe test section.	100
6.7	Development of centerline turbulence intensity along pipe test section. . .	102
6.8	Development of centerline skewness factor along pipe test section.	103
6.9	Development of centerline flatness factor along pipe test section.	104
6.10	Development of mean static pressure.	107
6.11	Development of the mean pressure gradient along the pipe test section. . .	108
6.12	First variation of mean pressure gradient.	108
6.13	Second variation of mean pressure gradient.	108
6.14	Third variation of mean pressure gradient.	108
6.15	Fourth variation of mean pressure gradient.	108
6.16	Representation of mean velocity.	110
6.17	Mean velocity profile for $R^+ = 5.25 \times 10^3$	111
6.18	Clausner chart for pipes. From [35].	113
6.19	Clausner chart with CoLaPipe results.	115
6.20	Clausner chart with CoLaPipe results.	116
6.21	Mean velocity profiles for $Re_m = 7.23 \times 10^4$	119
6.22	Mean velocity profiles for $Re_m = 5.7 \times 10^5$	120
6.23	Overview of the raw fluctuating velocity profiles.	122
6.24	Overview of the influence of the wall friction velocity.	124
6.25	Overview of the influence of the wall friction velocity.	125
6.26	Overview of the corrected fluctuating velocity profiles.	128
7.1	Possible arrangement of three x-wire HWA probes.	131
7.2	Detailed view on the HWA probe arrangement.	132
7.3	Alternative HWA probe arrangement using a special equipped part of the pipe test section.	132

List of Tables

1.1	List of all elementary parts of the CoLaPipe.	1
1.2	Overview of present and planned pipe test facilities.	4
2.1	Overview of different shear flows and the limiting Reynolds numbers [41].	21
2.2	Overview of critical points for the sustainment of pipe flow turbulence. . .	21
3.1	Defining properties of wall regions and layers.	55
3.2	Variety of constants κ and B	58
4.1	Physical dimensions of the settling chamber.	68
4.2	Pressure drop through honey.	69
4.3	Summary of calculated pressure losses.	72
5.1	Overview about HWA probe collection.	81
5.2	Uncertainty estimation.	86
5.3	Error propagation.	86
6.1	Overview of exemplary wall shear stress data.	106
6.2	Comparison of wall friction velocity variation.	109
6.3	Overview of exemplary wall friction velocity.	111
6.4	Calculated wall friction velocity u_τ from Clauser chart.	114
6.5	Advantages and disadvantages of different methods.	117
6.6	Results for the wall friction velocity u_τ with different basic principles. . .	117
6.7	List of parameter variation for estimating u_τ	123

Nomenclature

Dimensionless Characteristic Numbers

$k_s^+ = k_s u_\tau / \nu$	Viscous scaled roughness height
L/D	Length-to-diameter ratio
$l^+ = l_w u_\tau / \nu$	Viscous scaled hot-wire length
$l^* = \nu / u_\tau$	Viscous length scale
$R^+ = u_\tau R / \nu$	Kármán number
$Re_c = U_{cl} D / \nu$	Centerline-based Reynolds number
$Re_{crit} = \bar{U}_{crit} D / \nu$	Critical Reynolds number
$Re_m = U_{bulk} D / \nu$	Bulk-based Reynolds number
$Re_\tau = u_\tau D / \nu$	Reynolds number based on wall friction velocity
$t^* = \nu / u_\tau$	Viscous time scale
$\bar{U}^+ = \bar{u} / u_\tau$	Normalized mean velocity
$y^+ = y u_\tau / \nu$	Normalized wall distance

Greek Symbols

Δp	Pressure drop
λ	Friction coefficient
ρ	Fluid density
τ	Decay rate
τ_w	Mean wall shear stress
ν	Kinematic viscosity
μ	Dynamic viscosity
κ	von Kármán constant
γ	Intermittency factor

Superscripts

*	Nondimensional quantity
+	Quantity in wall coordinates

Latin Symbols

A	Cross section
C_f	Friction coefficient
D_{exit}	Exit diameter
D_h	Hydraulic diameter
D_i	Inner pipe diameter
D_{in}	Inlet diameter
f	Friction factor
$F_c(\overline{u'^2})$	Flatness factor
k_s	Sand grain roughness
k_s^+	Equivalent sand grain roughness
L	Length of test facility
L_c	Characteristic length
l_w	Hot-wire length
P	Blower unit power
p_{amb}	Ambient pressure
p_{dyn}	Dynamic pressure
p_{stat}	Static pressure
r	Cylindrical co-ordinate/Cylinder radius
R	Pipe radius
R_{gas}	Universal gas constant
s	Pipe wall thickness
$S_c(\overline{u'^2})$	Skewness factor
T	Temperature
Tu	Turbulence intensity level
Tu_{art}	Turbulence intensity level for artificial transition
Tu_{nat}	Turbulence intensity level for natural transition
t	Observation time
t_0	Constant delay
U	Streamwise mean velocity
\underline{U}	Instantaneous velocity vector
U_{bulk}	Bulk velocity
U_c	Characteristic velocity
U_∞	Free stream velocity
u'	Fluctuating velocity
$\sqrt{\overline{u'^2}}$	Root-mean-square value of fluctuating velocity
u_τ	Wall friction velocity
$\overline{u'v'}$	Reynolds shear-stress
V	Normal/Radial mean velocity
v'	Velocity fluctuation in normal direction
W	Circumferential mean velocity
w'	Velocity fluctuation in circumferential direction

Latin Symbols

x	Streamwise flow co-ordinate
y	Normal flow co-ordinate

Abbreviations

CDF	Cumulative distribution function
CR	Contraction ratio
DNS	Direct numerical simulation
ER	Enlargement ratio
HWA	Hot-wire anemometry
IIT	Illinois Institute of Technology
LAS	Department of Aerodynamics and Fluid Mechanics
LDA	Laser-Doppler anemometry
LDV	Laser-Doppler velocimetry
MTL	Minim Turbulence Level
NDF	National Diagnostic Facility
PDF	Probability distribution function
PIV	Particle image velocimetry
RANS	Reynolds-averaged Navier-Stokes
RPM	Rotation per minute
TBL	Turbulent boundary layer
ZPG	Zero pressure gradient

Abstract

The main content of this thesis is in the field of mechanical engineering with a special subject to fluid mechanics. Hence, it deals with two main parts. One part, which is the basis, is the conceptual design and realization of a large high Reynolds number pipe test facility. This new setup is further on named as CoLaPipe - Cottbus Large Pipe. The second part covers investigations on pipe flow, e.g. velocity and pressure field measurements, under different aspects.

The basic idea behind this project was the support of a highly debated field in fluid mechanics since pipe flow is intensively studied by researchers for almost one hundred and twenty years. A broad literature review with the focus on high and very high Reynolds numbers, but even including low and moderate Reynolds numbers, disclosed the discrepancies between different utilized facilities:

- no clear criterion for a minimum development length,
- challenge of the validity of the universal logarithmic law, and
- scaling behavior of fluctuating velocity,

where these facts are only extracts. With this knowledge and preliminary studies the CoLaPipe was designed for investigations on pipe flow in the field of high Reynolds number turbulence ($Re_m \leq 1.5 \times 10^6$). The different parts of the facility, e.g. test section, contraction and blower, and etc., are presented in detail in this thesis. The application of suitable measuring techniques to resolve the velocity and pressure field is discussed, respectively. At this point the focus is on the possibility of the direct measurement of the wall shear stress u_τ using the mean pressure gradient method. It is believed, that this technique is the most accurate one. The importance of this quantity is due to the definition of the wall friction velocity u_τ :

$$u_\tau = \sqrt{\tau_w / \rho},$$

where τ_w is the wall shear stress and ρ is the density of the working medium. It is even believed that u_τ is a convenient value for the purpose of data normalization. This in turn is a common tool to make measurement results comparable. The direct calculation of u_τ , as in the case of the CoLaPipe, is not obvious, since the pipe test section has to be especially equipped. This can not be realized at every facility. Hence, different methods are established to estimate the wall shear stress τ_w , which are listed in the following:

- mean pressure gradient method,
- viscous sublayer profile method,
- Clauser-Chart-Method and
- exploitation of the viscous sublayer profile method.

To appraise the efforts and improvements among the above listed alternatives this work presents a detailed description of the utilization and an overall comparison. Therewith a rating in between can be developed. But these results have to be considered in the context of the facility possibilities.

Fluid mechanics in a wide context requires a flowing medium, which behavior has to be characterized under certain restrictions and conditions. Within this thesis the fluid is air under ambient boundary conditions, but cooled down to a working temperature in the range of $15^\circ C$ to $21^\circ C$. Independently of the investigated conditions the fluid flow properties have to be calculated accurately. These properties are the fluid flow density and the kinematic viscosity. The calculation of these parameters is well-known. Nevertheless the process is presented in detail. The results can be obtained within an accuracy of less than $\pm 0.5\%$.

The final part of this work composes the analysis of turbulent pipe flow with focusing on the mean and fluctuating velocity profiles, and the characterization of the development of the uniform inlet flow, over laminar to turbulent pipe flow, respectively. In the case of investigating the minimum development length of the flow the focus is on natural as well as artificial transition. The difference in between is on one side the onset of turbulence without any defined disturbances from outside (natural transition), and on the other side the forced laminar-to-turbulent transition where predefined obstacles are applied to the flow at the inlet part of the pipe. In the context of an artificial transition a reduction in the minimum development length is claimed, which is intensively discussed within the present thesis.

1 Preamble

1.1 Introduction

Flow through a circular cross section is one of the simplest experiments, which can be investigated under laboratory conditions. Nevertheless, pipe flow is one of the most challenging ones due to its complexity and versatile applications. This and the fact that there are still a lot of open questions on this topic motivates the recent work, which has a special focus on high Reynolds number pipe flow.

This thesis deals with two main parts, where one is the basis for the other. The first part covers the conceptual design and setup of a new pipe test facility named CoLaPipe, which is discussed in detail in Chapter 4. The given name of the wind tunnel is derived from *Cottbus Large Pipe*. In this case, conceptual design means the description of the overall design study as well as the presentation of every mounted part listed in the following Table 1.1:

Table 1.1: List of all elementary parts of the CoLaPipe.

Chapter	Name of Part	Characteristic	Remarks
4.1	pipe test section	large length-to-diameter ratio	smooth-walled
4.2	settling chamber	/	circular cross section with screens
4.2.1	inlet contraction	numerical validation	polynomial curvature
4.2.2	cooling system	/	purchased part
4.3	blower unit	radial blower	combined module (blower, motor and frequency converter)

An emphasis is placed on the high accuracy assembly of the designed and manufactured parts to minimize inaccuracies, and to enable comparable experimental results supporting fluid mechanics community. The utilized measurement techniques, instrumentation and even the error quantification is presented within Chapter 5.

The second main part of this thesis is discussed in Chapter 6. It covers broad investigations on pipe flow under different boundary conditions. A useful separation between the presented results is 1.) first data sets to put the facility into service and 2.) continuative measurements to answer some of the still open questions. A selection is listed in the following:

1. Accurate positioning of the HWA measurement probe.
2. Exact estimation of the wall friction velocity.
3. Definition and prediction of turbulent flow state.
4. Influence of natural and artificial transition on development of turbulence.
5. Characteristic behavior of mean and fluctuating velocity profile.
6. Scaling behavior of mean and fluctuating velocity at high Reynolds numbers.

The whole work is accompanied by a detailed review on the existing literature (Chapter 2). Here, the focus is not only on high Reynolds number pipe flow. But also on low and moderate Reynolds numbers representing different characteristics, which account for different interests to scientists and engineers. A brief summary of the underlying theory and mathematical background is also presented through Chapter 3.

In conclusion, it can be assert, that the CoLaPipe is a well-working pipe test facility. Therewith it is possible to investigate fully developed turbulence in a circular shaped facility under different boundary conditions at high Reynolds numbers. The results, presented in Chapter 6, demonstrate the high quality and even shed light on some highly debated points. For example, the scaling behavior of the mean flow velocity within the logarithmic layer is found to be not universal. This can be an artifact due to Reynolds numbers inconsistencies. Nevertheless, there are still some open questions, which can be ordinary answered during the future operation of the test facility. One of the most important open questions is the idea behind the structural behavior of high Reynolds number pipe flow with respect to large- and very large-scale motions. Here, only initial numerical and experimental results exist but are not sufficient and satisfying enough [6, 8, 87].

1.2 Motivation

Flows of any kind come along with the humans in every common situation. This can be for example the strong flowing air between houses, which makes it sometimes difficult to walk further on; or it can be the simple flowing system within every peoples bath - the water-tap. Also the weather forecast would not be that sufficient if the scientists behind it have had no or pure knowledge about the flows in the oceans and clouds. Even the flow in piping system for energy supply, e.g. cold and hot water and air, are flow systems, which are common and transport the medium through circular shaped tubes. The flow geometry behind is a pipe, which is on one side simple and on the other challenging. Also in larger dimensions pipe flow is the preferred system to transport fluids of any kind. Here, the transportation process of oil and gas over more than thousand kilometers, as in the *Druschba pipeline*, which is the connection from east Russia to Germany, is no curiosity. Hence, it is not particular that pipe flow acts as a well known model for shear flow and its instabilities, due to the importance in technical applications for more than 120 years. In addition to the aforementioned applications pipe flow phenomena are also present in automotive engineering and air conditioning technology, and hence a detailed knowledge on it is important for this kind of industry.

The pioneering work of Reynolds [85] is the beginning of an outstanding interest on the knowledge of the dynamics within pipe flow. Several researchers inspired by him pick up his discoveries, like Nikuradse [74] and Laufer [57], who are only a selection, and extend the overall background on fluid mechanics in particular pipe flow. Nevertheless it persists until now the necessity to investigate this kind of wall-bounded flow because of the immense practical relevance, which is still increasing due to more and more complex systems, e.g. to solve economic and environmental requirements, especially in the case of high Reynolds number turbulence as well as the qualitative physical understanding of the transition process. To get as close as possible to the answers of all the open questions different test facilities with circular cross section exist or are planned (refer to Table 1.2).

Table 1.2 lists physical dimensions of test facilities, where Re_m is the bulk-based Reynolds number, L/D is the length-to-diameter ratio and D_i is the inner diameter of the test section. In all cases air under ambient conditions is used as working fluid except in the Princeton SuperPipe, where additionally pressurized air is applied to the system to reach the maximum laboratory Reynolds number.

The non-dimensional factor L/D is very important evaluating facilities with respect to the full development of turbulence. Patel and Head [78] as well as Zanon et al. [116] claim a minimum developing length of about $70 D$. With this consideration all presented facilities in Table 1.2 provide the basis for intensive investigations on fully developed

Table 1.2: Overview of present and planned pipe test facilities contributing to high Reynolds number turbulence in pipe flow.

	Re_m	L/D	D_i	working fluid
CICLoPE (Forlì)	$4.0 \times 10^4 - 2.0 \times 10^6$	100	0.90 m	air
CoLaPipe (Cottbus)	$4.0 \times 10^4 - 1.5 \times 10^6$	148	0.19 m	air
CoLaPipe (return line)	$2.3 \times 10^4 - 6.0 \times 10^5$	79	0.342 m	air
Zanoun et al. [116]	$3.0 \times 10^4 - 1.0 \times 10^5$	187.5	0.032 m	air
SuperPipe (Princeton)	$3.0 \times 10^4 - 3.5 \times 10^7$	200	0.129 m	air

turbulent pipe flow. Even the transition process from laminar to turbulent without triggering the flow artificially - natural transition - can be investigated using the presented facilities.

In addition to Table 1.2 Figure 1.1 is depicted, which is in a similar way shown in Talamelli et al. [96], to give an access to the facilities turbulence resolution. Even the main difference and limitations of the pipe experiments are demonstrated. Figure 1.1 represents ranges of capabilities of various pipe facilities in terms of the wall turbulence length scale, $l^* = \nu/u_\tau$, as a function of the Kármán number ($R^+ = u_\tau R/\nu$), where u_τ is the wall friction velocity, R is the pipe radius and ν is the kinematic viscosity.

The figure points out the spatial resolution limitations ($0.3 \leq l^* \leq 25$) of the Princeton SuperPipe in spite of the large achievable Reynolds number range, see also Talamelli et al. [96]. This is also marked by the green dashed line, which characterizes the minimum sufficient spatial resolution when using the common HWA measurement technique. Compared to the SuperPipe the other two presented facilities, i.e. CoLaPipe and CICLoPE, provide an adequate spatial resolution within the range of $10 \leq l^* \leq 100$. Especially the CoLaPipe allows measurements with high spatial resolution ($100 \leq l^* \leq 300$) utilizing the return line for a Kármán number range of $500 \leq R^+ \leq 2000$. The return line has an inner diameter of 340 mm that permits also enough separation between the inner and outer scales to study the desired characteristics of turbulence. Even labeled within Figure 1.1 are some important values concerning numerical procedures to support the ongoing discussion in the field of pipe flow turbulence. Here, the brown dashed line represents the actual maximum achievable Reynolds number utilizing DNS obtained by Wu and Moin [106]. But it is a great request among all related researchers either experimentalists or computational scientists to enhance the lower limit beyond $R^+ = 5000$ [44, 106]. This purpose is marked by the blue dashed line. The black dashed line shows the starting point for very high Reynolds number turbulence. And it is obvious from Figure 1.1 that this is hard to realize since the physical laboratory space is limited everywhere. With one exception, CICLoPE will provide access to very high Reynolds number

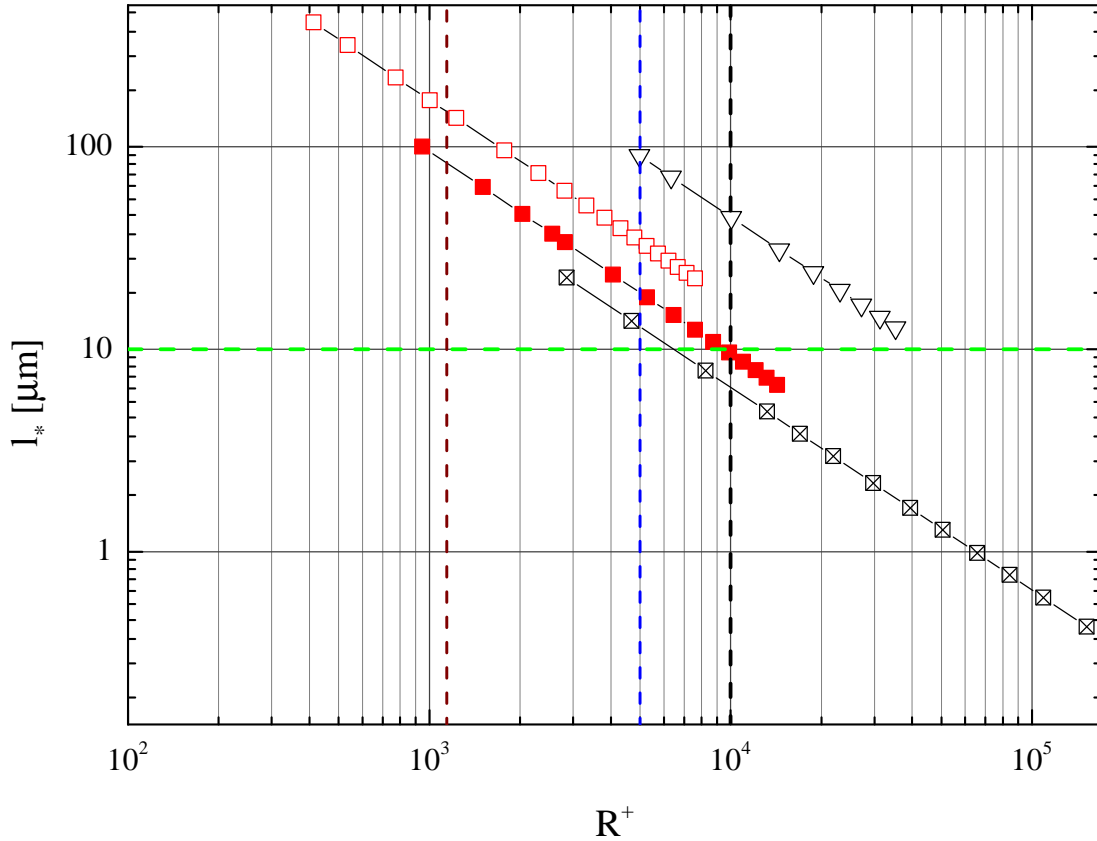


Figure 1.1: Overview of recent pipe test facilities relating the viscous length l^* to the Kármán number R^+ . \boxtimes Princeton SuperPipe; \blacksquare CoLaPipe; \square CoLaPipe return line; ∇ CICLoPE; $---$ minimum for sufficient spatial resolution; $---$ highest Reynolds number for DNS, $R^+ = 1142$ [106]; $---$ future Reynolds number for DNS; $---$ start of very high Reynolds number turbulence

turbulence, but is restricted to the resulting spatial resolution ($10 \leq l_* \leq 60$).

1.3 Preliminary Work

Investigations on pipe flow have a long tradition, and hence detailed results on this topic exist. Nevertheless, in preparation for the setup of the CoLaPipe test facility preliminary results are established using another test facility, which is described in detail elsewhere [116]. These results contain information on the transition behavior and the development length utilizing the evolution of statistical quantities along the pipe axis. The main difference between these preliminary results and the those presented within this thesis is the diverging Reynolds number range. The preliminary work is conducted for moderate Reynolds numbers ($Re \leq 106 \times 10^3$), whereas the CoLaPipe is mainly designed for

investigations on high Reynolds numbers turbulence.

The following chapter is about a brief description of the constructive setup of the preliminary used facility and the applied measurement techniques. In conclusion, the main results with the focus on the development length are presented.

1.3.1 Experimental Setup

The laboratory of the Department of Aerodynamics and Fluid Mechanics, BTU Cottbus-Senftenberg, maintains a high quality aero-acoustic test facility. It is an open wind tunnel with a free jet at the exit of the nozzle, i.e. no direct feedback. Air with a maximum velocity of 60 m/s is provided by a radial blower. This configuration, depicted in Figure 1.2, yields a centerline turbulence intensity of less than 0.35 %. To realize the main aim a test section with circular cross section of $D_i = 0.032$ m and a total length of $L = 6$ m is connected to the nozzle exit, referred as to *Pipe test section* in Figure 1.2. This provides a length-to-diameter ratio of $L/D = 187.5$.

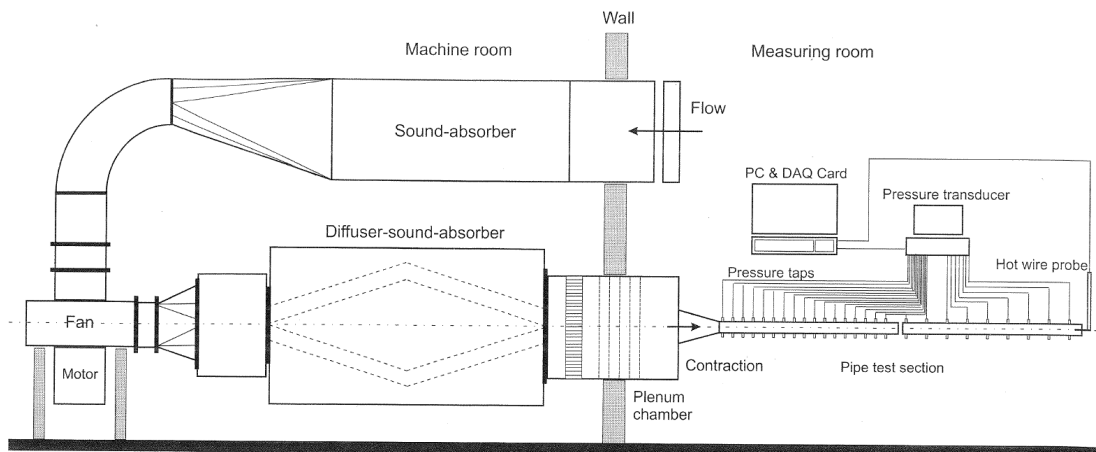


Figure 1.2: Schematic of the aero-acoustic test facility at the laboratory of the Dept. of Aerodynamics and Fluid Mechanics with adapted circular cross section and measurement techniques. From [116].

1.3.2 Measurement Techniques

To indicate the flow field within the pipe test facility different measuring techniques are applied. For information on the velocity, here mean and fluctuating velocity as well as bulk velocity, two independently working systems are installed. One is a LDA system for the wind tunnel calibration and the measurement of U_{bulk} ; and the other is a HWA

system collecting the mean and fluctuating velocity along the pipe axis. The local mean static pressure is captured through static pressure holes. They are distributed equally spaced along the axis and therewith provide sufficient information on the streamwise pressure gradient. The results of these intensive measurements are presented within the next chapter.

1.3.3 Results

The results obtained by Zanon et al. [116] highlight several different aspects. Therefore the focus is only on those, which have a direct feedback on the design concept of the CoLaPipe.

The limited laboratory space and the fact, that most of the literature results are inconsistent, like [57, 74, 78, 80] and [108], have motivated the intensive measurement series prior to the completion of the CoLaPipe concept. One main point is the identification of fully developed turbulence under natural transition conditions. For this aim different approaches are available and well known, but no clear criterion could be defined through the years. Hence, the flow field within the pipe is investigated for different initial conditions, e.g. varying Reynolds numbers. At this phase of the measurements the focus is on the evolution of the statistical quantities at the centerline of the test section to detect the transitional regime within the setup. Additionally, the turbulent flow state is identified and gives answers on the necessary length to achieve this flow state. These information obtained from the centerline turbulence statistics are plotted as a function of the dimensionless pipe length x/D ¹. The resulting data are presented in Figure 1.3. The tendency, which can be extracted from this figure, is that after a development length of nearly $x/D \approx 70$ the turbulent flow state is achieved. This is indicated through the invariant behavior of the statistical quantities, which means that they approach a constant value and persists with increasing x/D . For the design considerations of the CoLaPipe it denotes that at least $x/D = 100$ is required to investigate turbulence under natural conditions. The realization depends on the chosen pipe diameter, which can be a limiting property with respect to the spatial resolution. This relation will be discussed in detail in Chapter 4.

The work of Zanon et al. [116] supports also the debate on the correct scaling of the mean velocity profiles with the presentation of certain profiles for a sufficient range of R^+ . The most important results are presented in Figure 1.4, where the normalized mean

¹Note, that within numerical results the dimensionless pipe length is defined as x/R .

²Remark: The used nomenclature u'_c represents the root-mean-square value of the fluctuating velocity at the centerline of the pipe. Hence, u'_c equals $\sqrt{u'^2}$. This is also valid for the used nomenclature $S_c(u')$ as well as $F_c(u')$.

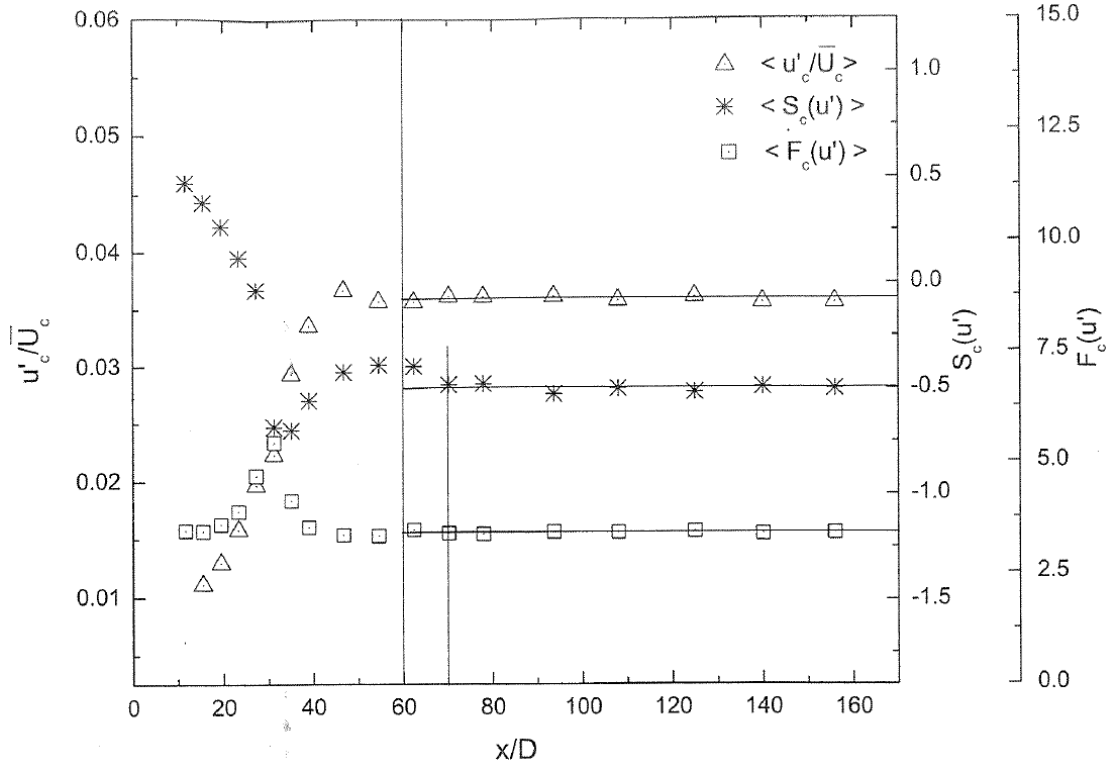


Figure 1.3: Pipe centerline statistics as a function of the normalized pipe length for no tripping². From [116].

velocity is shown as a function of the normalized wall distance scaled on inner variables. The diagram shows, that the curves collapse onto one single curve and yield a good agreement with some literature results in the logarithmic region of the boundary layer. Nevertheless, this figure shows a clear deviation of the mean velocity for $y^+ \geq 150$ - a so called velocity overshoot. It is supposed by the authors that this is a possible effect due to the low Reynolds number range or it can be interpreted as the existence of a local power law. Similar results are obtained by McKeon et al. [66].

For further information one can review the results obtained by [116]. Additionally, Chapter 6 deal with a more precise interpretation of this topic.

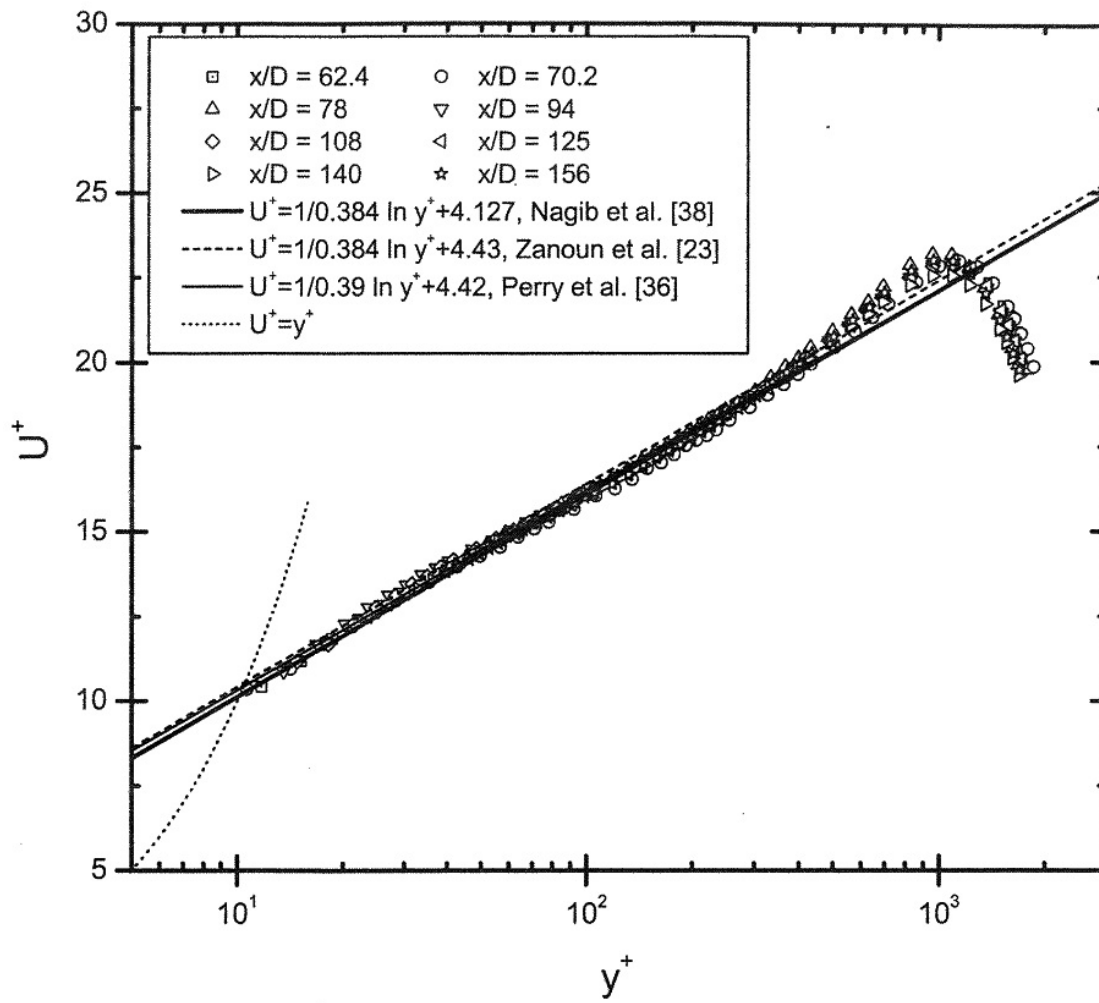


Figure 1.4: Presentation of the inner scaled mean velocity profiles for $1040 \leq R^+ \leq 1140$ and for different literature results. From [116].

2 Literature Review

As mentioned before, pipe flow is one of the most intensively investigated types of wall-bounded flows due to its immense practical relevance, e.g. in automotive and shipping industry. It also seems that pipe flow is of infinite complexity, and is therefore still a highly discussed field in fluid mechanics. The interest on this field of fluid mechanics has a long history starting with the pioneering experiments of Reynolds [85]. His investiga-

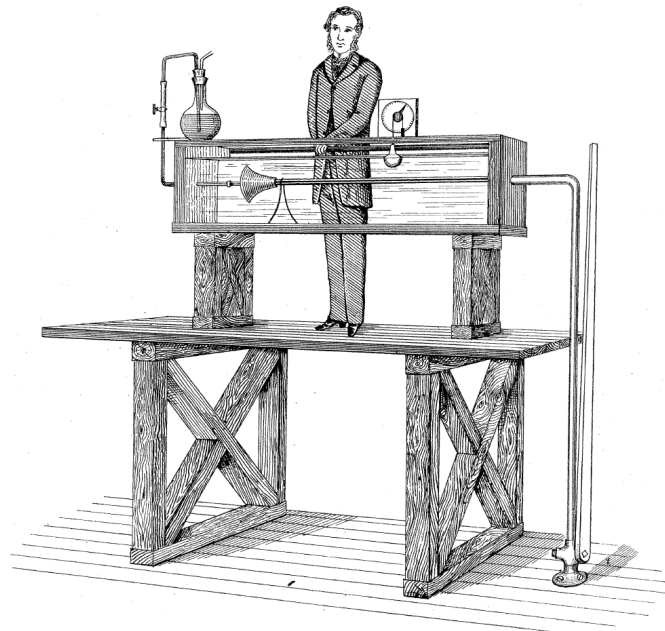


Figure 2.1: Osborne Reynolds' revolutionary experiment. From [85].

tions on fluid motion in glass tubes with water as the working fluid (see Figure 2.1) made it possible to observe “two broadly distinguishable forms - either the element of the fluid follow one another along lines of motion which lead in the most direct manner to their destination, or they eddy about in sinuous paths the most indirect possible ” [85]. These fundamental results are obtained investigating the effects of different velocities along tubes visualized using colored water. For sufficiently low velocities Reynolds observed a constant colored streak through the pipe, which is illustrated in Figure 2.2a. During the increase of the inlet velocity the colored water began to mix up with the surrounding

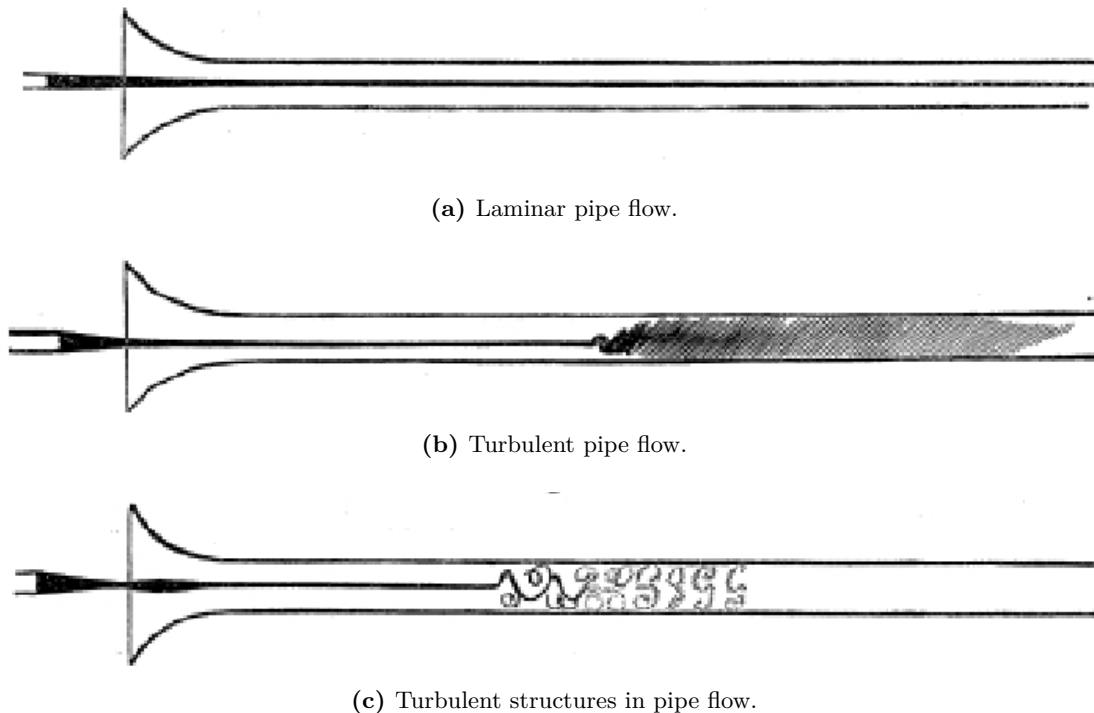


Figure 2.2: Experimental results performed by Reynolds [85] in 1883. From [85].

water after a certain distance from the entrance. The result is completely filled tube, which is schematically depicted in Figure 2.2b. A steady increase in the velocity up to the maximum caused the mixing point to move upstream, but it never reached the inlet of the tube. These observations together with his theoretical considerations gave scientists the understanding of the commonly known laminar and turbulent flow. Another fundamental result from this simple but at the same time very effective experiment is the observed relation between the inertial and viscous force, which is since then well-known as the Reynolds number

$$Re = \frac{\textit{inertial force}}{\textit{viscous force}} = \frac{\rho L_c U_c}{\mu} = \frac{L_c U_c}{\nu},$$

where L_c is a characteristic length, U_c is a characteristic velocity, ρ is the density of the working fluid, μ is the dynamic viscosity and $\nu = \mu/\rho$ - the kinematic viscosity of the working fluid. This non-dimensional relation gives scientist the possibility to investigate pipe flow under different conditions, and compare the results, anyway.

A detailed literature review on the historic development of pipe flow is among others presented by Zagarola [108]. In the following chapter the focus is on some selected references, which are confined through different ranges in the Reynolds number.

2.1 The Onset of Sustained Turbulence

From theory we know that pipe flow is linear stable and hence laminar. Contrarily, in most practical and experimental applications the turbulent flow state is achieved even for lower Reynolds numbers. This is a well-known paradox, which is the subject of various experiments and numerical analysis during the last decade. In conclusion, it is obvious to assume that this phenomenon is caused by finite amplitude perturbations, which propagate through the flow.

An important step to the understanding and useful exploitation of this problem comes from Hof et al. [36]. The scientists try to answer the following question:

..., if $\epsilon = \epsilon(\text{Re})$ denotes the minimal amplitude of all finite perturbations that can trigger transition, and if ϵ scales with Re according to

$$\epsilon = O(\text{Re}^\gamma)$$

as $\text{Re} \rightarrow \infty$, then what is the exponent γ ? [36]

They anticipate a negative value of γ indicating an increase of the sensitivity of the laminar flow with increasing Reynolds number. To relate this theoretical concept to experimental observations they conduct their experiments in two pipe facilities depicted in Figure 2.3. The related description of the facility as well as the utilized boundary conditions are presented elsewhere [19, 36]. These extensive investigations uncover the

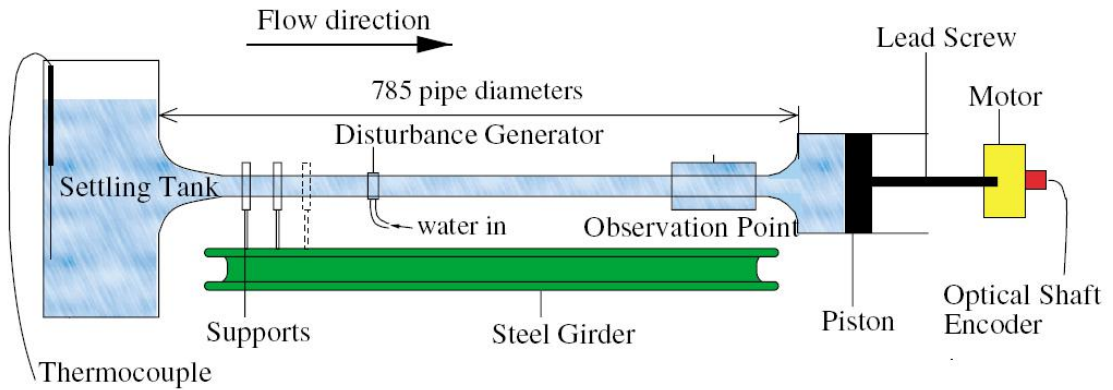


Figure 2.3: Schematic setup of the long pipe test facility at the *Manchester Center for Non-linear Dynamics, University of Manchester, United Kingdom*. Reprinted with permission from [B. Hof, A. Juel, T. Mullin, *Physical Review Letters*, 91(24):4, 2003.] Copyright 2003 by the American Physical Society.

exponent to be $\gamma = -1$ and give clear experimental evidence for the scaling behavior

depicted in Figure 2.4.

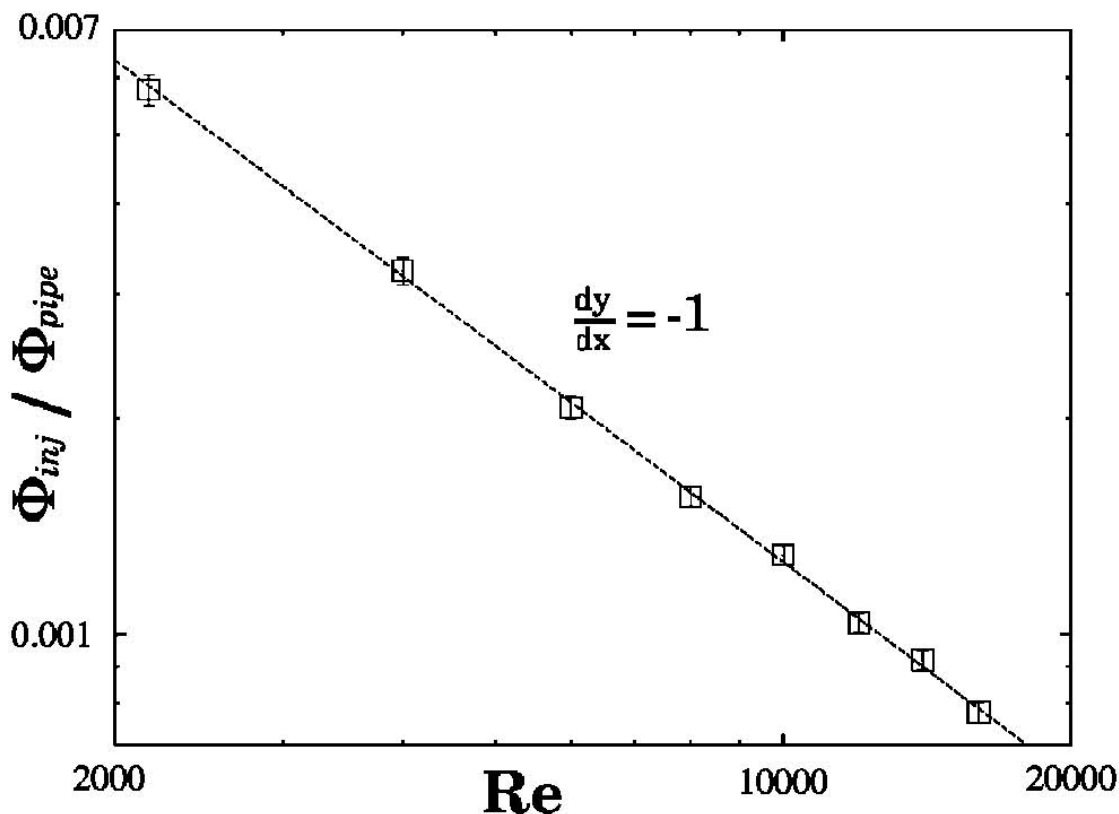


Figure 2.4: A log-log plot of the stability curve with respect to the non-dimensionalized amplitude of the perturbation and the Reynolds number covering a range of 2000 to 18000. The line shows a slope of -1 ± 0.01 . Reprinted with permission from [B. Hof, A. Juel, T. Mullin, *Physical Review Letters*, 91(24):4, 2003.] Copyright 2003 by the American Physical Society.

The governing equations in the field of pipe flow are the Navier-Stokes equations discussed in Chapter 3. This set of equations describe the fundamental theory and is a challenge regarding numerical predictions, which are very useful and important due to the comparison with experimental results. Several scientists focus on solving the equations or deriving solution statements [28, 52, 53, 100]. A deeper discussion on the hitherto existing efforts as well as future aims can be found in Chapter 2.4. Hof et al. [37] intend to fill the gap between previous numerical findings and the missing experimental evidence of traveling waves relevant for turbulence in pipe flow. These traveling wave solutions found throughout numerical simulations [34, 100–103] contain important structural features, namely streamwise vortices and streaks. To investigate this self-sustaining process experimentally Hof et al. [37] applied their measurements to the before mentioned experimental facility [19, 36]. An operating high-speed stereoscopic particle image velocimetry system enables the access to observe flow structures.

Therewith they detected different symmetric traveling waves C_m for different adjusted Reynolds numbers, and compared these experimental results with the previous found numerical solutions, refer to Figure 2.5. The accordance between the experimental and

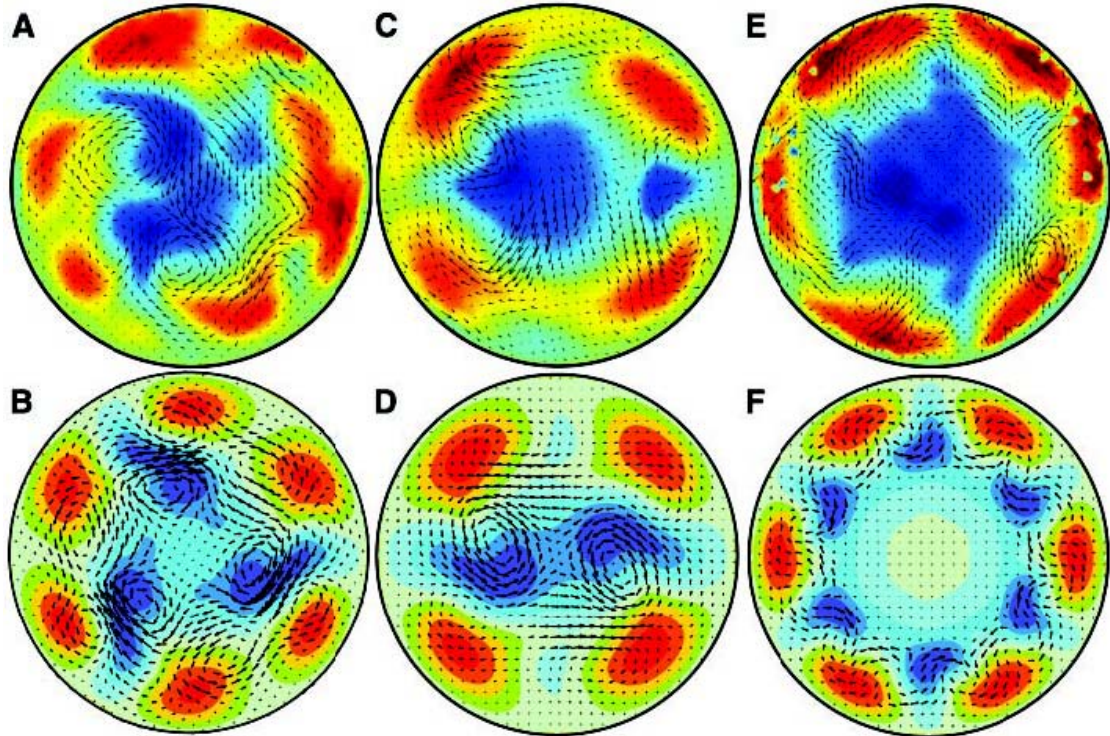


Figure 2.5: Comparison of experimentally (top) and numerically (bottom) observed streak patterns. From [37]. Reprinted with permission from AAAS.

numerical observations are evident, and

support a theoretical scenario in which the turbulent state is organized around a few dominant traveling waves [37].

In addition, these results are consistent with dynamical system theory and show that the concepts can account for a better understanding of turbulence, respectively. The insight into the dynamics and symmetry of streaks enables further improved research on turbulence and chaos control.

This above described mechanism of a traveling wave solution is investigated in more detail by Hof et al. [38]. Here, a fully developed laminar flow at $Re = 3 \times 10^3$ is disturbed using a water jet perturbation system. The result is a localized turbulent structure called slug (refer to [107]), which is moving in downstream direction and observed with a stereoscopic PIV-system. The achieved velocity fields in the cross-sectional plane of the pipe test facility are shown in Figure 2.6 yielding the characteristics for a traveling wave [38]. The dynamical behavior behind these observations is in excellent agreement

with the reported results from numerical investigations by Faisst and Eckhardt [28] and Wedin and Kerswell [104]. In conclusion the authors state that these findings are of great relevance with respect to transition and energy regeneration in shear flows.

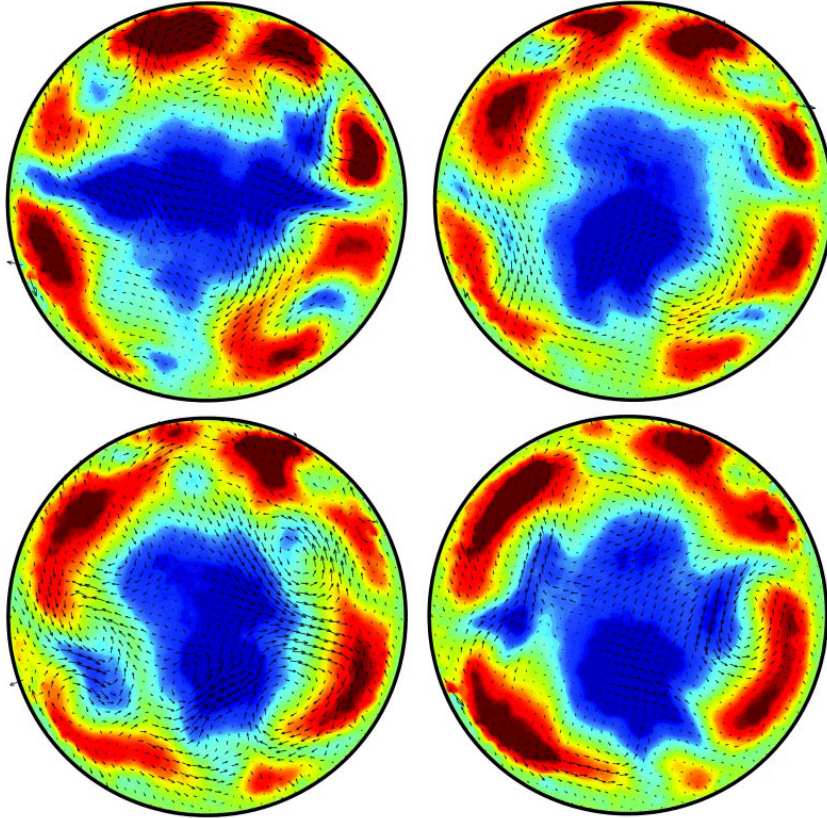


Figure 2.6: Velocity field of a traveling wave transient for $Re = 3 \times 10^3$. Reprinted with permission from [B. Hof, C. W. H. Dorne, J. Westerweel and F. T. M. Nieuwstadt, *Physical Review Letters*, 95(21):4, 2005.] Copyright 2005 by the American Physical Society.

In general, turbulence in pipe flow experiments is investigated in the way that the laminar flow state is artificially disturbed, and the focus is then on the transition to turbulence with its dynamical processes. The work of Peixinho and Mullin [79] is designed the other way around, which means that they constitute turbulent flow and monitor the process back to laminar flow by reducing the Reynolds number. This is a novel way to analyze coherent structures and approach recent theoretical developments. Therefore within Poiseuille flow an "equilibrium puff" is generated, considered as attractor for the system, and its decay back to laminar flow is observed. As mentioned before the control parameter in this case is the Reynolds number, which is reduced in a well-controlled manner using a piston to suddenly change the pipe diameter resulting in a decreased Reynolds number. Figure 2.7 shows the schematic experimental setup with which the

above described process is investigated. A schematic view of the flow control procedure



Figure 2.7: Schematic setup of the pipe flow facility for reverse transition investigations. Reprinted with permission from [J. Peixinho and T. Mullin, *Physical Review Letters*, 96(9):094501, 2006.

is depicted in Figure 2.8. On the left side of the pipe test section the developed Poiseuille flow at $Re = 1900$ is schematically depicted through the shown velocity profile. Further downstream the injected perturbation takes place marked by the arrow. The puff is generated and progresses downstream. Finally, the Reynolds number is reduced to a prescribed value Re_{final} and the resulting process is detected.

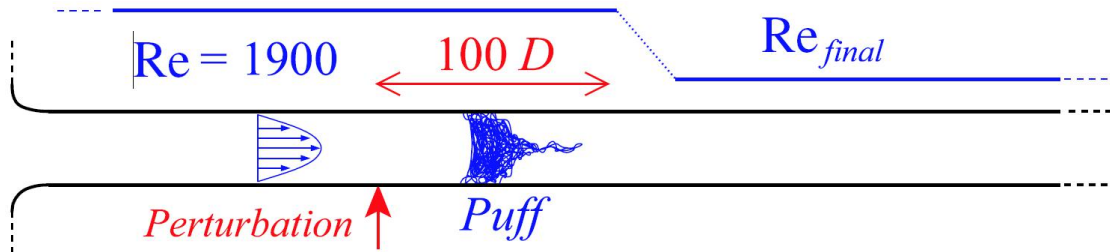
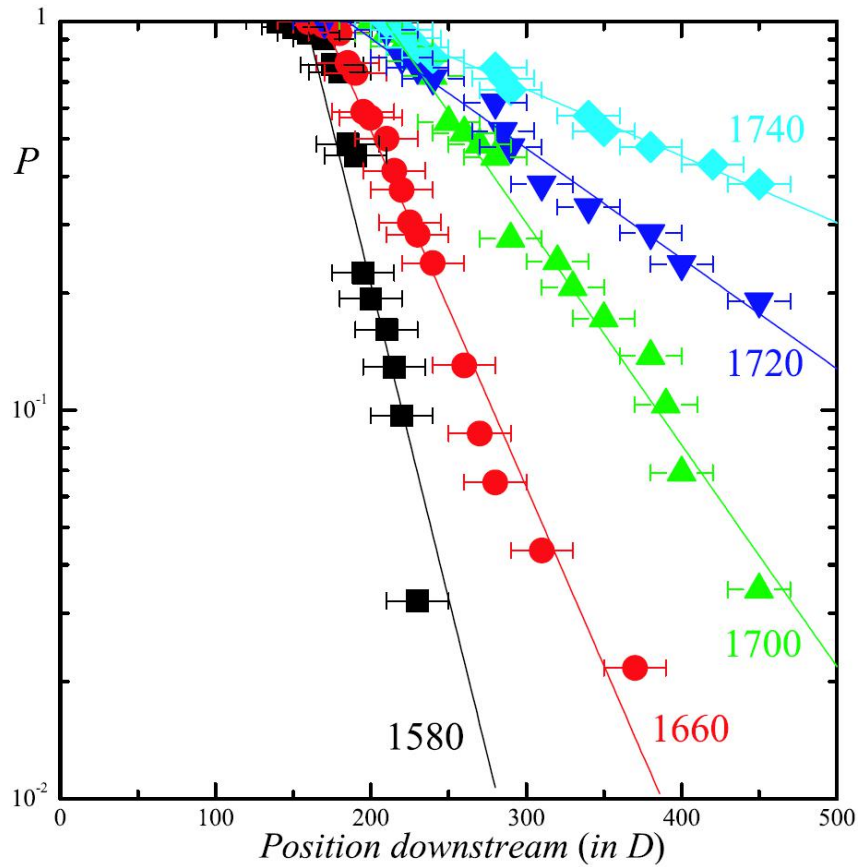


Figure 2.8: Schematic view of flow control procedure. Reprinted with permission from [J. Peixinho and T. Mullin, *Physical Review Letters*, 96(9):094501, 2006.

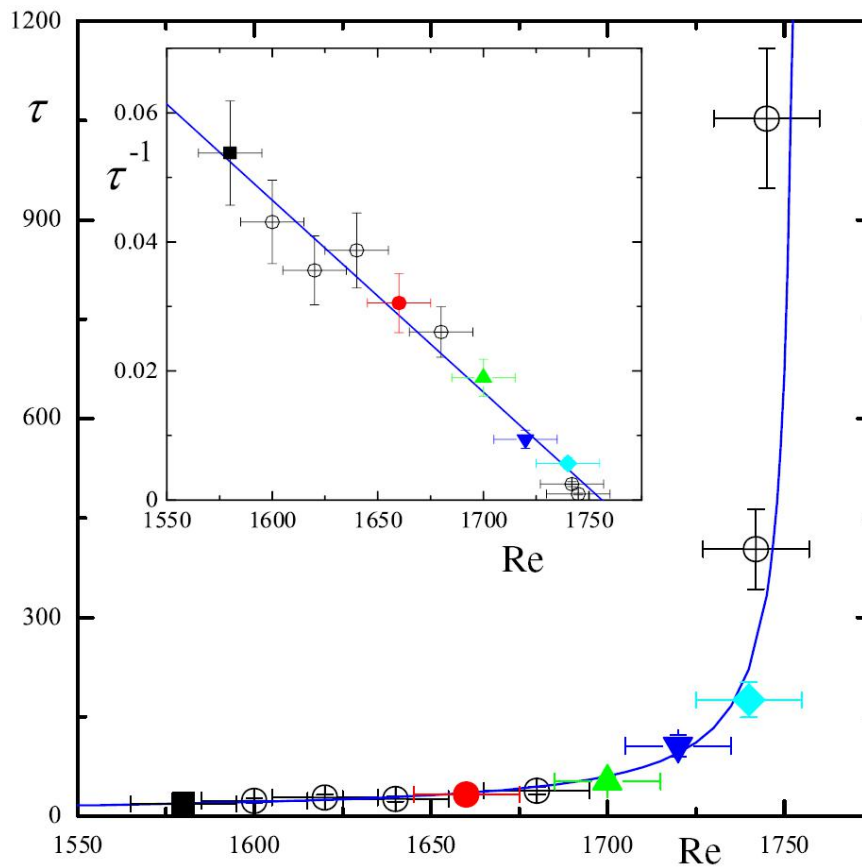
Peixinho and Mullin [79] observe a shrinking of the induced puffs to approximately half their original size. The distance for this process is probabilistic in nature and thus the most useful representation and measure is the probability P of observing a localized disturbed region within the flow as a function of the streamwise distance in pipe flow diameter D , depicted in Figure 2.9(a). Another interpretation of the data sets is presented in Figure 2.9(b), where τ is the decay rate. It is shown that τ diverges at a value of $Re_c = 1750 \pm 10$ indicating an approach to infinity of the lifetime of a localized turbulent structure at a critical Reynolds number. Below this critical threshold turbulence decays in streamwise distance.

In conclusion, the novel experiments of Peixinho and Mullin [79] indicate that the laminarization process progresses through structured stages [79]. And that close to the threshold, where the half-life becomes infinite, modulated wave packages emerge, which are significant features of this dynamical process.

Working on turbulence and chaos control requires further detailed information on the decay of turbulence at a certain point in time. It denotes for an experimental performance that the probability of decaying turbulence has to be captured in a statistically sufficient



(a) Probability of observing a puff with respect to streamwise distance.



(b) Variation of the decay rate as a function of the Reynolds number.

Figure 2.9: Results regarding reverse transition. Reprinted with permission from [J. Peixinho and T. Mullin, *Physical Review Letters*, 96(9):094501, 2006.

number of experiments. These investigations are conducted and reported by Hof et al. [39], who designed therefor a new test setup depicted in Figure 2.10. The probability

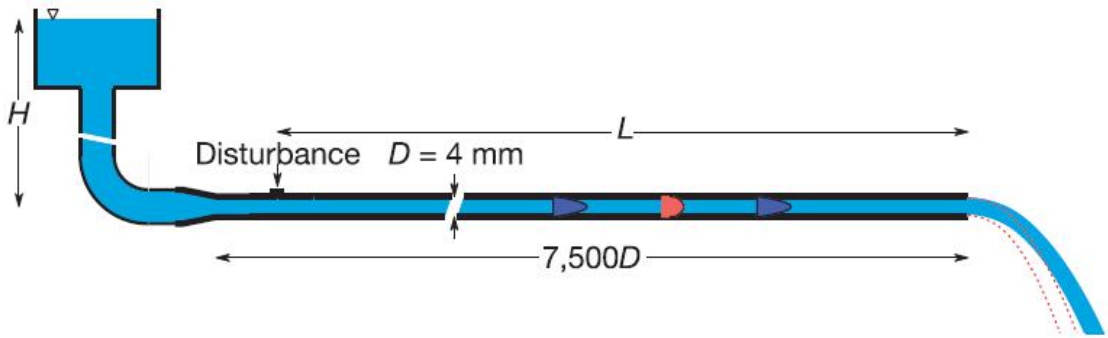


Figure 2.10: Schematic setup of the pipe test facility. Reprinted by permission from Macmillan Publishers Ltd: [Nature] (Hof et al. [39]), copyright (2006).

observed in this way can be expressed in terms of the probability distribution function:

$$P(t, Re) = \exp[-(t - t_0)/\tau(Re)], \quad (2.1)$$

where t is the observation time, t_0 is a constant delay ($t_0 \ll \tau$), and τ is the characteristic lifetime depending on Re . The observed results, which are shown in Figure 2.11, do not support the expectations from previous studies [29, 79]. Here, the shown results for different observation times collapse onto a single *S-shape* curve converging to $P = 1$ for higher Reynolds numbers. Hence, these results indicate that turbulence in pipe flow decays, and that finally after a certain time the flow always relaminarizes. This establishes immense possibilities for turbulence control mechanism. Maybe, this is a universal property of this class of flows, which turns it additionally to a very special field of interest for scientists and engineers.

The above described contradictory results [29, 39, 79, 105] are believed to be caused by different experimental and numerical protocols applied to trigger turbulence. For clarification de Lozar and Hof [20] conduct intensive experiments with the focus on four different perturbation schemes and two different pipe lengths. The resultant decay rates τ^{-1} for the different triggering procedures are presented by them [20] as a function of the Reynolds number. A detailed description of the triggering procedures and the results can be found elsewhere [20]. In conclusion, the obtained results show no clear dependence or influence due to the applied triggering system. Therewith, all four investigated perturbation systems show the same decay statistics.

The possibility to relaminarize pipe flow by applying a certain control mechanism to the system pushed scientists to do further research on this topics. Very important results are reported by Hof et al. [41], who

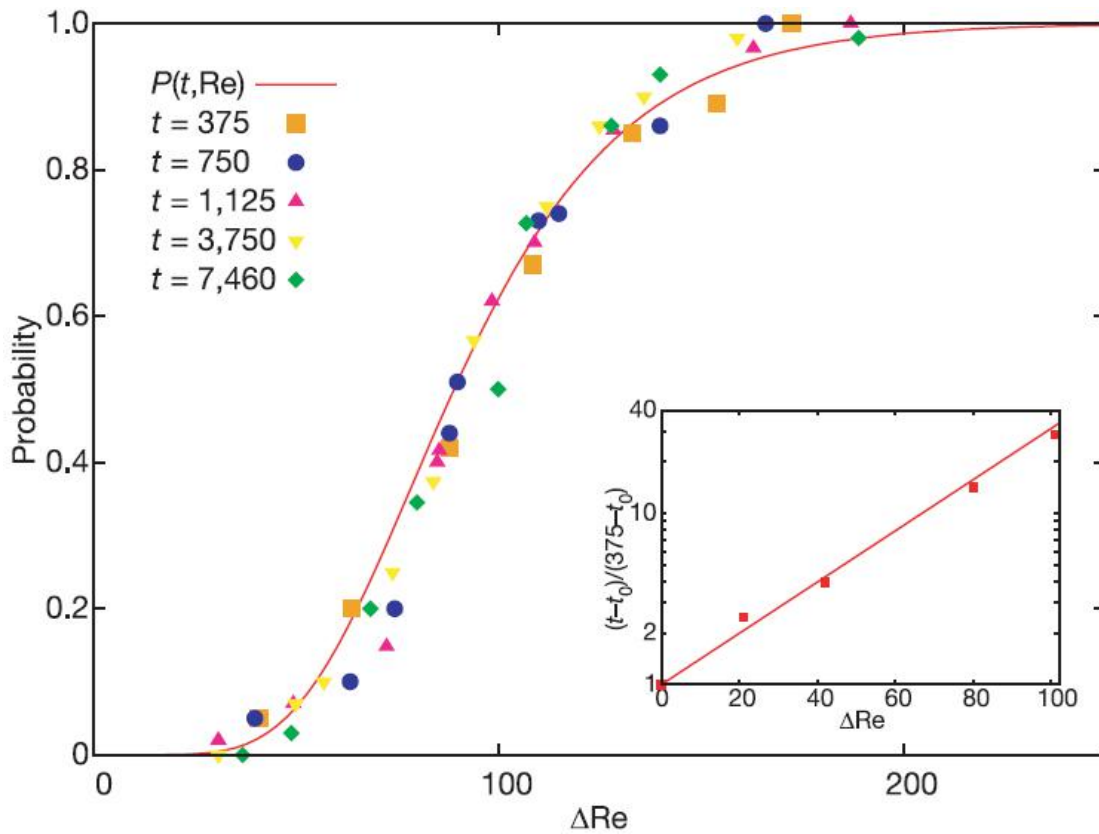


Figure 2.11: Probability distribution of lifetimes with respect to Reynolds number. Reprinted by permission from Macmillan Publishers Ltd: [Nature] (Hof et al. [39]), copyright (2006).

uncovered an amplification mechanism that constantly feeds energy from the mean shear into turbulent eddies. [41]

This finding is the basis for investigations on the interception of this energy transfer, and the application of a sufficient control mechanism to force the relaminarization process. The mechanism itself consists of continuous injection and simultaneous withdrawal of water through small holes in the wall of the pipe. The experimental procedure showing the relaminarization process is structured in three phases. At first, an intermittent flow ($Re = 2000$) is created by adding a small perturbation to the pipe inlet, which periodically generates turbulent puffs. Figure 2.12 A depicts the laminar and turbulent regions, which can be clearly distinguished. Thereafter, the permanently generated puffs get time to travel downstream. This is shown in Figure 2.12 B. The last step during this manipulation is the triggering of the control mechanism, which is kept on for the rest of the experimental observation. The result is depicted in Figure 2.12 C, where it is obvious that the turbulent puffs decay and a laminar zone emerges. Even the required pressure difference to pump the fluid is reduced to the laminar value, refer to Figure 2.12 D.

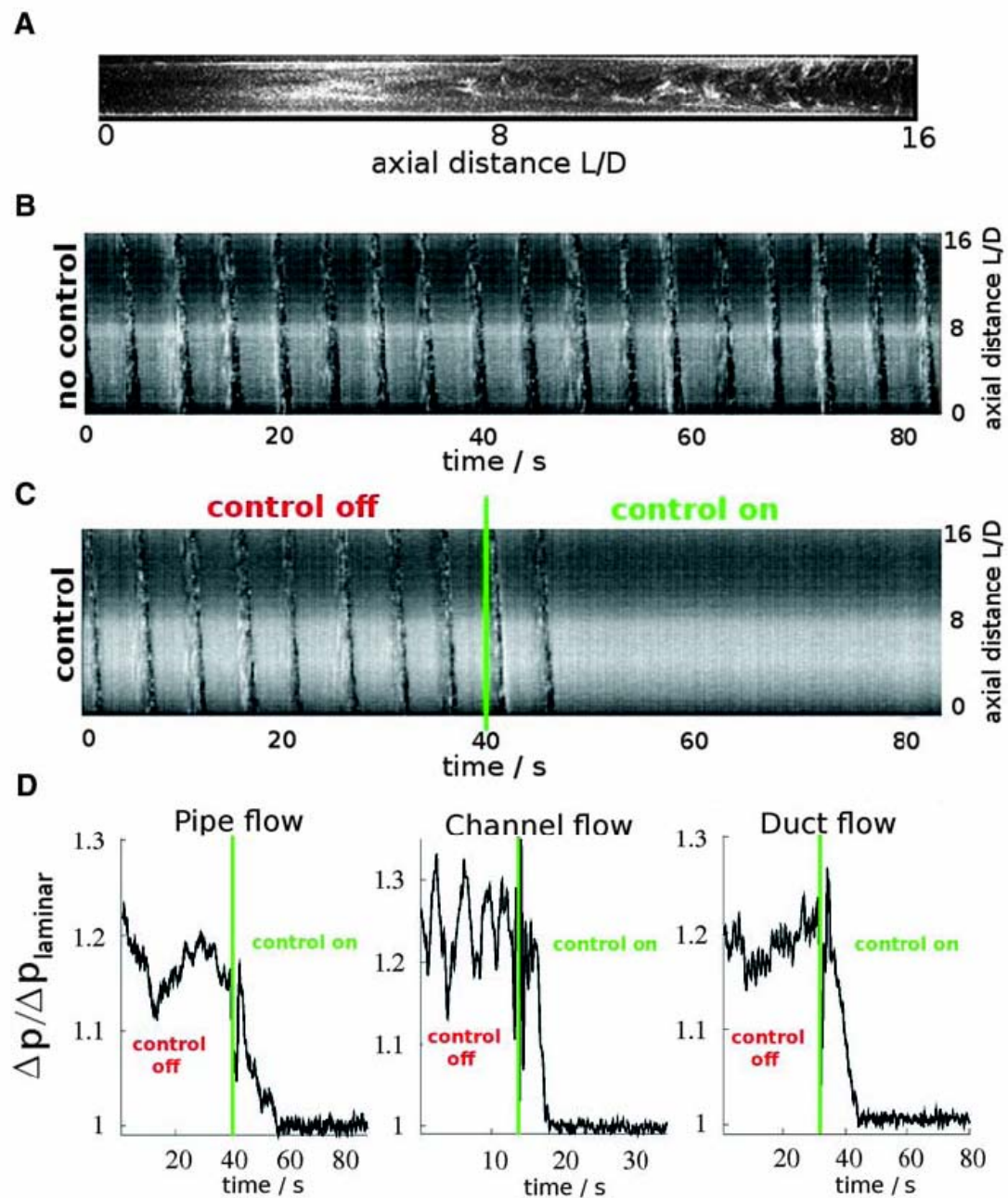


Figure 2.12: Realization of the control mechanism within the experiment. From [B. Hof, A. de Lozar, M. Avila, X. Tu and T. M. Schneider. Eliminating Turbulence in Spatially Intermittent Flows. *Science*. 327:4, 2010.]. Reprinted with permission from AAAS.

Similar results can be obtained by applying the above mechanism to an intermittent channel and square duct flow (Figure 2.12 D). In conclusion, Hof et al. [41] state that this simple control mechanism works very well for sufficiently low Reynolds numbers, but it becomes less efficient with increasing Reynolds number, and fails once the regime of spatially expanding turbulence is reached ($Re \geq 2500$). For more clarity Table 2.1 lists the resulting limitations.

Table 2.1: Overview of different shear flows and the limiting Reynolds numbers [41].

flow system	pipe	channel	duct
Reynolds number	< 2000	< 1400	< 1800

All of the described scientific work in the field of low Reynolds number pipe flow is important and necessary to uncover the distinct critical point at which pipe flow becomes persistently turbulent. During many years of pipe flow research on this topic different critical Reynolds numbers are estimated due to different criteria used for definition [26], which are presented in Table 2.2. It is obvious that the scattering values are

Table 2.2: Overview of critical points for the sustainment of pipe flow turbulence.

Reference	Critical Point
Reynolds [85]	2020
Darbyshire and Mullin [19]	1700
Faisst and Eckhardt [29]	≥ 1800
Eckhardt [26]	≈ 1950
Eckhardt [25]	3000

insufficient. Hence, Avila et al. [4] conducted time-consuming experiments as well as numerical simulations using two independent numerical codes, which are described briefly in Chapter 2.4, to estimate the onset of sustained turbulence. Mainly, the experimental procedure comprises the generation of a single turbulent puff and the monitoring of any changes in the development of the flow. This procedure was developed by Hof et al. [36] and improved through Hof et al. [39] and de Lozar and Hof [20], and is therefore a well-known and proven technique. The post-processing of the data is the analysis of the mean lifetime of an initial puff before decaying or splitting. All the sampled data as well as the results of the numerical simulations are depicted in Figure 2.13. The presented intersection point of the left (decaying turbulence) and the right (puff splitting) branch

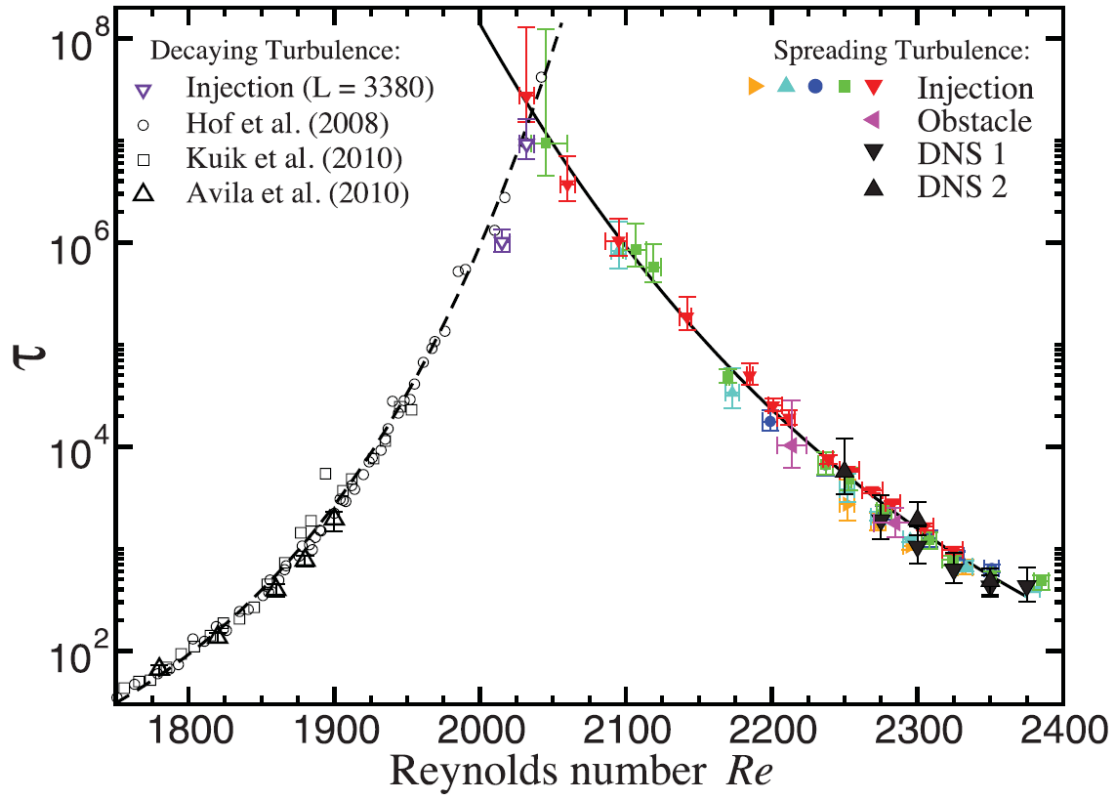


Figure 2.13: Mean lifetime of a puff before decaying or splitting. From [K. Avila , D. Moxey, A. de Lozar, M. Avila, D. Barkley and B. Hof. The onset of turbulence in pipe flow. *Science*, 333(192):192-196, 2011]. Reprinted with permission from AAAS.

marks the critical point for the onset of sustained turbulence and is approximately 2040 ± 10 .

2.2 Moderate Reynolds Number Range

The previous chapter describes in detail the onset of sustained turbulence and the occurring fluid flow pattern, e.g. puffs and slugs. Hence, the smallest Reynolds number range, which can be investigated ($Re \leq 5 \times 10^3$). The present chapter deals with the next order of magnitude: $5 \times 10^3 < Re \leq 10 \times 10^4$.

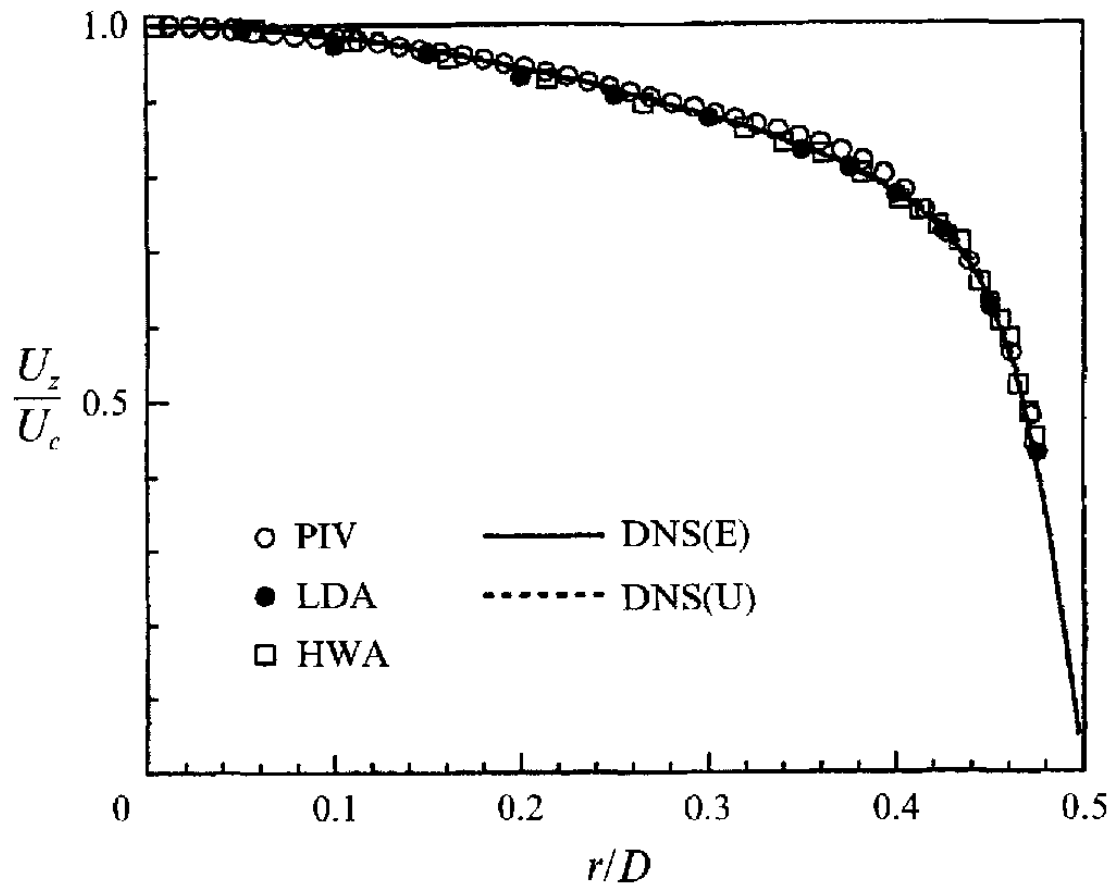


Figure 2.14: Normalized mean velocity scaled by the centerline velocity U_c as a function of the dimensionless pipe diameter (r/D). From J.G.M. Eggels, F. Unger, M.H. Weiss, J. Westerweel, R.J. Adrian, R. Friedrich and F.T.M. Nieuwstadt. Fully developed turbulent pipe flow: a comparison between direct and numerical simulation and experiment. *Journal of Fluid Mechanics*, 268:35, p. 185, reproduced with permission.

During the 1990ies the impact on numerical investigations was immense. With it, adequate tools for reproducing fluid dynamics are developed and hence comparative works, which means the comparison between experimental and numerical results, arise. One famous comparison is published by Eggels et al. [27]. Within this work the focus is on the study of fully developed turbulence for $Re_c = 7 \times 10^3$. The working tools for this

investigation are on one hand DNS and on the other intensive experiments within a test facility with circular cross section. Next to the comparison of DNS and experiments for pipe flow, they investigate additionally the similarities and differences of channel and pipe flow. One main result for the case of pipe flow is the excellent agreement of the lower-order statistics, which are mean velocity and variance. To confirm this result the normalized mean velocity scaled by the centerline velocity U_c as a function of the dimensionless pipe diameter (r/D) is depicted in Figure 2.14. Here, different measuring techniques and DNS results are compared and show clearly, that they collapse onto one single curve. In addition, the rms-values of the fluctuating velocity in all three dimensions (u_z , u_r , u_θ - cylindrical co-ordinates) even as a function of the normalized pipe diameter (r/D) are shown in Figure 2.15. And even for this second-order moment the concurrence between LDA, HWA, PIV and DNS is obvious.

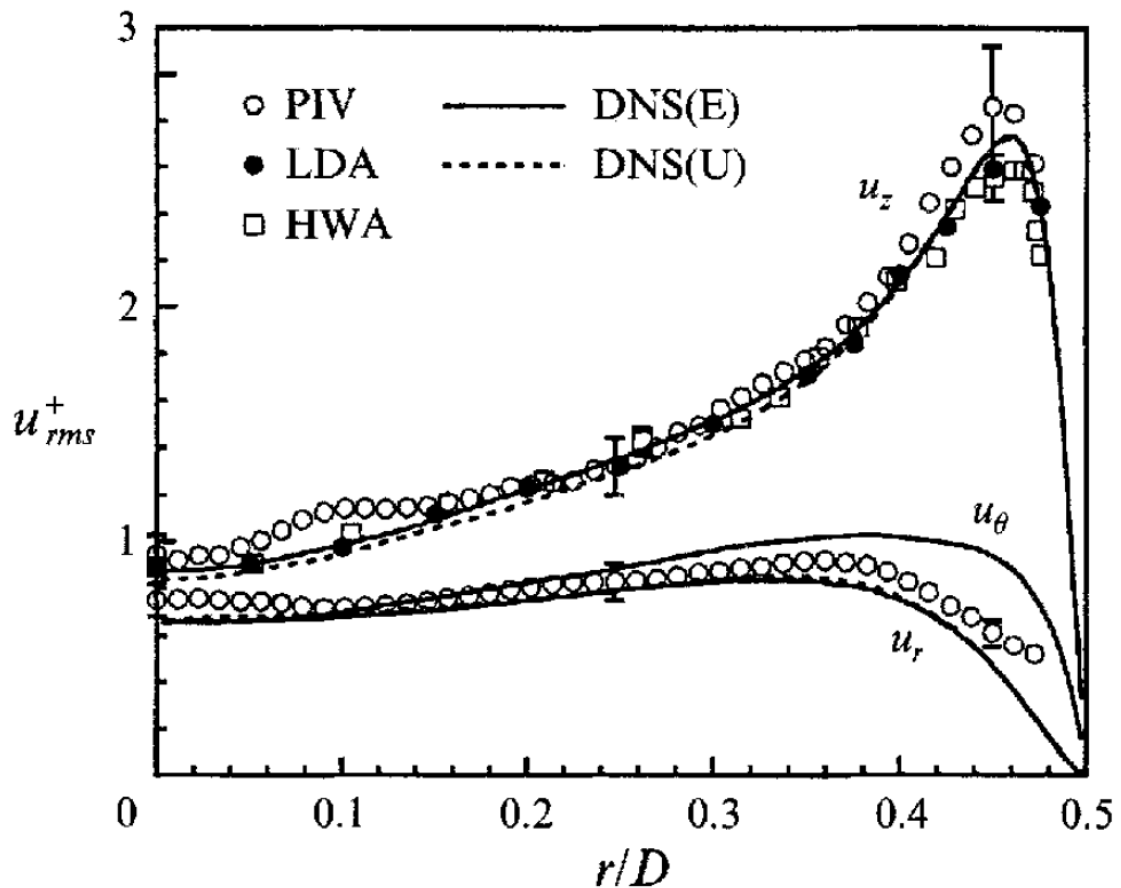


Figure 2.15: Variance of the fluctuating velocity as a function of the dimensionless pipe diameter (r/D). From J.G.M. Eggels, F. Unger, M.H. Weiss, J. Westerweel, R.J. Adrian, R. Friedrich and F.T.M. Nieuwstadt. Fully developed turbulent pipe flow: a comparison between direct and numerical simulation and experiment. *Journal of Fluid Mechanics*, 268:35, p. 195, reproduced with permission.

The second main result is the appropriate agreement for the higher-order statistics, i.e. skewness and flatness factors. Even therefor Eggels et al. [27] compare the above named measuring techniques and DNS results from different sources, e.g. Mansour et al. [60]. Figure 2.16 shows the third and fourth-order moment as a function of the wall distance scaled on inner co-ordinates for fully developed turbulence. From these figure the slight deviations between the curves are detected.

Eggels et al. [27] also focus on similarities and differences between two systems, namely pipe and plane channel flow. And their results show that the mean velocity profile of the pipe fails to conform the law of the wall in contrast to channel flow. Figure 2.17 depicts this deviation.

Even such results spark the discussion on the comparability of these two basic wall-bounded flow systems, pipe and channel flow, and on the validity of the law of the wall with the *von Kármán's* constant κ and the additive constant C .

The influence of the Reynolds number on turbulence statistics in pipe flow for a Reynolds number range of $5 \times 10^3 - 25 \times 10^3$ is investigated by den Toonder and Nieuwstadt [21] in a circular test facility with water as the working medium. The experimental setup, which is a closed-loop, and the special test section are depicted in Figure 2.18.

The focus within these investigations is on turbulence. Hence, den Toonder and Nieuwstadt [21] installed a tripping device formed as a ring to force early transition from laminar to turbulent pipe flow. To resolve the turbulent velocity field a LDV measurement system is applied to the setup. Therewith they are able to analyze the higher order statistics and the energy spectra. But the wall curvature produces refraction of the LDV laser beams due to the mismatch of the refractive index of the working medium and the pipe material. Hence, a special developed test section (refer to the left part in Figure 2.18) is installed to minimize this effect. To confirm the well working setup den Toonder and Nieuwstadt [21] compare their results to the DNS results of Eggels et al. [27] (refer to Figure 2.19a). It is clear from this figure that there is an excellent agreement between the observed experimental and numerical results. But the representation of the mean velocity profile scaled in inner variables shows the aforementioned Reynolds number dependence within the logarithmic layer and therewith a deviation of the constants valid from the "universal" law of the wall (refer to Figure 2.19b). Such a significant Reynolds number dependence can not be observed for the velocity fluctuations and even not for the higher-order statistics, like skewness and flatness factor. The spectral measurements performed at $y^+ = 12$ and $y^+ = 30$ for three different Reynolds numbers show also no clear significant dependence on the Reynolds number. Only a slight increase of energy can be observed for increasing Reynolds numbers. In conclusion den Toonder and Nieuwstadt [21] argue for a proof of a clear Reynolds number dependence of turbulence

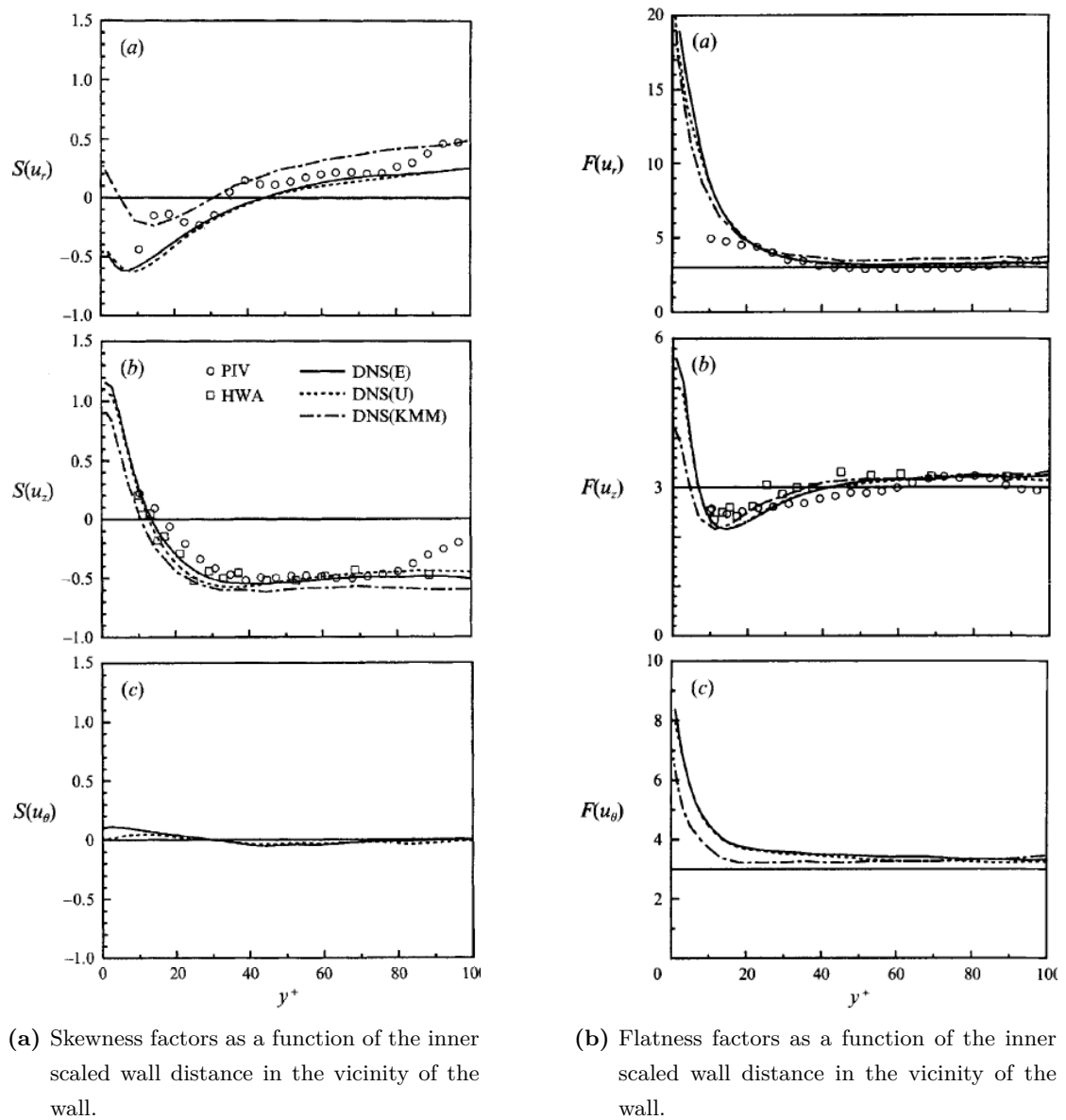


Figure 2.16: Higher-order statistical moments in the case of fully developed turbulence from experiments as well as DNS results: (a) normal-to-the-wall velocity component, (b) streamwise velocity component and (c) the circumferential velocity component. From J.G.M. Eggels, F. Unger, M.H. Weiss, J. Westerweel, R.J. Adrian, R. Friedrich and F.T.M. Nieuwstadt. Fully developed turbulent pipe flow: a comparison between direct and numerical simulation and experiment. *Journal of Fluid Mechanics*, 268:35, p. 199-200, reproduced with permission.

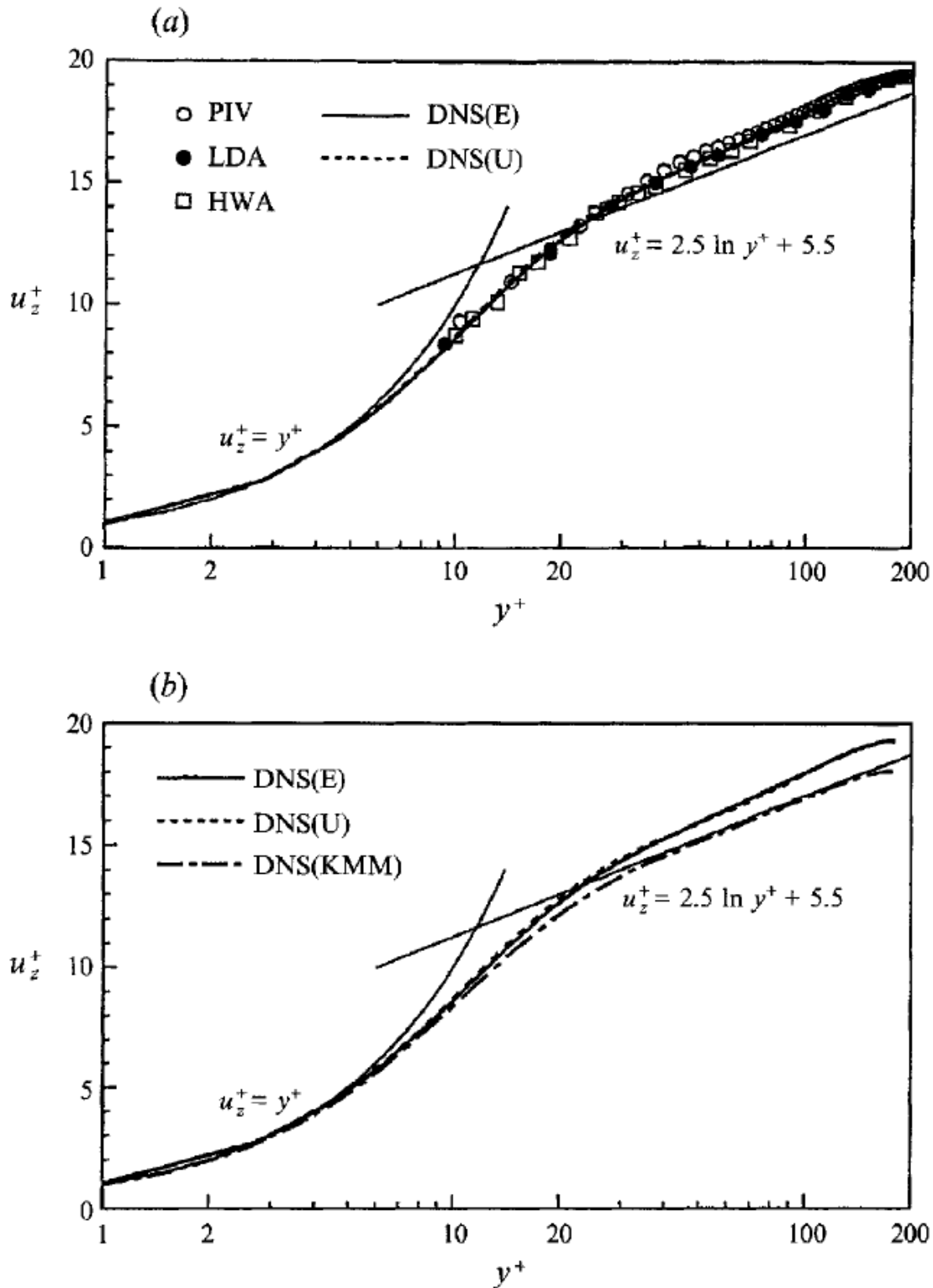


Figure 2.17: Axial mean velocity profile as a function of y^+ : (a) experimental and numerical results and (b) comparison of DNS data by [60] for channel flow and DNS data by [27] for pipe flow. From J.G.M. Eggels, F. Unger, M.H. Weiss, J. Westerweel, R.J. Adrian, R. Friedrich and F.T.M. Nieuwstadt. Fully developed turbulent pipe flow: a comparison between direct and numerical simulation and experiment. *Journal of Fluid Mechanics*, 268:35, p. 187, reproduced with permission.

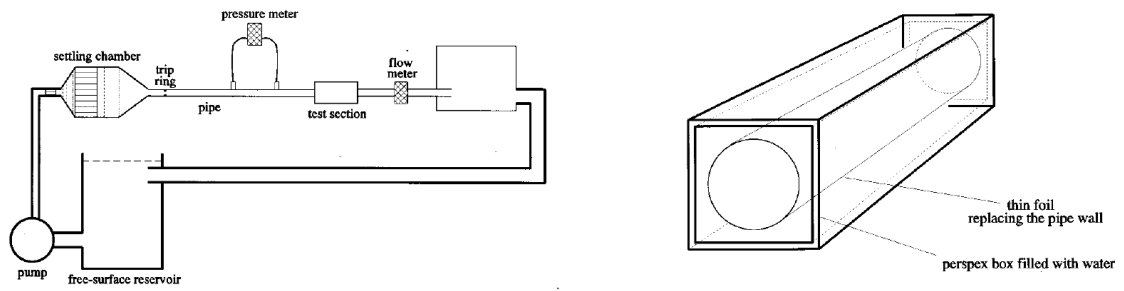
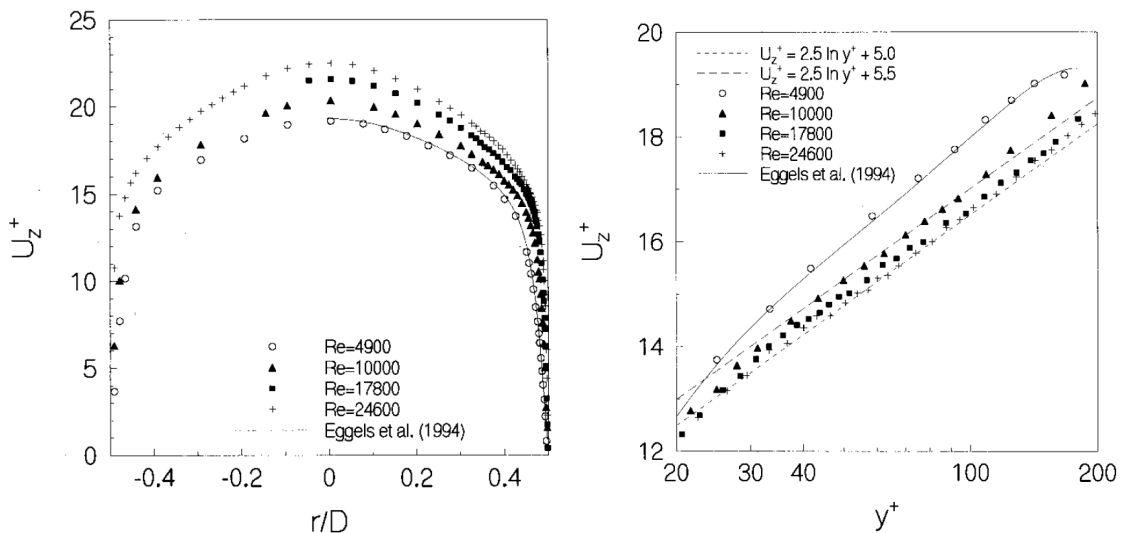


Figure 2.18: Left: Experimental setup of the pipe test facility. Right: Special test section. Reprinted with permission from [J.M.J. den Toonder and F.T.M. Nieuwstadt. Reynolds number effects in a turbulent pipe flow for low to moderate Re. *Physics of Fluids*, 9(11), 1997.]. Copyright [1997], AIP Publishing LLC.



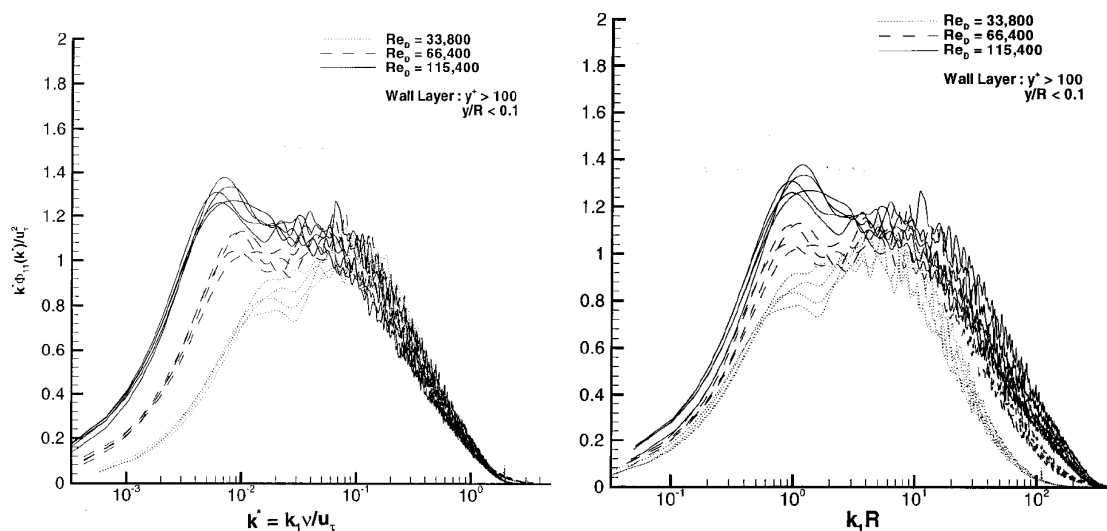
(a) Mean velocity profiles for four different Reynolds numbers and the comparison with DNS results.

(b) Detailed view of the logarithmic layer.

Figure 2.19: Overview about mean velocity profiles for four different Reynolds numbers. Reprinted with permission from [J.M.J. den Toonder and F.T.M. Nieuwstadt. Reynolds number effects in a turbulent pipe flow for low to moderate Re. *Physics of Fluids*, 9(11), 1997.]. Copyright [1997], AIP Publishing LLC.

statistics scaled on inner variables for low to moderate Reynolds number in a pipe flow system [21]. And that the observed asymptotic behavior indeed appears valid for higher Reynolds numbers should be the focus of future investigations on this topic for larger Reynolds numbers.

Beside the investigations on mean and fluctuating velocities as well as the turbulence statistics higher-order the structural behavior of turbulent pipe flow become important. Due to this fact Kim and Adrian [53] perform hot-film investigations in a pipe with air as the working medium for three Reynolds numbers $Re_c = 33.8 \times 10^3, 66.4 \times 10^3, 115.4 \times 10^3$ with the focus on the spectra and the wave numbers occurring from the fluid system. The resulting premultiplied spectra for two different scales is presented in Figure 2.20.



(a) Premultiplied spectra scaled on inner variables. (b) Premultiplied spectra scaled on outer variables.

Figure 2.20: Representation of the premultiplied spectra for two different scaling showing the correlation behavior for low and high wave number modes. Reprinted with permission from [K. C. Kim and R. J. Adrian. Very large-scale motion in the outer layer. *Physics of Fluids*, 11, 1999.]. Copyright [1999], AIP Publishing LLC.

The authors show that the two modes, low and high wave number modes, hold a different correlation behavior. On one side the high wave number parts of the investigated Reynolds numbers correlate with the premultiplied spectra scaled on inner variables, refer to Figure 2.20a. Whereas on the other side the lower wave number parts investigated correlate with the premultiplied spectra scaled on outer variables, refer to Figure 2.20b. This knowledge is useful with regard to the interpretation of the occurring low wave number maxima. Figure 2.21 gives a deeper insight in the variation of this low wave number maxima with radial location and Reynolds number, respectively.

Within Figure 2.21 the arrows indicate the scale of the large-scale motions, Λ_{max} , due

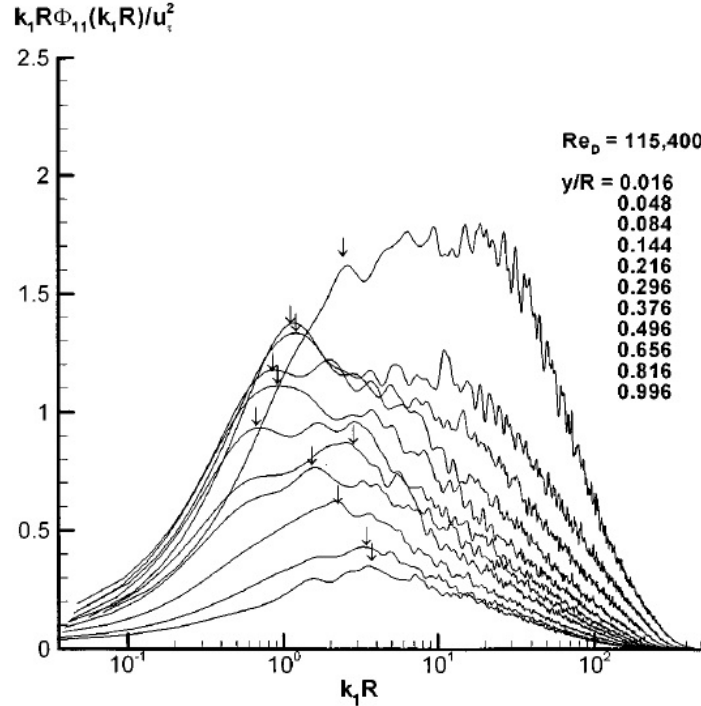


Figure 2.21: Premultiplied spectra for $Re_c = 115.4 \times 10^3$ as a function of the distance from the wall. Each small arrow indicates the wave number of the very large-scale motion, $2\Pi/\Lambda_{max}$. Reprinted with permission from [K. C. Kim and R. J. Adrian. Very large-scale motion in the outer layer. *Physics of Fluids*, 11, 1999.]. Copyright [1999], AIP Publishing LLC.

to the location of the maximum $2\Pi/\Lambda_{max}$. To clearly estimate the length of the large-scale motions within the system Kim and Adrian [53] rearranged the dimensionless wave length as a function of the wall distance (refer to Figure 2.22). What we can see from this figure is the large extent of the very large-scale motion in the streamwise direction. The estimated maximum value for Λ_{max} is at about 14 pipe radii, which is much more higher than previously reported. Additionally, this rearrangement shows the occurrence of the very large-scale motions over the entire logarithmic region of the mean velocity profile ($\leq 0.4 R$). In conclusion Kim and Adrian [53] discover the large extent of the VLSM as well as their formation within the flow system. The beginning is coherently aligned hairpin packets, which form the LSM. These packets also align coherently to form the very large-scale motions.

At the lower bound of the moderate Reynolds number range the occurring structures called puffs and slugs are of great importance due to the understanding of the transition process from laminar to turbulent flow. Since the formation process from a slug-like structure to turbulence is generally known (refer to [107]) Nishi et al. [76] perform investigations on the naturally occurring slug formation. This process is called "puff splitting",

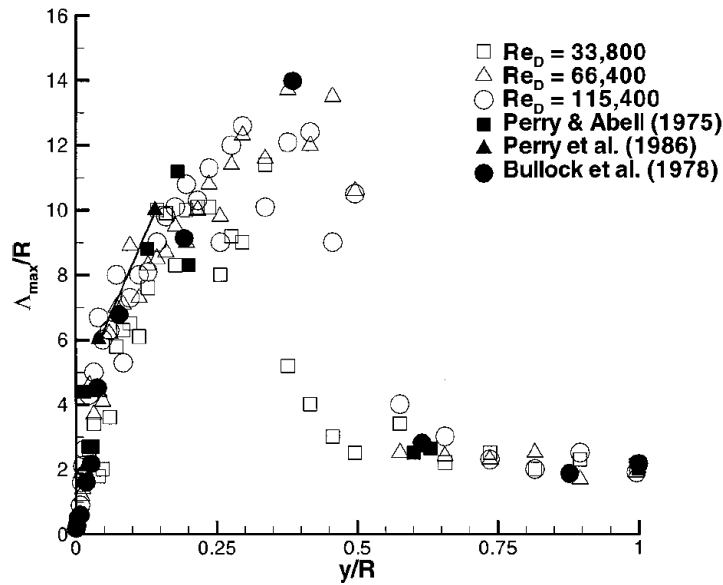


Figure 2.22: The dimensionless wavelength of the very large-scale motion. Reprinted with permission from [K. C. Kim and R. J. Adrian. Very large-scale motion in the outer layer. *Physics of Fluids*, 11, 1999.]. Copyright [1999], AIP Publishing LLC.

where the split puffs develop into a slug. For realization a special test facility is designed, which is shown in Figure 2.23.

Although the behavior of a slug is clear in general the conducted experiments of Nishi et al. [76] are divided into two parts:

1. Studies of slug development, and
2. Studies of puff development.

The main result of the first set of measurements is the expanding of the slugs along the pipe. This phenomena is found to correlate with the different propagation velocities of the front and back edges of the slugs. Figure 2.24 depicts the described behavior, where the arrows indicate the front and back of the slug.

The second measurement campaign gives an insight into the behavior of puffs for changing Reynolds numbers. This means, that for low Reynolds numbers the perturbation at the inlet of the pipe is able to form a puff, and that remains unaffected along the facility. For increasing Reynolds numbers these puffs split once ore more, and for sufficiently high Reynolds numbers the produced puffs merge into slugs and even behave slug-like for the rest of the pipe. The development of the process is depicted in Figure2.25. Interestingly, the through "puff splitting" developed slugs also initiate the laminar-to-turbulent transition process as well as the original slugs. In spite of these results there are a lot of open

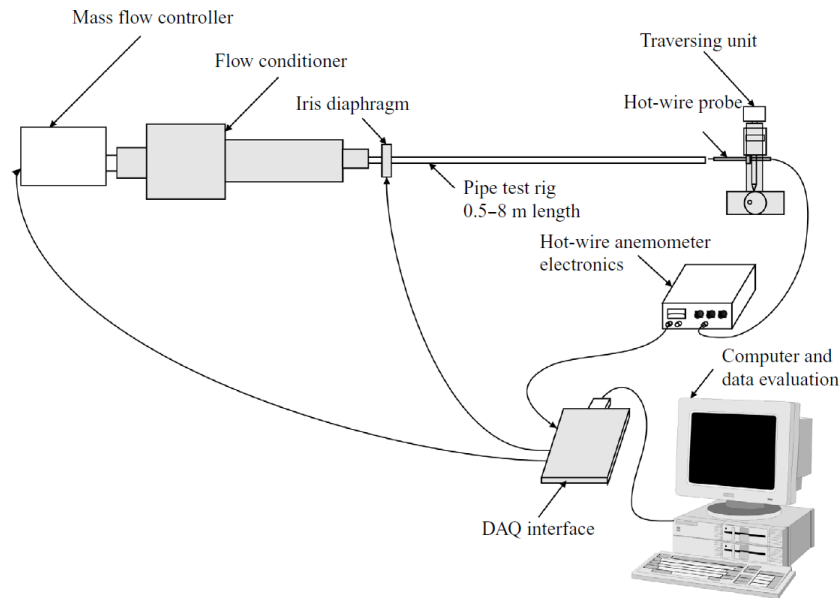


Figure 2.23: Schematic of special experimental test facility for "puff splitting" investigations. From Mi. Nishi, B. Ünsal, F. Durst, and G. Biswas, Laminar-to-turbulent transition of pipe flows through puffs and slugs, *Journal of Fluid Mechanics*, 614(-1), p. 428, reproduced with permission].

questions on this topic, for example the influence of the traveling wave solution/theory or transitional flows [76]. This will be supported even by numerical investigations.

¹Note that the lower bound of the moderate Reynolds number range is $\approx 5 \times 10^3$, but the phenomena for the shown results ($Re = 2.68 \times 10^3$, $Re = 2.68 \times 10^3$) are the same as for the slightly higher Reynolds number and hence the example is a suitable showcase.

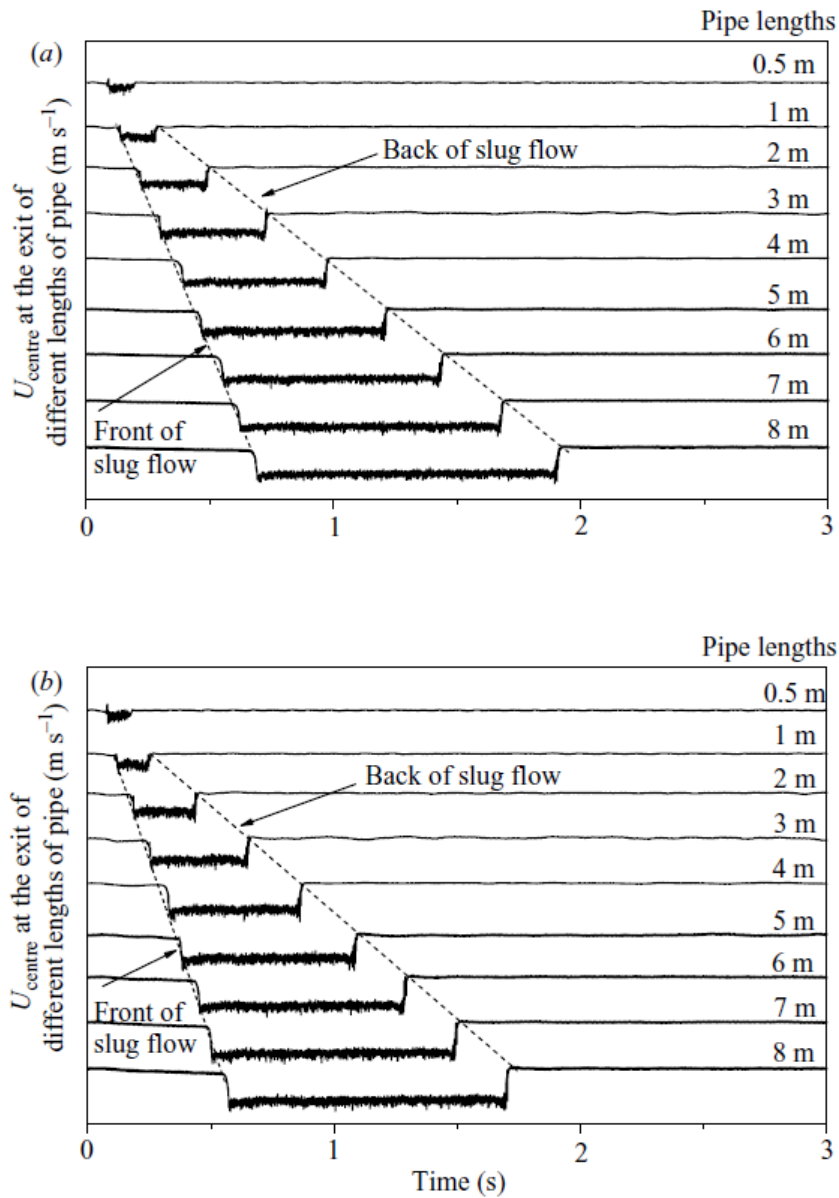


Figure 2.24: Development of slug for two different Reynolds numbers (a) $Re = 8.23 \times 10^3$ and (b) $Re = 10.07 \times 10^3$. From Mi. Nishi, B. Ünsal, F. Durst, and G. Biswas, Laminar-to-turbulent transition of pipe flows through puffs and slugs, *Journal of Fluid Mechanics*, 614(-1), p. 435, reproduced with permission].

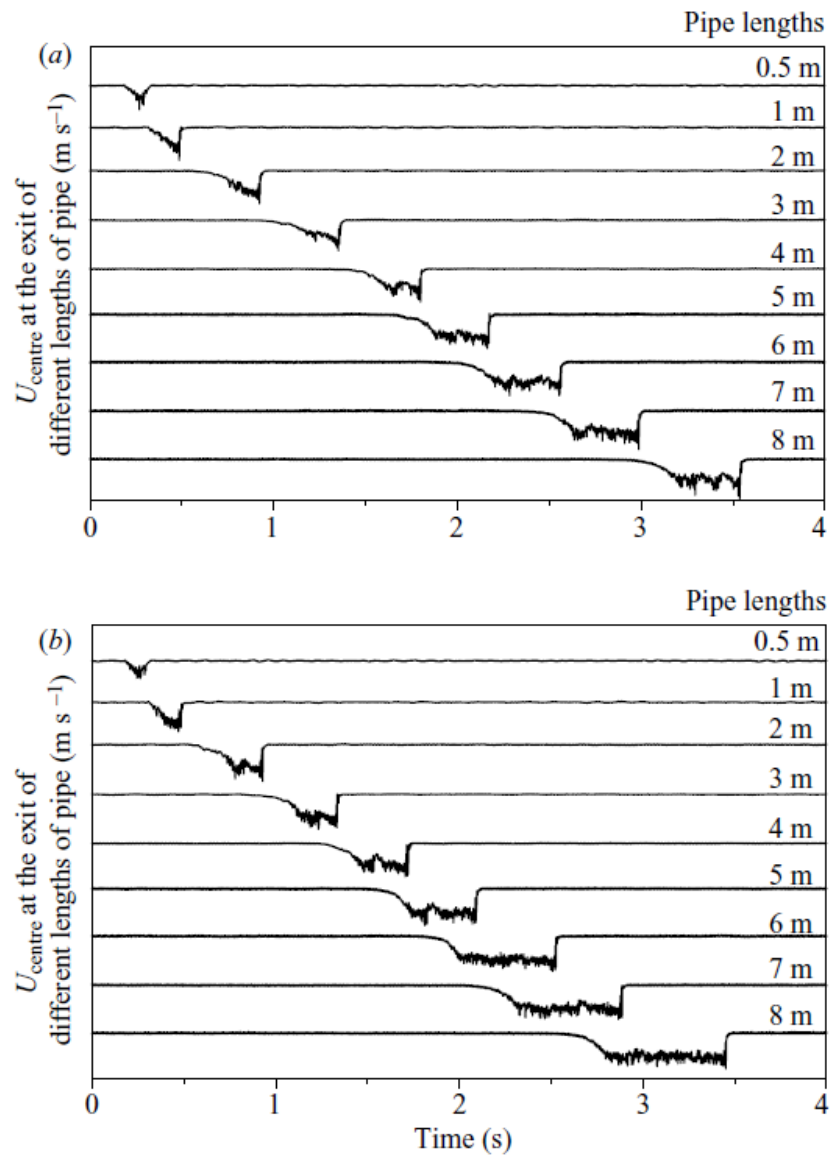


Figure 2.25: Development of a puff for two different Reynolds numbers (a) $\text{Re} = 2.68 \times 10^3$ and (b) $\text{Re} = 2.865 \times 10^3$ showing "puff splitting"¹. From Mi. Nishi, B. Ünsal, F. Durst, and G. Biswas, Laminar-to-turbulent transition of pipe flows through puffs and slugs, *Journal of Fluid Mechanics*, 614(-1), p. 438, reproduced with permission].

2.3 High and Very High Reynolds number Experiments - An Approach to Nature

Pipe flow turbulence is extended to a large range of Reynolds numbers. All of them have their own allurements, which scientist can meet if different requirements in laboratory experiments are fulfilled. The most applicable and at the same time highly feasible Reynolds number range is about $Re \geq 5 \times 10^5$. That is why pipe flow facilities covering this range of Reynolds numbers are rare. Hence, only two suitable wind tunnels with circular cross section are established, namely the *Princeton/DARPA-ONR SuperPipe Facility* and the *CoLaPipe*, presented within this work. Another impressive facility is actual in the phase of installation, namely CICLoPE, which will contribute the ongoing discussions in the near future.

The *SuperPipe* was set up in 1996 with the aim of investigating high and very high Reynolds number pipe flow (including an unprecedented Reynolds number range of $Re \approx 3.5 \times 10^7$). Zagarola [108] presented a detailed description of the facility with all components and first results. A schematic setup is depicted in Figure 2.26.

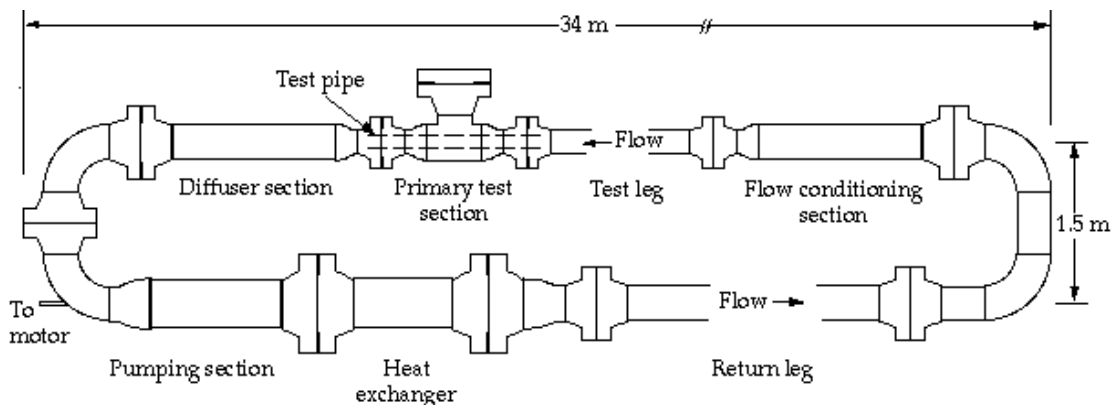


Figure 2.26: Schematic setup of the SuperPipe. From [108].

With the finish of the setup of the *SuperPipe* a new age on the field of experimental investigations on pipe flow begins. Intensive measurements on the mean velocity profile should shed light on several unclear aspects, like the Reynolds number independence of the law of the wall and its constants (κ , B) and the "true" scaling behavior exceeding the linear part of the boundary layer. Hence, a couple of publications presents new developed and revised laws regarding mean flow scaling [109–112]. The basis builds an intensive measurement series on the behavior of the mean velocity for different Reynolds numbers up to $Re = 35 \times 10^6$, which is exemplary shown in Figure 2.27. Presented is the inner scaled mean velocity profile as a function of the dimensionless wall distance.

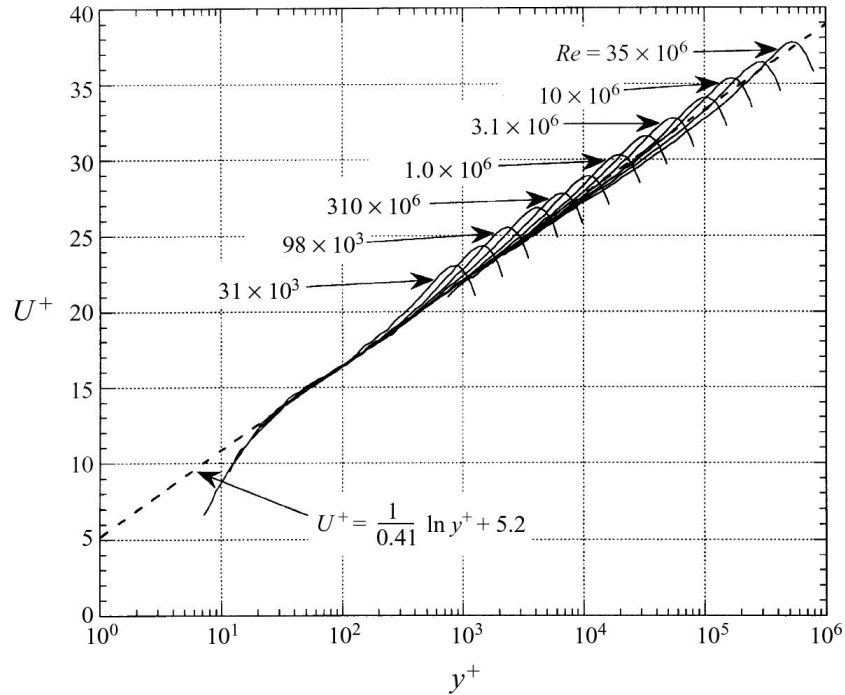


Figure 2.27: Linear-log plot of normalized velocity profiles using inner variables (u_τ). From M. V. Zagarola and A. J. Smits, Mean-flow scaling of turbulent pipe flow, *Journal of Fluid Mechanics*, 373, p. 61, reproduced with permission.

An assumption, which has to be stated prior to any investigations, is the fact of the smoothness of the pipe surface and therefore the dependence on only the Reynolds number [108]. Hence, for measurements within the *SuperPipe* the equations for smooth surfaces are valid. The following measurement series provided by [109–112] establish new and revised scaling laws for the mean velocity profile. The main point here is the scaling parameter for the non-dimensionalization, which is believed to be $U_{Cl} - \bar{U}$. The representation of the mean velocity profiles show a better agreement in comparison to the general way of using the inner variable u_τ , refer to Figure 2.28. Further research on this topic, meaning reinterpretations of the already presented results ([109–112]), e.g. by Barenblatt et al. [10] and Perry et al. [81] shows that the *Princeton/DARPA-ONR SuperPipe Facility* is not smooth for higher Reynolds numbers, here exceeding 10^6 , and hence the underlying formulas are not appropriate. This conclusion makes it difficult to appraise the presented results for such high Reynolds numbers. On the other hand newer publications of McKeon et al. [65] or [91] confirm the assumption of Zagarola [108] and the others, that their results even for the highest Reynolds number ($\approx 3 \times 10^7$) are unaffected by surface roughness and hence can be treated as hydraulically smooth.

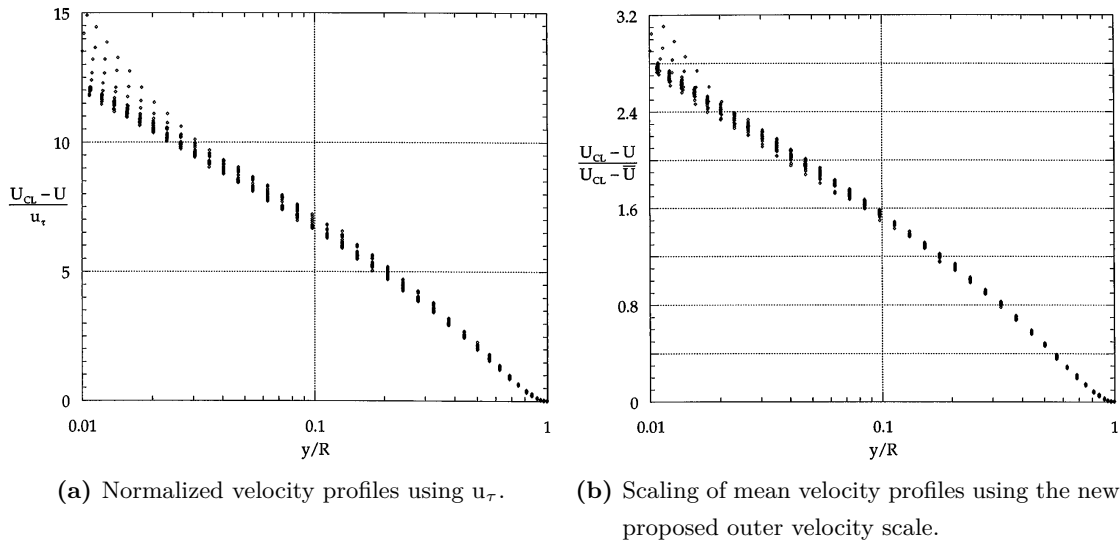


Figure 2.28: Representation of mean velocity profiles using two different scaling methods: a) conventional outer velocity scaling, and b) new proposed outer velocity scaling. Reprinted figures with permission from [M. V. Zagarola and A. J. Smits, *Physical Review Letters*, 78, p. 242, 1997.] Copyright (1997) by the American Physical Society.

On this basis McKeon et al. [67] propose their new friction factor relationship:

$$\frac{1}{\sqrt{\lambda}} = 1.930 \log(Re_D \sqrt{\lambda}) - 0.537,$$

valid for the Reynolds number range of $310 \times 10^3 \leq Re_D \leq 18 \times 10^6$. This is a result coming out of the comparison with *Prandtl's "universal" friction factor relationship*, which is a suitable characterization for a limited and lower range of Reynolds numbers. But seem to be unsuitable for the extrapolation regarding higher Reynolds numbers represented by the deviation of the friction factors for different high and very high Reynolds numbers, refer to Figure 2.29. Even interesting beside the mean velocity and the friction factors for high Reynolds numbers is the evolution of statistical quantities, which mean higher-order moments. As representative the second-order moment, the streamwise fluctuating velocity, is depicted in Figure 2.30. The shown data sets are measured within the *Superpipe* as well, and yield a second peak for u'^+ , beside the near wall peak due to production of kinetic energy, which is at this time believed to represent structural changes in the flow field [71]. These possible changes can be large and very large scale motions formed from hairpin vortex packets.

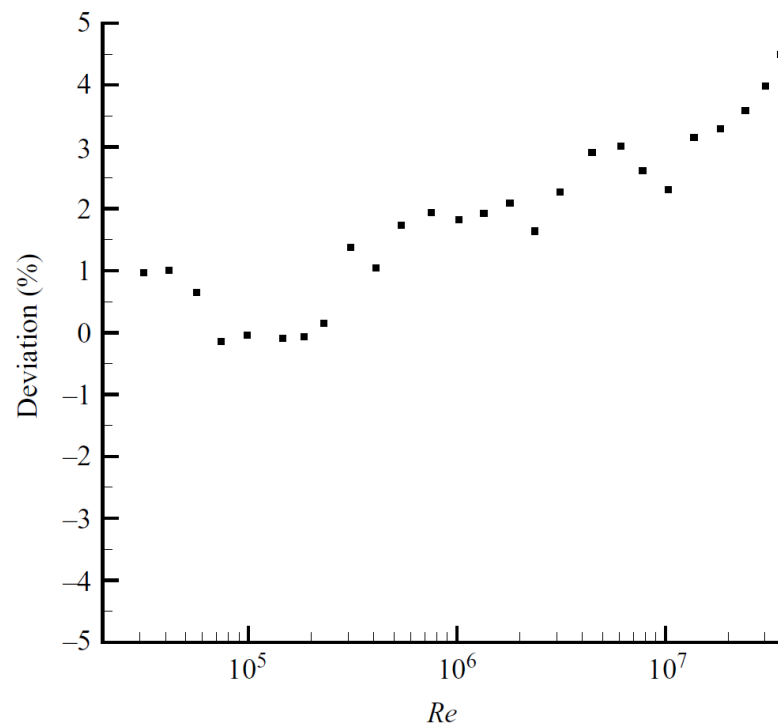


Figure 2.29: Recalculation of *SuperPipe* data using *Prandtl's "universal" friction factor relationship*. From B. J. McKeon, M. V. Zagarola, and A. J. Smits, A new friction factor relationship for fully developed pipe flow, *Journal of Fluid Mechanics*, 538:14, p. 434, reproduced with permission.

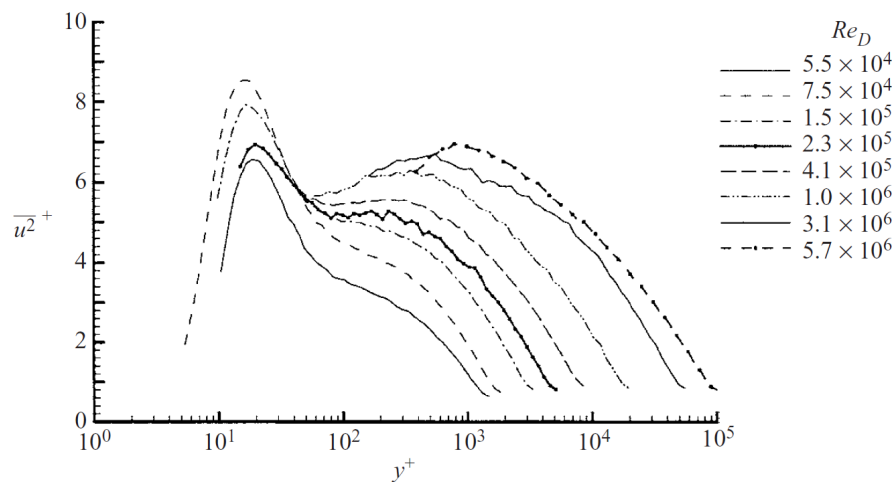


Figure 2.30: Representation of the second-order moment as a function of the normalized wall distance. From J. F. Morrison, B. J. McKeon, W. Jiang, and A. J. Smits, Scaling of the streamwise velocity component in turbulent pipe flow, *Journal of Fluid Mechanics*, 508 p. 108, reproduced with permission.

2.4 Numerical Approach to Turbulence in Pipe Flow

For experimentalists the comparison of their results with those from numerical simulations is of great importance. And of course the other way around gives a significant feedback, e.g. improved turbulence models and grid resolution. Another important fact on the inalienable necessity of developing numerical simulations is, that this method is the best way to control initial conditions on the way from laminar to turbulent pipe flow, since it is believed that transition is initiated by triggering the laminar velocity profile. Otherwise the flow state will remain laminar in time due to its linear stability. Hence, intensive work has been conducted to improve the computational boundary conditions for resolving the Navier-Stokes equation and the dynamic occurring in pipe flow, which are discussed in more details within Chapter 3.1.

A pioneering work on this topic, containing direct numerical simulations of turbulent channel flow, are performed by Kim et al. [52]. In this work they were limited to one Reynolds number ($Re_c = 3300$), but computed essential turbulence statistics, like mean and fluctuating velocity as well as higher-order statistics. The numerical results are then compared to certain experimental results showing a good general agreement for the characteristics. However, some inconsistencies in the near wall region are uncovered. Possible sources for those discrepancies can be related to the experimental estimation of the wall shear stress u_τ and heat-conduction problems between the probe and the wall during the measurements. Also the developing length of the flow, which is until now a great problem in experiments even for pipe flow, turned out to be a problem. With the knowledge on this problems the scientist in the field of numerical simulations were encouraged, and hence a lot of computations and improvements are conducted. Since the numerical procedures and the history of simulating turbulence either in channel or pipe flow is not in focus here only the most outstanding studies are presented generated since the last decade.

The experimental observations by Darbyshire and Mullin [19] initiated a detailed numerical investigation by Faisst and Eckhardt [29]. They aim on the possibility to relate the special behavior of pipe flow, where on one side transition to turbulence can be triggered by initial conditions and on the other side not, to a formation of a chaotic saddle in the phase space of the system. The out coming result is a distribution of turbulent lifetimes, which follow an exponential law. This behavior is depicted in Figure 2.31. From this Figure 2.31 we see, that the probability of turbulence is decaying with the lifetime t . This means the turbulent flow state is possibly collapsing into the laminar flow state. Here, the lifetime distribution is following an exponential behavior. This shown numerical observations and the conclusions, which were drawn by Faisst and Eckhardt [29], build the basis for the groundbreaking experimental results obtained by Hof et al. [39],

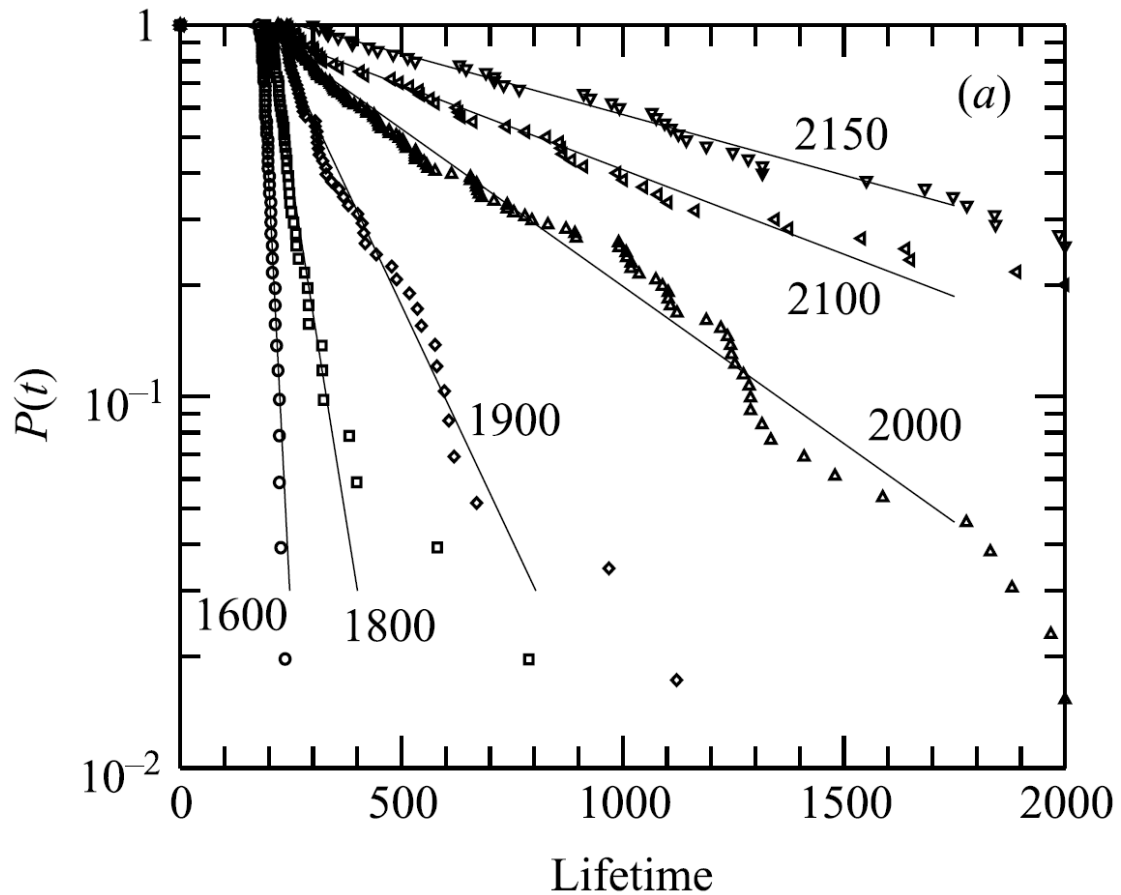


Figure 2.31: The probability $P(t)$ of decaying turbulence is shown as a function of the turbulent lifetimes for six different transitional Reynolds numbers. From H. Faisst and B. Eckhardt, Sensitive dependence on initial conditions in transition to turbulence in pipe flow, *Journal of Fluid Mechanics*, 504, p. 350, reproduced with permission.

which are described in Chapter 2.1. Another very important work is done by Wedin and Kerswell [104], who found three-dimensional traveling wave solutions for a flow through a circular pressure-driven pipe. These solutions consist of three well-defined flow features, which are

1. streamwise rolls,
2. streamwise streaks and
3. streamwise-dependent wavy structures.

A contour plot of such traveling waves for four modes ($m_0 = 3, 4, 5, 6$) is depicted in Figure 2.32. A detailed description can be found in [104]. By the help of this investigation and such sophisticated results a series of experimental observations is developing

to get a knowledge of the link between these traveling wave solutions and the mean properties of transitional flow. Hence, the very first time Hof et al. [37] observed the discovered traveling wave solutions within a flow through a circular cross section, refer to Chapter 2.1. Next to all introduced efforts on dealing with pipe flow in a sufficient

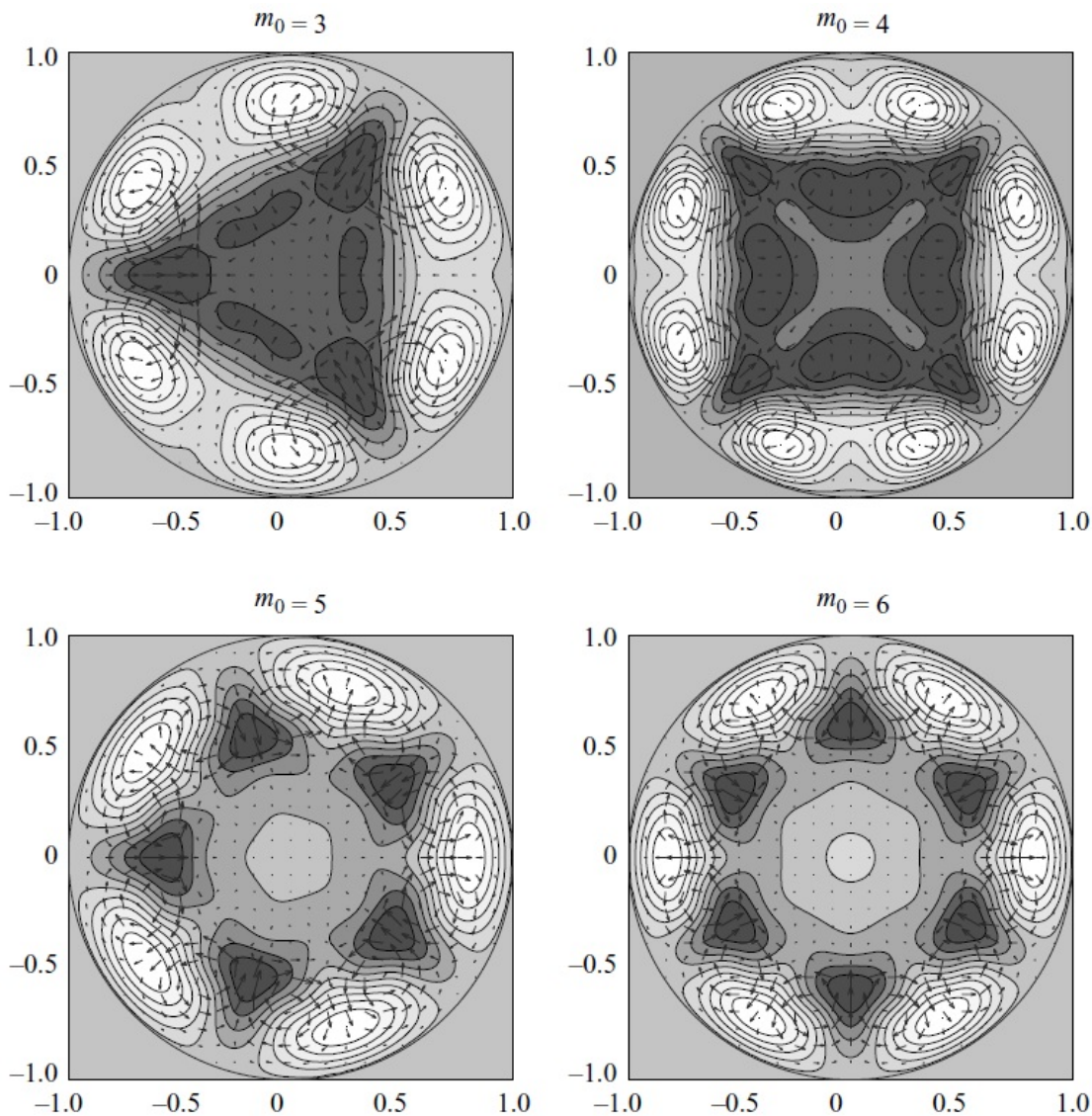


Figure 2.32: Numerical discovery of traveling wave solutions for $m_0 = 3, 4, 5, 6$ at their saddle-node bifurcation points and optimal wave number. From H. Wedin and R. R. Kerswell, Exact coherent structures in pipe flow: travelling wave solutions, *Journal of Fluid Mechanics*, 508, p. 353, reproduced with permission.

numerical way it is necessary and important for a comprehensive understanding of pipe flow turbulence to analyze and conceive the onset and nature of turbulence. The hitherto theory with the common critical Reynolds number of $Re_{crit} = 2300$, which goes back to Rotta [89], was renewed through the extraordinary work of Hof et al. [36], Hof et al. [37],

Hof et al. [38], Hof et al. [39], Hof et al. [40], de Lozar and Hof [20], Hof et al. [41], Avila et al. [5] as well as Avila et al. [4] during the last decade. Within these works localized turbulent structures, like puffs and slugs, which are responsible for the sustainment of pipe flow turbulence, were experimentally and numerically investigated. This includes the decay and proliferation mechanism of the structures as well as the spatial coupling of transiently chaotic domains, which breaks with the classical view that turbulence depends on the temporal complexity [4]. Furthermore a new critical point for the onset of turbulence was identified and is characterized through $Re_{crit} = 2040 \pm 10$. Another impressive result is the mechanism of eliminating turbulence by constantly converting energy from the mean shear into turbulent eddies [41], however, under special boundary conditions.

The presented numerical results all deal with a low Reynolds number range since it is until now very challenging, even with the today improved computer technology, to resolve turbulent dynamics for Reynolds numbers or Kármán numbers, respectively, larger than $R^+ = 5000$. The requirements for such solutions are considerable [106]. Nevertheless, Hoyas and Jiménez [44] investigate the scaling of velocity fluctuations within turbulent channel flow approaching a Reynolds number $Re_\tau = 2003$. The used procedure is a direct numerical simulation. From this DNS performance Hoyas and Jiménez [44] conclude, that an insufficient scaling of some fluctuation intensities in wall units are obtained, refer to Figure 2.33 (a) and (b). This can be a result due to an interaction of the logarithmic layer with the wall, where possibly an energy transfer between eddies and near-wall streaks take place. For a circular shaped computational domain Wu and Moin [106] present a detailed DNS analysis. Within their investigation the Kármán number is $R^+ = 1142$ corresponding to a pipe-diameter-based Reynolds number of $Re_D = 44 \times 10^3$. They state that the resulting mean velocity profiles agree well with experimental observations made at the *SuperPipe*, which is depicted in Figure 2.34.

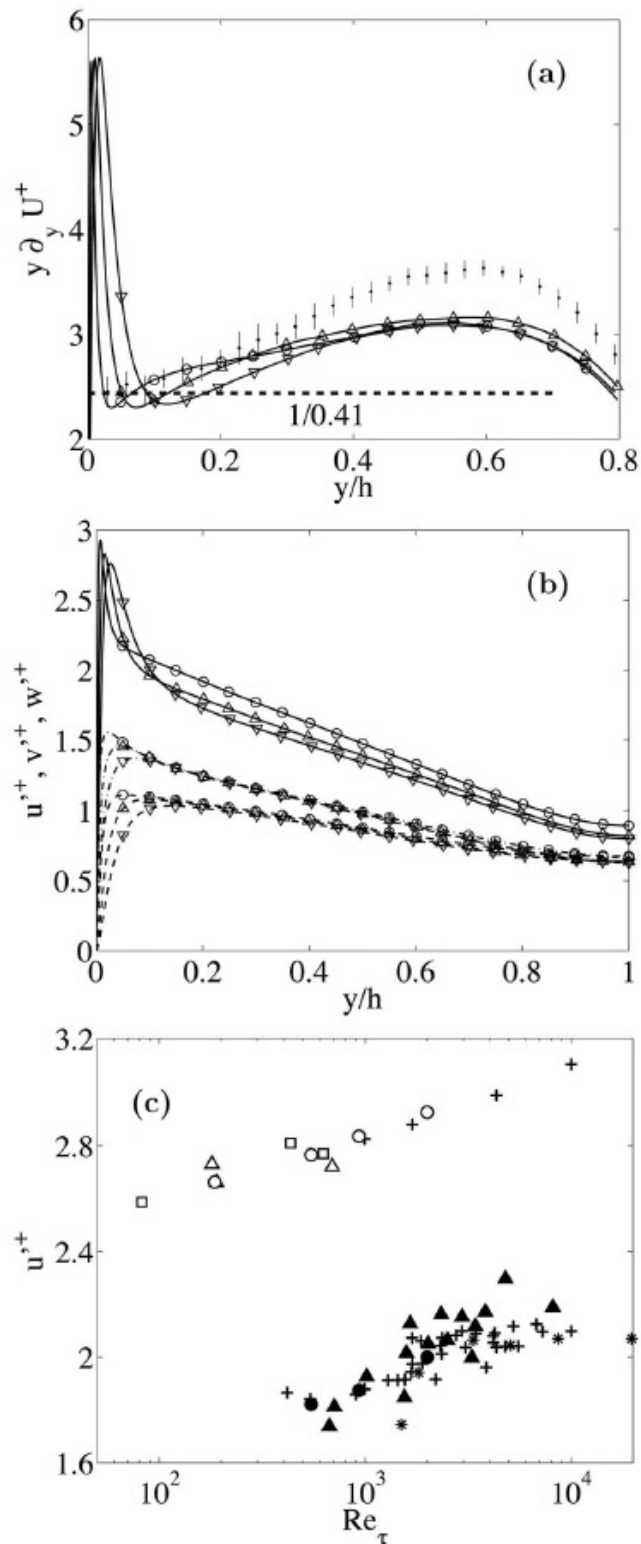


Figure 2.33: Numerical results. For a detailed description refer to Hoyas and Jiménez [44]. Reprinted with permission from [S. Hoyas and J. Jiménez. Scaling of the velocity fluctuations in turbulent channels up to $Re_\tau = 2003$. *Physics of Fluids*, 18(1), 2006]. Copyright [2006], AIP Publishing LLC.

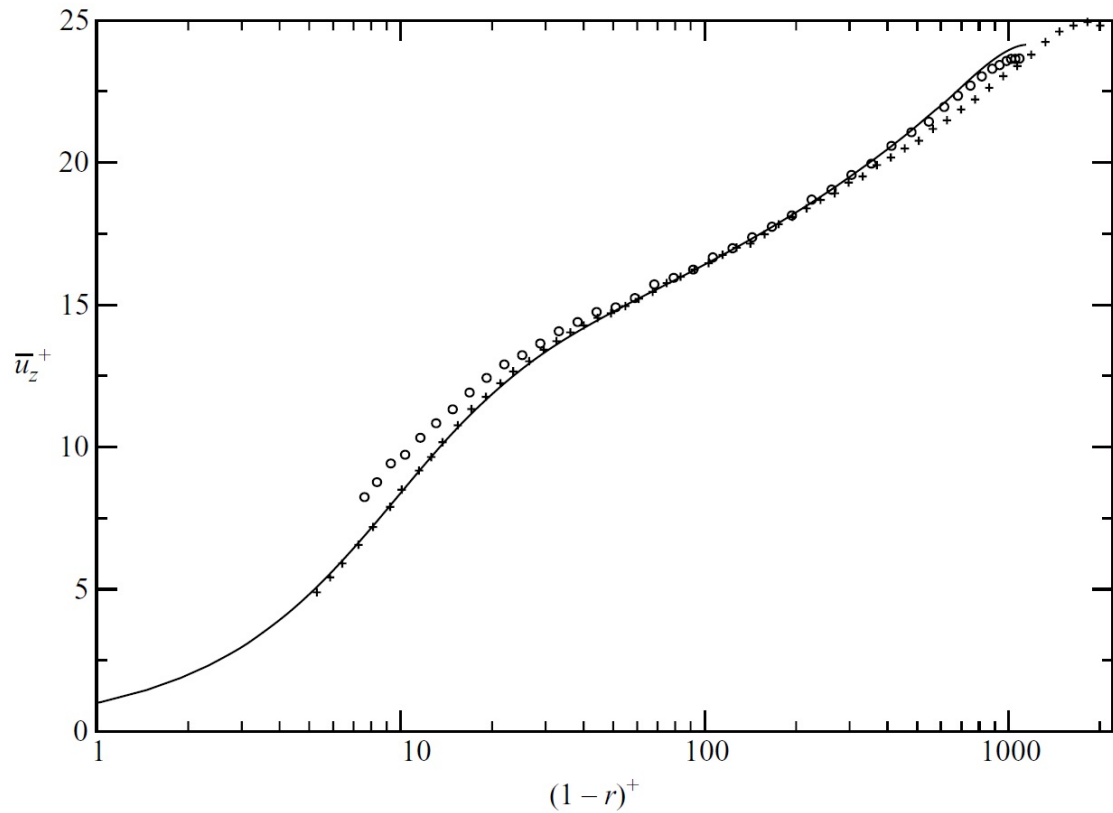


Figure 2.34: DNS result for mean velocity profile as a function of $(1-r)^+$ represented by the solid line. Symbols represent experimental results from SuperPipe [65, 110]. From X. Wu and P. Moin, A direct numerical simulation study on the mean velocity characteristics in turbulent pipe flow, *Journal of Fluid Mechanics*, 608, p. 92, reproduced with permission.

3 Theoretical Analysis and Background

As mentioned before pipe flow is one of the simplest geometries for investigating wall-bounded flows. This is due to its axial symmetry regarding the circular cross section. Hence, a large number of researchers have focused on such kind of flow system, e.g. Reynolds [85], Nikuradse [74], and a large number of research paper, underlying theory still progressing. Nevertheless, here a short summary of pipe flow theoretical analysis highlighting the field of theory on fully developed turbulent pipe flow as well as a brief overview on laminar pipe flow and the occurring transition process is presented. Since this thesis includes first results on the scaling behavior of the mean and fluctuating velocity within pipe flow, a review of the underlying formula and the theoretical background is presented additionally. Further detailed reviews on the theoretical considerations concerning such kind of wall-bounded flow are given by Zagarola [108], McKeon [63], Monty [69] and Zanoun [113]. A deeper insight into the mathematical aspects can be found in the classical work of Batchelor [11] and Pope [83].

3.1 Governing Equations

Introducing experimental results in the field of fluid mechanics, especially on pipe flow turbulence, need a discussion on the fundamental equations, which describe the phenomena in a mathematical way. Here, the French mathematician and physicist *Claude L. M. H. Navier* as well as the Irish mathematician and physicist *George G. Stokes* developed a system of equations, which is represented through the following symbolic notation:

$$\frac{D\mathbf{U}}{Dt} = \rho \left(\frac{\partial \mathbf{U}}{\partial t} + \mathbf{U} \cdot \nabla \mathbf{U} \right) = -\nabla p + \mu \nabla^2 \mathbf{U} + \frac{1}{3} \mu \nabla (\nabla \cdot \mathbf{U}) + \rho \mathbf{f}, \quad (3.1)$$

where the left side of Equation 3.1 represents the local and convective acceleration term, and the right side of Equation 3.1 represents a summation of acting pressure forces, diffusion, shear forces and external forces acting on the observed fluid element. Equation 3.1 is of course named in memory of both pioneering scientists, who have established and

enhanced the set of equations, the *Navier-Stokes* equations.

If the flow is now supposed to be Newtonian and incompressible, which is represented through the continuity equation

$$\nabla \cdot \underline{U} = 0, \quad (3.2)$$

and restricted to no action of body forces, the *Navier-Stokes* equation is reduced to

$$\frac{D\underline{U}}{Dt} = \frac{\partial \underline{U}}{\partial t} + (\underline{U} \cdot \nabla)\underline{U} = -\frac{\nabla p}{\rho} + \nu \nabla^2 \underline{U} \quad (3.3)$$

where \underline{U} is the instantaneous velocity vector, p is the pressure in the flow field, ρ is the density of the fluid and ν is its kinematic viscosity.

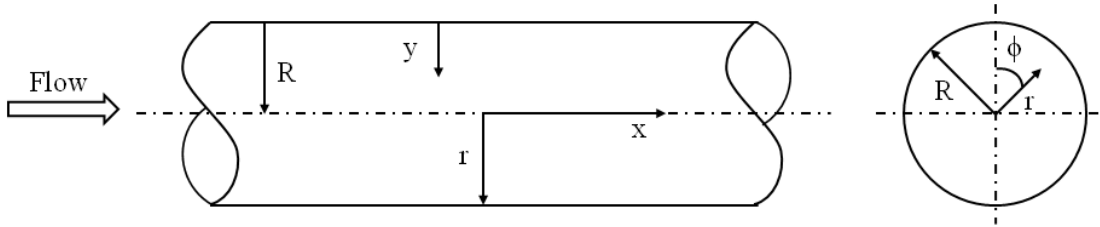


Figure 3.1: General cylindrical coordinate system for the present pipe flow investigations.

It is common, due to the circular geometry of a pipe with the radius R , to define a cylindrical co-ordinate system, which is presented in Figure 3.1, and to apply it onto the both equations - continuity (Equation 3.2) and *Navier-Stokes* equation (Equation 3.3). The transformation from Cartesian to cylindrical co-ordinates is therefor defined by:

$$\nabla_{(r,\phi,x)} f = \left(\begin{array}{c} \frac{\partial f}{\partial r} \\ \frac{1}{r} \frac{\partial f}{\partial \phi} \\ \frac{\partial f}{\partial x} \end{array} \right) \quad (3.4)$$

Hence,

$$\frac{1}{r} \frac{\partial(r u_r)}{\partial r} + \frac{1}{r} \frac{\partial u_\phi}{\partial \phi} + \frac{\partial u_x}{\partial x} = 0 \quad (3.5)$$

is the resulting continuity equation in cylindrical co-ordinates. The resulting set of equations regarding the *Navier-Stokes* equation for all three dimensions, i.e. streamwise (x), radial (r) and circumferential (ϕ), yield to:

streamwise direction:

$$\frac{\partial u_x}{\partial t} + u_r \frac{\partial u_x}{\partial r} + u_\phi \frac{\partial u_x}{\partial \phi} + u_x \frac{\partial u_x}{\partial x} = -\frac{1}{\rho} \frac{\partial p}{\partial x} + \nu \left(\frac{\partial^2 u_x}{\partial r^2} + \frac{1}{r} \frac{\partial u_x}{\partial r} + \frac{1}{r^2} \frac{\partial^2 u_x}{\partial \phi^2} + \frac{\partial^2 u_x}{\partial x^2} \right) \quad (3.6)$$

radial direction:

$$\begin{aligned} \frac{\partial u_r}{\partial t} + u_r \frac{\partial u_r}{\partial r} + \frac{u_\phi}{r} \frac{\partial u_r}{\partial \phi} - \frac{u_\phi^2}{r} + u_x \frac{\partial u_r}{\partial x} = -\frac{1}{\rho} \frac{\partial p}{\partial r} + \nu \left(\frac{\partial^2 u_r}{\partial r^2} + \frac{1}{r} \frac{\partial u_r}{\partial r} - \frac{u_r}{r^2} \right. \\ \left. + \frac{1}{r^2} \frac{\partial^2 u_r}{\partial \phi^2} - \frac{2}{r^2} \frac{\partial u_\phi}{\partial \phi} + \frac{\partial^2 u_r}{\partial x^2} \right) \end{aligned} \quad (3.7)$$

circumferential direction:

$$\begin{aligned} \frac{\partial u_\phi}{\partial t} + u_r \frac{\partial u_\phi}{\partial r} + \frac{u_\phi}{r} \frac{\partial u_\phi}{\partial \phi} + \frac{u_r u_\phi}{r} + u_x \frac{\partial u_\phi}{\partial x} = -\frac{1}{\rho r} \frac{\partial p}{\partial \phi} + \nu \left(\frac{\partial^2 u_\phi}{\partial \phi^2} + \frac{1}{r} \frac{\partial u_\phi}{\partial r} - \frac{u_\phi}{r^2} \right. \\ \left. + \frac{1}{r^2} \frac{\partial^2 u_\phi}{\partial \phi^2} + \frac{2}{r^2} \frac{\partial u_r}{\partial \phi} + \frac{\partial^2 u_\phi}{\partial x^2} \right) \end{aligned} \quad (3.8)$$

Since the focus within this thesis is on turbulent pipe flow it is useful to separate the average and fluctuating part of the fluid velocity by the help of *Reynolds' decomposition*, where $U_x = U + u'$, $U_r = V + v'$, $U_\phi = W + w'$ and $p = P + p'$ represents the sum of both parts. Even the time-average (denoted by an overbar) of the equations is formed and the flow field is considered as fully-developed in streamwise direction

$$\frac{\partial}{\partial x} = 0, \quad (3.9)$$

and axisymmetric in circumferential direction

$$\frac{\partial}{\partial \phi} = 0, \quad (3.10)$$

the full set of *Navier-Stokes* equations is simplified to:

$$\frac{\partial(\overline{U + u'})}{\partial t} + \overline{V + v'} \frac{\partial \overline{U + u'}}{\partial r} = -\frac{1}{\rho} \frac{\partial \overline{P + p'}}{\partial x} + \nu \left(\frac{\partial^2 \overline{U + u'}}{\partial r^2} + \frac{1}{r} \frac{\partial \overline{U + u'}}{\partial r} \right) \quad (3.11)$$

$$\begin{aligned} \frac{\partial(\overline{V + v'})}{\partial t} + \overline{V + v'} \frac{\partial \overline{V + v'}}{\partial r} - \frac{\overline{(W + w')}}{r} &= -\frac{1}{\rho} \frac{\partial \overline{P + p'}}{\partial r} + \nu \left(\frac{\partial^2 \overline{V + v'}}{\partial r^2} \right. \\ &\left. + \frac{1}{r} \frac{\partial \overline{V + v'}}{\partial r} - \frac{\overline{V + v'}}{r^2} \right). \end{aligned} \quad (3.12)$$

Applying all simplifications on the continuity equation, Equation 3.5 yields to

$$\frac{1}{r} \frac{\partial(r \overline{V + v'})}{\partial r} = 0. \quad (3.13)$$

The obtained results are the Reynolds-averaged *Navier-Stokes* (RANS) equations, with the continuity equation for the mean flow

$$\frac{1}{r} \frac{\partial(r V)}{\partial r} = 0, \quad (3.14)$$

whereas the RANS equations yield in streamwise direction:

$$\frac{1}{\rho} \frac{\partial P}{\partial x} = \frac{1}{r} \frac{\partial}{\partial r} \left(r \left[-\overline{u'v'} + \nu \frac{\partial U}{\partial r} \right] \right), \text{ and} \quad (3.15)$$

radial direction:

$$\frac{1}{\rho} \frac{\partial P}{\partial r} = -\frac{1}{r} \frac{\partial(r \overline{v'^2})}{\partial r} + \frac{\overline{w'^2}}{r}, \quad (3.16)$$

for the flow through a pipe, which is considered to be smooth-walled. At this point the turbulence is linked to the mean flow through the Reynolds stress term $\overline{u'_i u'_j}$. A more detailed description of the above derivation can be found in the work of Batchelor [11] and Pope [83].

If now the appropriate boundary conditions are applied to the above system, e.g. at the

centerline of the pipe, where $r = 0$ the following results can be derived:

$$\frac{\partial U}{\partial r} = 0, \text{ and} \quad (3.17)$$

$$\overline{u'v'} = \overline{v'^2} = \overline{w'^2} = 0, \text{ and} \quad (3.18)$$

at the pipe wall, where $r = R$, the equations are simplified by the integration in radial direction to:

$$\frac{\partial U}{\partial r} = \frac{R}{2} \frac{1}{\rho\nu} \frac{\partial P}{\partial x}, \text{ and} \quad (3.19)$$

$$\overline{u'v'} = \overline{v'^2} = \overline{w'^2} = 0. \quad (3.20)$$

With the convention, that the wall shear stress τ_w is defined as

$$\tau_w = -\frac{D}{4} \frac{dP}{dx}, \quad (3.21)$$

which shows that the wall shear stress is constant along the pipe, and that the wall friction velocity u_τ , chosen as the appropriate scaling parameter, is defined as

$$u_\tau = \sqrt{\frac{\tau_w}{\rho}}, \quad (3.22)$$

Equation 3.19 can be rearranged to

$$\frac{\partial U}{\partial r} = -\frac{1}{\nu} \frac{\tau_w}{\rho} = -\frac{u_\tau^2}{\nu}. \quad (3.23)$$

A more general form to investigate the Reynolds stress term $\overline{u'v'}$ can be formulated, when Equation 3.15 is integrated from the centerline to r . This yields

$$-\frac{r}{R} u_\tau^2 = -\overline{u'v'} + \nu \frac{\partial U}{\partial r}. \quad (3.24)$$

Here, the first term on the right side of Equation 3.24 represents the Reynolds shear-stress or the effect of the turbulent motion, and the second term represents the effect of the viscous stress. The left side of Equation 3.24 represents the effect of the pressure gradient, which is constant along the pipe. From this derivation it is obvious, that if one has knowledge of the mean flow field the Reynolds shear-stress can be estimated, and vice versa. But this has to be treated with great care, e.g. due to measurement inaccuracies. Now, it is also common to redefine the origin to be the wall, which is depicted in Figure 3.1, and thus Equation 3.24 can be rewritten in the conventional form

$$\left(1 - \frac{y}{R}\right)u_{\tau}^2 = -\overline{u'v'} + \nu \frac{\partial U}{\partial y}. \quad (3.25)$$

This formulation is exact and gives all information on the entire mean flow field. Note that in the case of a zero Reynolds shear-stress term Equation 3.25 can be integrated and hence results in the laminar Poiseuille velocity profile.

Therewith, the development of the classical fully developed turbulence in pipe flow is derived from the full set of *Navier-Stokes* equations with the transformation from Cartesian to cylindrical coordinates.

3.2 General Aspects on Pipe Flow

Basically, the motion within a three-dimensional flow field can be described with the velocity vector \underline{U} as well as the pressure p and the temperature T . Here, \underline{U} is defined as:

$$\underline{U} = \vec{e}_x u + \vec{e}_y v + \vec{e}_z w,$$

with three components u , v and w in Cartesian co-ordinates and the unit vectors \vec{e}_x , \vec{e}_y and \vec{e}_z . All five parameter, i.e. $\vec{e}_x u$, $\vec{e}_y v$, $\vec{e}_z w$ as well as p and T , are estimated using the following equations:

- continuity equation (conservation of mass),
- three momentum equations (conservation of momentum) and
- energy equation (conservation of energy).

3.2.1 Laminar Pipe Flow

The aforementioned equations, which are discussed within Chapter 3.1, can be simplified in the case of axial symmetric flow, which is for a circular cross section well known as *Hagen-Poiseuille-Flow* or laminar pipe flow. Hence, the velocity in radial and circumferential direction can be set to zero ($r = \phi = 0$). Note that a co-ordinate transformation from Cartesian to cylindrical co-ordinates is useful, which is even described in Chapter 3.1. Additionally, the remaining velocity component, which is the one in axial direction, depends only on the radius R of the pipe: $u(r)$. Furthermore, the pressure at every cross-section is a constant force. And if these assumptions are applied on the full *Navier-Stokes-Equations*, Equation 3.6 - 3.8, the system is reduced to one resulting equation, which is the one in axial direction:

$$\mu \left(\frac{\partial^2 u_x}{\partial r^2} + \frac{1}{r} \frac{\partial u_x}{\partial r} \right) = \frac{\partial p}{\partial x}. \quad (3.26)$$

If the no-slip boundary condition $u(r = R) = 0$ is applied as well, the following exact solution for the velocity profile can be derived:

$$u_x(r) = u_{max} \left(1 - \frac{r^2}{R^2} \right). \quad (3.27)$$

The result is the commonly known parabolic velocity profile, which is depicted in Figure 3.2 and marked with character "a".

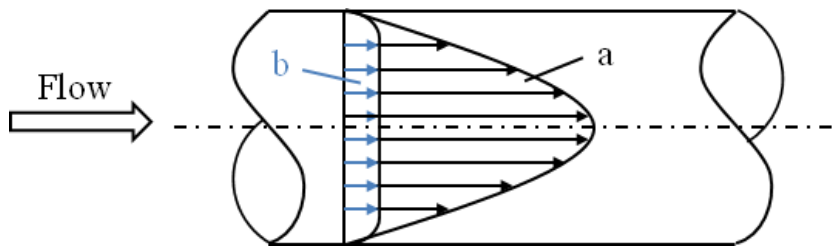


Figure 3.2: Schematic representation of a) developed laminar and b) fully turbulent velocity profile.

Since laminar pipe flow is not the focus within this thesis, no further details on the characteristic behavior are presented. Nevertheless, there exist several numerical and experimental research work on this topic, e.g. Hornbeck [43], Friedmann et al. [31], Huang and Chen [45] and Durst et al. [24], where this is such a brief selection.

3.2.2 Laminar-to-Turbulent Transition

With the beginning of the laminar-to-turbulent transition the flow yields an intermittent character. This property can be imagined as laminar and turbulent spots over the cross section and length of the pipe, which exist beside each other at the same time. To characterize this flow state the intermittency factor γ is established, which describes the turbulent spot time at the observed point within the flow. Hence, for persisting turbulence $\gamma = 1$ is valid and for persisting laminar flow $\gamma = 0$ is valid. To document such an intermittent behavior of the flow Rotta [89] analyzed flow data for a number of varying Reynolds numbers. The result is presented in Figure 3.3, where γ is related to the development length x/d for Reynolds numbers between $Re = 2300$ and $Re = 2600$.

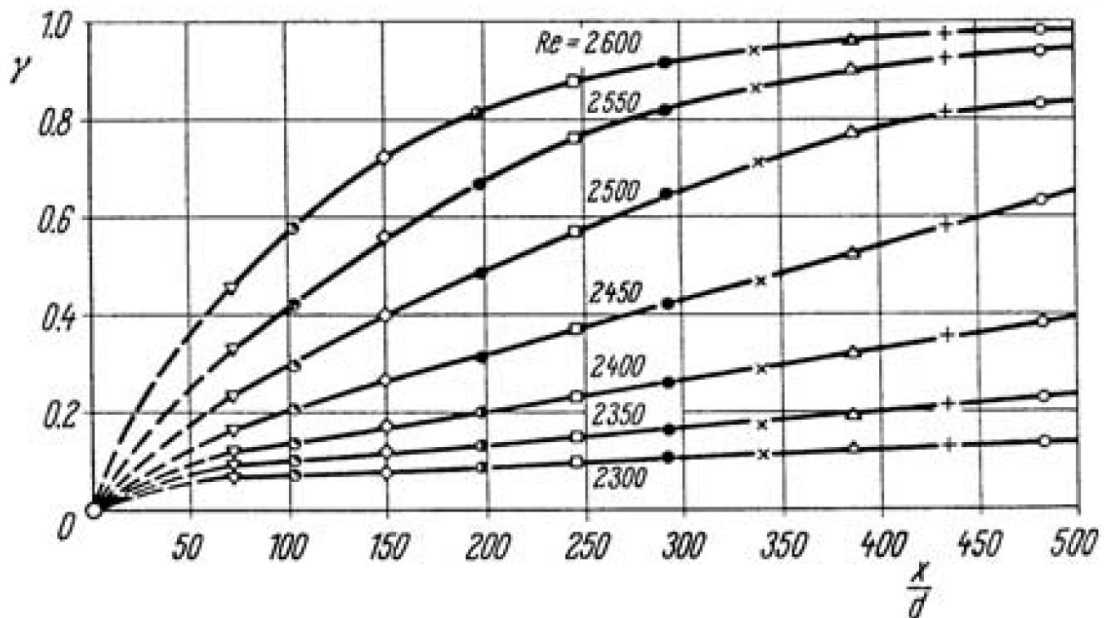


Figure 3.3: .

]Overview of intermittency factor γ for different Reynolds numbers as a function of the development length. From [89] and [90].

It is obvious from Figure 3.3 that the intermittency factor increases with increasing Reynolds number for fixed x/d , and that γ continuous increases, respectively, for a fixed Reynolds number until it reaches the maximum value of $\gamma = 1$. If the fixed Reynolds number is close to the critical Reynolds number (Re_{crit}) the length for the full development of turbulence can be more than 1000 d.

The transition process itself is mainly influenced by small disturbances, e.g. resulting from the inlet. Such disturbances can be damped if the influence of the viscosity is high and the Reynolds number is sufficient low enough. For a decreasing influence of the

viscosity effect and an increasing Reynolds number these disturbances grow and therefore initiate the transition to full turbulence. This process is finished after a certain length. Thereafter the fully developed turbulent flow state is approached, and the governing equations to describe the flow field are presented in Chapter 3.1.

3.3 The Structure of the Turbulent Boundary Layer

As mentioned earlier the turbulent boundary layer is evolving from the inlet flow state to the fully laminar flow state with the beginning transition until the fully developed flow state is approached. When this flow state is developed the turbulent boundary layer is grown from the wall to the core region of the pipe. Hence, the turbulent boundary layer can be classified into different regions [99], which is schematically depicted in Figure 3.4. The first region is the inner region, which is also commonly known as the

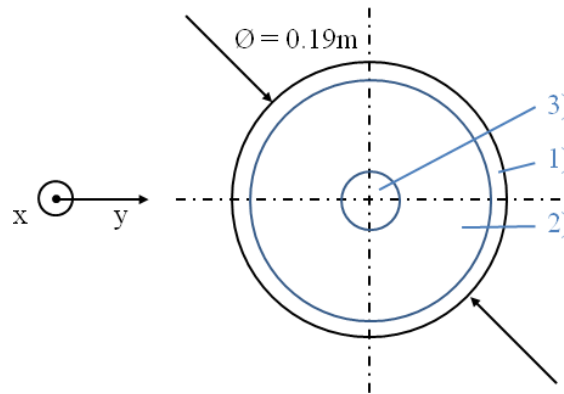


Figure 3.4: Schematic overview about the structure of turbulent boundary layer. A similar figure can be found in Barenblatt et al. [10].

viscous sublayer (Figure 3.4 - 1)). This part of the boundary layer is nominally influenced by the viscous force. The core region around the axis of the pipe or even named as the outer region of the boundary layer (Figure 3.4 - 3)), is dominated by the turbulent stress. Hence, the influence of the viscous force is negligible. Due to the symmetry requirements of the circular shaped cross section the pipe centerline characterizes the outer end of the boundary layer. And, which is obvious from Figure 3.4 there is a third region between the inner and the core region of the pipe, which is called logarithmic layer or intermediate part of the boundary layer (Figure 3.4 - 2)). All three regions can be treated separately due to the influence of the viscous force and are very important with respect to the scaling of the mean velocity profile. In accordance to Figure 3.4 a more detailed classification of the three main parts as well as some additional components, i.e. for a better representation due to the mean flow scaling, forming the turbulent boundary

layer is presented in Figure 3.5. Similar illustration can be found in the work of McKeon [63] and Monty [69] for pipe flow and channel flow, respectively. From Figure 3.5 we see

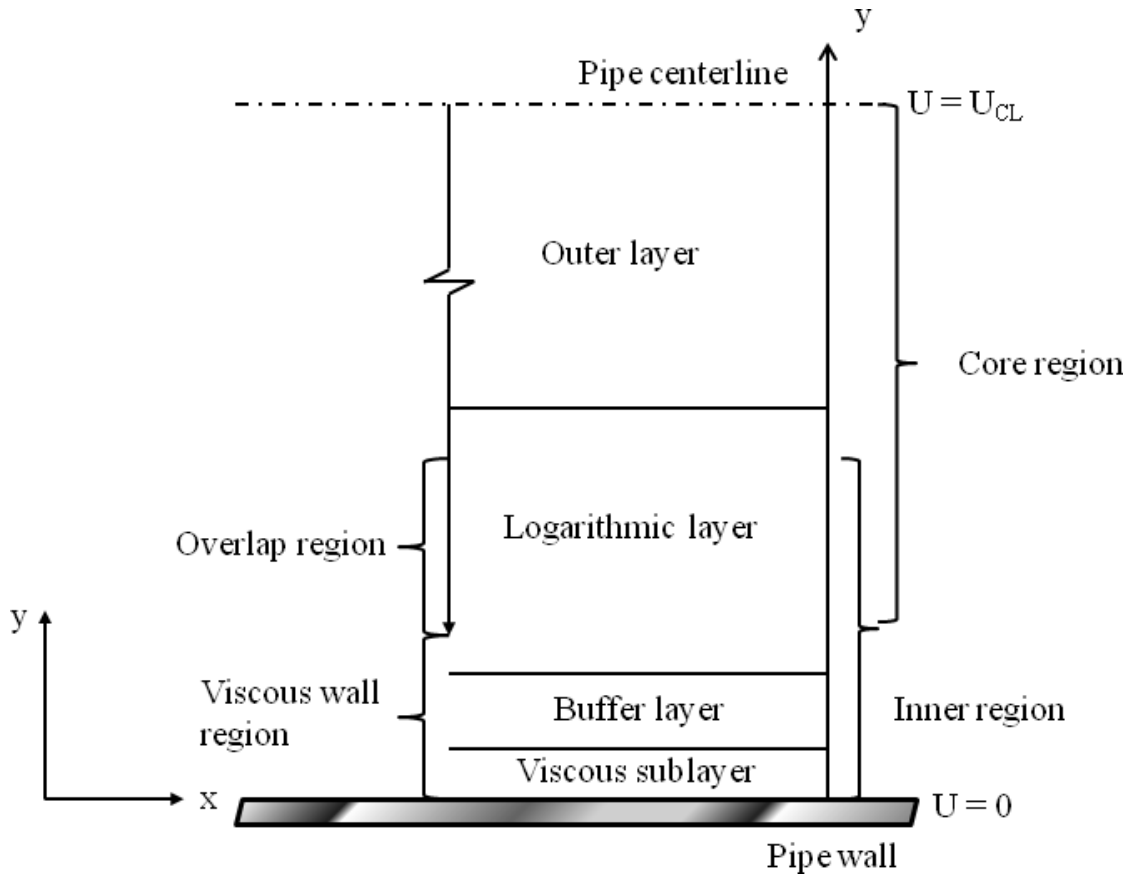


Figure 3.5: Schematic representation of various regions occurring in fully developed turbulent pipe flow.

that the inner region of the turbulent boundary layer is formed by the viscous sublayer or linear region ($y^+ < 5$) and the buffer layer, which is supposed to represent the region of $5 \leq y^+ \leq 30$, as well as the logarithmic layer. The core region or outer layer extends the normalized wall distance y^+ from 50 up to the centerline of the pipe.

All above described and depicted layers and regions as well as their defining properties are additionally listed in Table 3.1 to give a direct overview and the possibility to compare them. This is related to a presentation of Pope [83]. Hence, the mean flow field within the distinct regions, mainly viscous sublayer, buffer layer, logarithmic layer and outer layer, is described by the help of different underlying formulations, which are presented in the following. This mean flow scaling is as already discussed a highly debated topic in the fluid mechanics community. To support the ongoing discussion some first results from the new CoLaPipe are presented as well in Chapter 6.6.

Table 3.1: Defining properties of wall regions and layers.

Region	Position	Property/Remark
Viscous sublayer	$y^+ \geq 5$	Viscous force dominates Reynolds shear-stress
Buffer layer	$5 < y^+ < 30$	Region between viscous sublayer and logarithmic layer
Viscous wall region	$y^+ < 50$	Significant viscous contribution to shear stress
Inner region	$y/R < 0.1$	Dominant properties u_τ and y^+
Outer layer	$y^+ > 50$	Viscous force is negligible
Logarithmic layer	$y^+ > 30, y/R < 0.3$	Validity of logarithmic law

3.3.1 The Viscous Sublayer

Within the inner region, near the wall, the viscous force is the predominant force and the velocity gradient $\partial u/\partial y$ is very large. Hence, the velocity in the vicinity of the wall can be expressed by the following functional relation:

$$U = f(y, \nu, u_\tau),$$

where y is the distance from the wall, ν is the kinematic viscosity and u_τ represents the wall friction velocity. From Equation 3.25 and with the aforementioned dependencies the linear behavior of the velocity gradient close to the wall, valid for $y^+ \leq 5$, can be derived and expressed, like

$$U^+ = y^+. \quad (3.28)$$

Here, the notation $(^+)$ describes the dimensionless form, where the appropriate scaling parameter is the wall friction velocity u_τ . This relation is postulated throughout the well-known work of von Kármán [99] even with the limitation of y^+ . Prandtl and Betz [84] extends this region up to $y^+ \leq 11.5$ on the basis of his experimental results. Despite these different assumptions for the validity of the linear law of the wall the CoLaPipe experimental results give a good representation of the linear behavior of the mean flow

close to the wall. This is depicted and described in Chapter 6.6. Note that the spatial resolution of this very thin layer is restricted to the lower bound of the investigated Reynolds number range since the viscous sublayer diminishes with increasing Reynolds number. But not only the good agreement is presented, also the clear deviation from this scaling for $y^+ > 10$ has to be considered and is shown. This is pointed out as well through the numerical results obtained by Kim et al. [52], which is depicted in Figure 3.6 and which supports the statement of von Kármán [99].

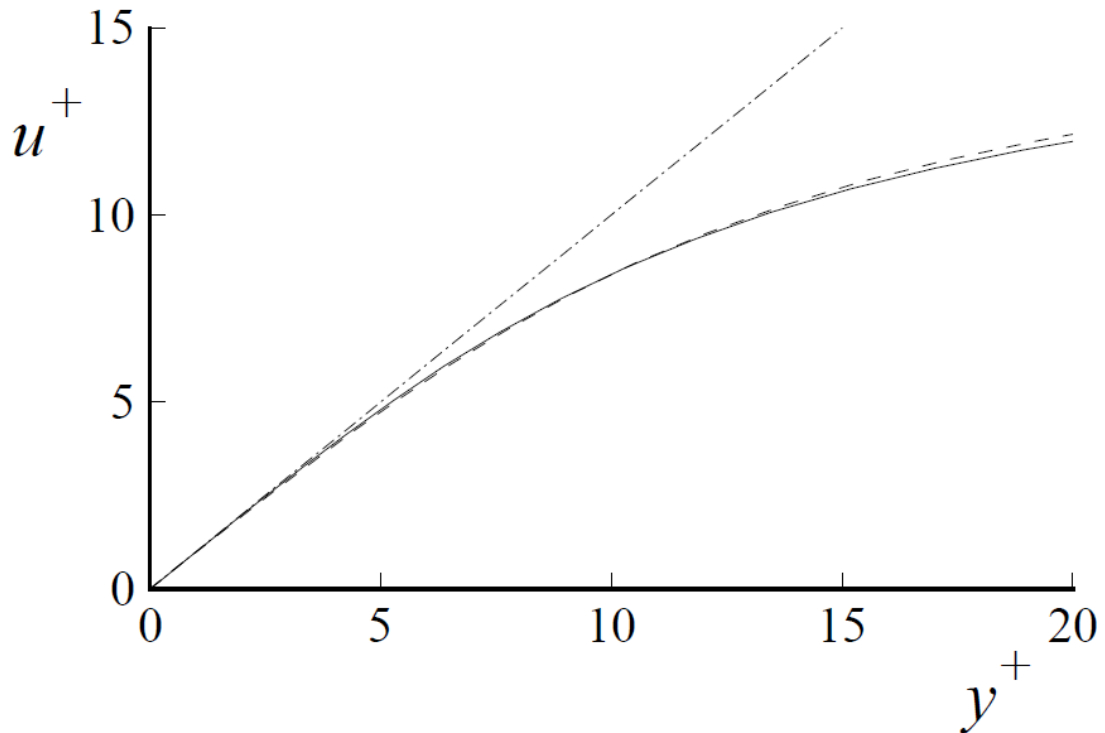


Figure 3.6: Linear-linear plot of the normalized mean velocity profile scaled on the wall friction velocity u_τ obtained by DNS. From [83].

3.3.2 The Buffer Layer

The buffer layer acts as a direct coupling between the viscous sublayer ($y^+ < 5$) and the logarithmic region ($y^+ > 30$, $y/R < 0.3$), where the scaling laws for both different regions are not appropriate. This behavior is due to the decreasing influence of the viscous force and the increasing effects with regard to the turbulence-dominated parts of the flow. Here, von Kármán [99] has developed a relation to indicate the scaling behavior of the

mean flow within this transitional layer:

$$U^+ = 5 \ln y^+ - 3.05 \quad (3.29)$$

Since the scaling in the vicinity of the wall is of great interest among all researchers within this field of fluid mechanics, several other relations are proposed. These can be found together with a detailed discussion in the work of Zanon [113], and therefore here no further details are presented.

3.3.3 The Logarithmic Region of the Boundary Layer

The scaling of the mean flow within the logarithmic region of a turbulent boundary layer separates researchers into two camps. One supports the general opinion of a universal scaling behavior within the logarithmic region represented by Equation 3.30, and the other, who propose a power-law scaling. The contradiction can be retraced easily due to a broad variation of the proposed scaling parameter. Details on this can be found elsewhere, e.g. Zagarola and Smits [110], Zanon [113], George [32], Nagib and Chauhan [72] and Marusic et al. [62]. Especially the work of George [32] put the ongoing discussion on the "right" scaling of the mean flow velocity in a more general context, where the influence of the correct estimation of the scaling parameter have a great influence on engineering work, like in aircraft design for instance. Despite the discussion on the universality of the scaling parameter and the validity for the three wall-bounded flow systems, i.e. pipe and channel flow as well as TBL, the common relation for the scaling of the mean velocity within the logarithmic region of a turbulent boundary layer in pipe flow is

$$U^+ = \frac{1}{\kappa} \ln(y^+) + B. \quad (3.30)$$

Within Equation 3.30 U^+ is the mean velocity scaled on the wall friction velocity u_τ , denoted as inner scaling, y^+ is the normalized wall distance also scaled on inner variables, and κ as well as B are empirical estimated constants, which are believed to be Reynolds number independent and therewith universal. Nevertheless, in recent years some considerations and estimations on various experimental data sets are conducted by McKeon et al. [65], Örlü et al. [88], Zanon [113], Zanon and Durst [114], which come to the concluding result of varying constants due to varying Reynolds numbers and experimental setups. In addition, the utilized measurement technique to resolve

the mean velocity and all depending or even necessary quantities, like the wall friction velocity u_τ , the density ρ and kinematic viscosity ν of the working fluid, plays a dominant role. However, this logarithmic region works as a bridge between the inner and the outer boundary layer, refer to the introduction of Chapter 3.3, and hence the range of its validity, remember $y^+ > 30$, $y/R < 0.3$, is also intensively discussed represented by the work of Marusic et al. [61]. For the constants κ and B in Equation 3.30 several results can be found in the literature, which are recently summarized by Örlü et al. [88] and Bailey et al. [7]. An overview is presented in Table 3.2. Due to the inconsistencies

Table 3.2: Variety of the von Kármán constant κ and the additive constant B , which are relevant in the logarithmic law, refer to Equation 3.30.

κ	B	flow type	reference	year
$0.40 \leq \kappa \leq 0.41$	5.2	TBL	Coles [18]	1956
0.384	4.17	TBL	Österlund et al. [95]	2000
0.37	3.7	channel flow	Zanoun and Durst [114]	2003
0.421	5.6	pipe flow	McKeon et al. [65]	2004
0.386	5.6	pipe flow	Monty [69]	2005

among the scientific work for almost 60 years of research on this topic, alternative scaling laws for the mean flow velocity profile have been developed. As already mentioned George [32] has proposed a power-law scaling for the logarithmic region valid for TBL only, whereas the logarithmic scaling holds for pipe and channel flow, respectively. In contrast, Barenblatt [9] has analyzed and conducted pipe flow experiments and finally draw the conclusion of a Reynolds number depending power-law scaling. At this point no further efforts regarding alternative mean flow scaling are made since detailed discussions can be found in the work of [108], Zanoun [113] and George [32], as well as this thesis will not support an intensive debate on whether the mean velocity scales on the logarithmic law or a power-law. The focus is on the introduction of a new high Reynolds number pipe flow test facility and some first results.

3.3.4 The Outer or Core Region of the Boundary Layer

With increasing distance from the wall towards the core region the influence of the viscosity becomes negligible, and the velocity gradient becomes smaller. Hence, the scaling for the mean velocity is different compared to the inner region. A valid formulation is considered by von Kármán [99] as well as Millikan [68], which is called the velocity defect

law:

$$\frac{U_c - U}{u_\tau} = g(\eta). \quad (3.31)$$

Here, U_c is the centerline velocity, u_τ is the wall friction velocity and $\eta = r/R$ for pipes. If similarity rules are applied to Equation 3.31 the following dimensionless relation can be derived:

$$\frac{U_c - U}{u_\tau} = \frac{1}{\kappa} \left[\ln \left(1 - \sqrt{\frac{r}{R}} \right) + \sqrt{\frac{r}{R}} \right]. \quad (3.32)$$

Although, von Kármán [99] as well as Millikan [68] and also other scientist investigated the mean velocity scaling in the core region of a pipe it was and is not that interesting as the inner and overlap (logarithmic) region for researchers since the important processes, like turbulent kinetic energy production and dissipation, are initiated in the vicinity of the wall. Nevertheless, over the last eighty-five years certain mean velocity scaling relations are developed and a representative summarization is presented in Zanoun [113].

4 The Design Process of the CoLaPipe

The design and the design process for every experimental setup has to be well considered in all fields of interest. In the case of the CoLaPipe the laboratory space of $40\text{ m} \times 15\text{ m} \times 6\text{ m}$ and the laws regarding emergency exits and fire loads were essential limits, which defined the major physical dimensions, i.e. the length and the height, of the setup. Other boundary conditions, i.e. pipe diameter and maximum Reynolds number, are results from an intensive literature survey, refer to Chapter 2, and even preliminary studies, which are presented in Chapter 1.3.

The resultant CoLaPipe is a high Reynolds number test facility ($Re_m \leq 1.5 \times 10^6$) accounting for fundamental research, e.g. a contribution to understanding the physical processes and dynamics of turbulence. It supports also industrial projects, e.g. investigations on flow meter for *AVL List GmbH* and first collaboration with *Texas Instruments Incorporated*.

Figure 4.1 depicts all wind tunnel components described explicitly in the following sections, i.e. test sections, settling chamber, inlet contraction, power assembly and heat exchanger. The corners provided with guide vanes are purchased parts and therefore not specified in detail.

4.1 Pipe Test Sections

Based on the constructive form of the CoLaPipe, which is closed-return, the test facility provides two test sections (refer to Figure 4.1). One is attached to the blower suction side, and the second is mounted on the delivery side of the blower (return line). Both test sections are made of high-precision smooth acrylic glass to provide good optical accessibility for the application of measuring techniques, like LDA and PIV.

The lower test section with an overall length of $L = 28\text{ m}$ has an inner diameter of $D_i = 0.19\text{ m}$. The wall thickness amounts to $s = 5\text{ mm}$. Whereas, the return line is 27 m long and has an inner diameter of $D_i = 0.342\text{ m}$. The wall thickness is $s = 4\text{ mm}$.

Both test sections are divided into segments, each segment 2 m long with additional

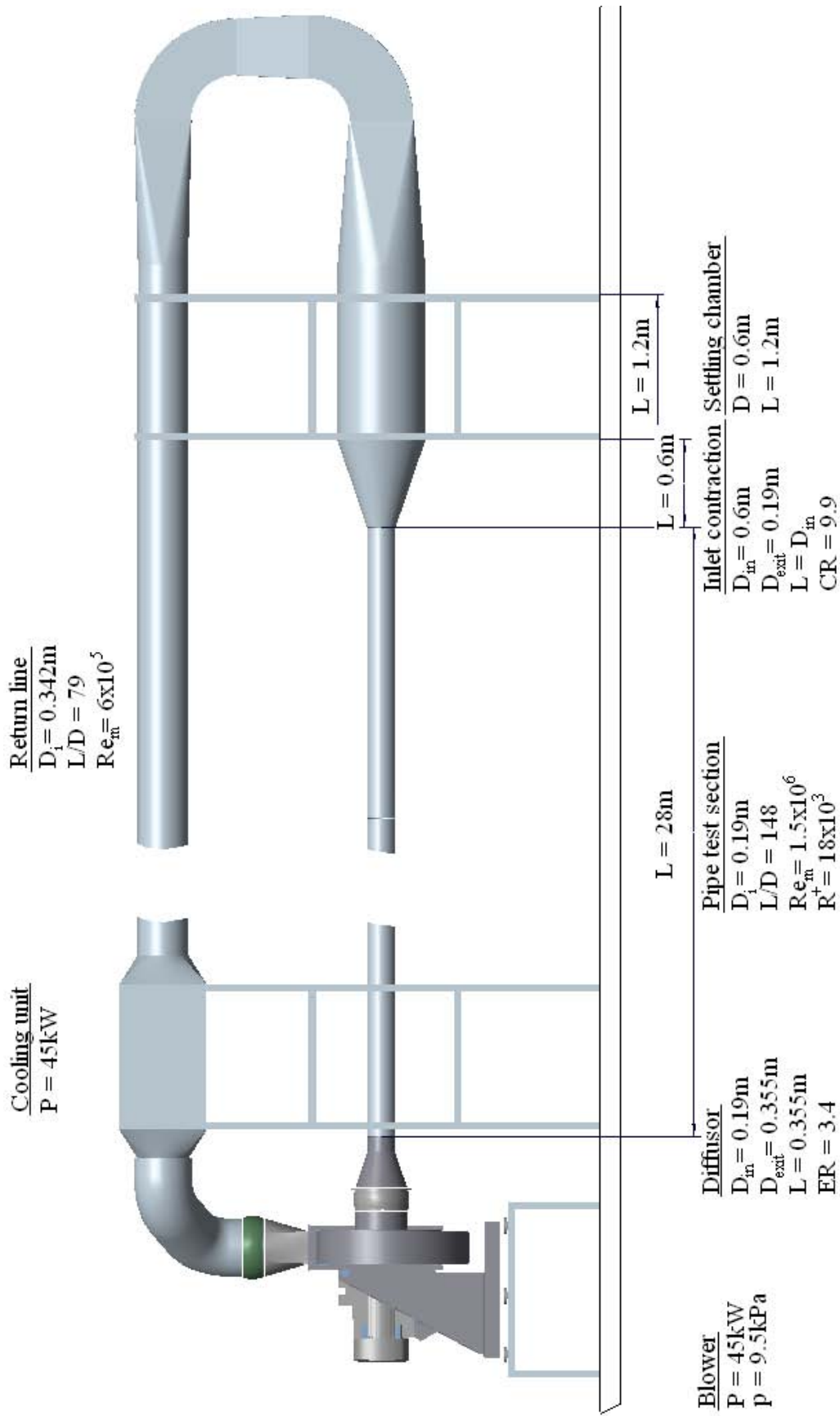


Figure 4.1: Sketch of the CoLaPipe showing all relevant parts and temperature, pressure and velocity measuring equipment (HWA). Not shown is the control panel and the traversing mechanism.

parts at the beginning and at the end ($L = 0.5\text{ m}$) working as connectors to the blower on one side, and to the inlet contraction at the other side. One specific segment ($L = 2\text{ m}$) is prepared as the main test section providing three parts with different lengths ($L_1 = 0.25\text{ m}, L_2 = 0.5\text{ m}, L_3 = 0.75\text{ m}$) allowing access for velocity and temperature measurements. This is a flexible solution for scanning the whole pipe length in relative small intervals ($L_{min} = 0.25\text{ m}$) regarding the development of pipe flow, which is discussed in more detail in the following.

4.1.1 Flow Development

To investigate turbulent pipe flow it is essential to provide a fully developed turbulent flow state. During the design process certain experimental results, e.g. the fundamental results of Nikuradse [74], the continuative experiments of Laufer [57] and the *SuperPipe* data presented in Zagarola [108] and Zagarola and Smits [110], as well as the physical space in the laboratory of the Department of Aerodynamics and Fluid Mechanics served as basic requirements. The consequence is a length-to-diameter ratio of $L/D = 148$ for the lower test section, which is calculated as following:

$$L = 28\text{ m}$$

$$D = 0.19\text{ m}$$

$$\implies L/D = \frac{28\text{ m}}{0.19\text{ m}} = 147.4 \approx \mathbf{148}.$$

The calculation of the length-to-diameter ratio for the return line is identical:

$$L = 27\text{ m}$$

$$D = 0.342\text{ m}$$

$$\implies L/D = \frac{27\text{ m}}{0.342\text{ m}} = \mathbf{78.95} \approx \mathbf{79}.$$

and finally amounts to $L/D \leq 79$. These pipe lengths seem to be sufficient as development lengths for a settled mean flow as well as for fully developed turbulence and its higher order statistics, refer also to [116].

Nevertheless, due to the differences in literature the question arises whether the development length for the actual test section ($L/D = 148$) is long enough to ensure a turbulent flow state or if not, is it possible to significantly reduce the minimum necessary length using adequate tripping devices. Common methods are sand paper stripes or diaphragms. These methods are often used and are therefore believed to be very effective, e.g. [78]. For an adequate answer on these questions intensive investigations on this topic are conducted, which are described in detail in Chapter 6 and Chapter 6.1.

4.1.2 Surface Roughness

It is generally believed since Nikuradse [75] that the flow over a surface is smooth for $k_s^+ \leq 5$, transitionally rough for $5 \leq k_s^+ \leq 70$, and fully rough for $k_s^+ \geq 70$, where the scaled roughness height k_s^+ is defined as:

$$k_s^+ = k_s \frac{u_\tau}{\nu}. \quad (4.1)$$

One requirement for the CoLaPipe is a hydraulically smooth surface for all Reynolds numbers. To meet this requirement the non-dimensional relation

$$\frac{k_s}{D} \leq \frac{5}{R^+} \quad (4.2)$$

has to be fulfilled. This results in a maximum average sand grain roughness k_s of less than $0.5 \mu\text{m}$ for a maximum Kármán number of $R^+ = 18 \times 10^3$.

Acrylic glass is a well-known material for high-quality surface properties, which can be expressed in a k_s value of $0.1 \mu\text{m}$. Therewith, we ensure smooth flow for low as well as for high Reynolds numbers (up to 1.5×10^6).

Even newer findings by Shockling et al. [91] claiming a smooth flow for $k_s^+ \leq 3.5$ are satisfied with the reported average sand grain roughness.

4.1.3 Diameter Accuracy

According to Talamelli et al. [96] the absolute accuracy of the inner pipe diameter is not very stringent as long as there are minor deviations along the pipe. Here, the used acrylic

glass tube for the suction side test section has an inner pipe diameter of $D_i = 0.19\text{ m}$. The overall averaged variation is $\pm 2.3 \times 10^{-4}\text{ m}$ corresponding to a deviation of less than 0.12%. The return line also made of acrylic glass has an inner diameter of $D_i = 0.342\text{ m}$, and an overall averaged variation of $\pm 3.2 \times 10^{-4}\text{ m}$. This is equivalent to a deviation of less than 0.1%.

The described diameter accuracies are in a satisfying range in agreement with reported mean velocity variations of 0.2% from MTL at KTH Stockholm or NDF at IIT Chicago.

4.1.4 Straightness and Alignment

Long test sections, in general, require high attention during the assembly process. This is even essential for the CoLaPipe. But there is another difficulty, in case of the CoLaPipe with its length of $L = 28\text{ m}$. It is the segmentation of the test section, i.e. 14 segments with a length of 2 m . Hence, the alignment of the pipe segments has to be done carefully to minimize deflections in the longitudinal direction with respect to the streamwise flow direction. For the realization we use common surveying devices, like a theodolite and a surveying level depicted in Figure 4.2a and Figure 4.2b.



(a) Theodolite to survey the pipe test section.



(b) Surveying level with tripod.

Figure 4.2: Surveying devices to align the pipe test section segments necessary to avoid deflections.

With the presented equipment it is possible to align the segments within an accuracy of $0.5\text{ mm}/100\text{ m}$. Before the alignment of the segments is conducted the sub-construction is set up and aligned, respectively. Here, an important boundary condition is the connection to the blower unit. This means that at first the sub-contraction and the blower unit has to be aligned. This is shown in Figure 4.3.



(a) Sub-construction of the CoLaPipe with a laser point at the end marking the position of the blower unit. The theodolite and the surveying level are used to set up the sub-construction as well as to establish the connection to the blower unit.



(b) CoLaPipe setup without pipe segments during surveying procedure with the blower unit at the end. The blower unit serves as connection and is therefore the initial point.

Figure 4.3: Overview about the alignment of the sub-construction with the blower unit. First step before the application of the pipe test section segments to avoid deflections in the streamwise direction.

Thereafter the pipe segments can be applied to the CoLaPipe sub-construction and aligned as well. The whole assembly of the parts is realized by the use of custom-designed flanges, which are prescribed in more detail in the following chapter.

4.1.5 Test Pipe Connections

A precise connection of the pipe segments is essential due to small perturbations between the intersection of two segments. Hence, we designed flanges of the same material as the pipe - acrylic glass - to obtain the same material properties, like weight and thermal expansion, depicted in Figure 4.4.

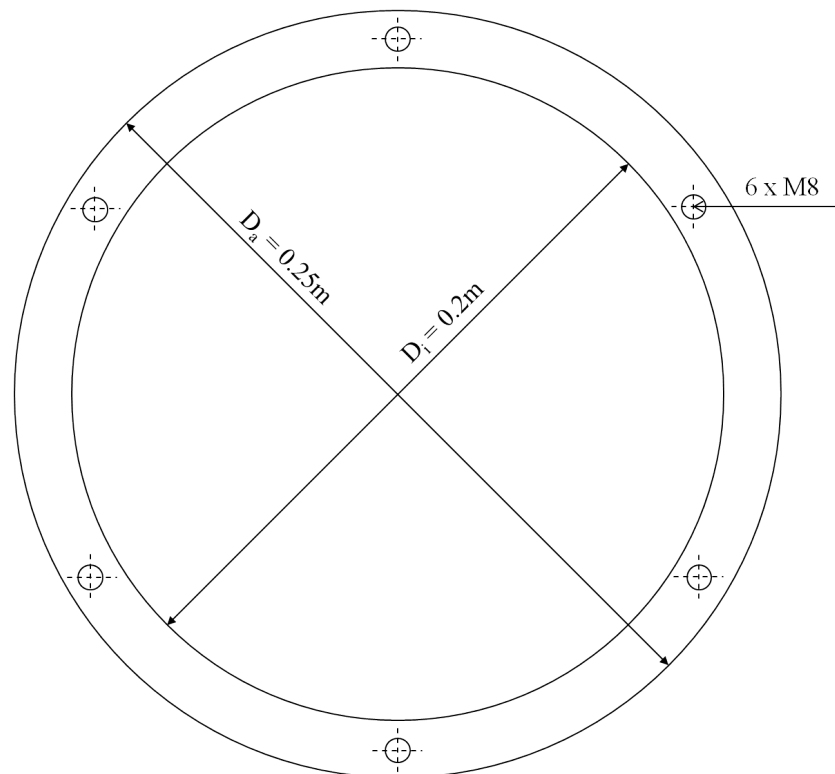


Figure 4.4: Schematic of flange.

The flanges itself have six drilling-holes on the pitch diameter to ensure a minimal power transmission. This design enables also an easy centering of the segments against each other. Additionally, we obtain small leakage effects. Nevertheless, the flanges are additional masked after the setup.

The fitting of the flanges to the pipe segments is conducted carefully through an adhesive bond, refer to Figure 4.5. One disadvantage of such a form-locked fixing is the aging. The adhesive bond has to be renewed after a certain time period to ensure a stable connection.

4.2 Settling Chamber

The settling chamber is an important part of any wind tunnel, eliminating flow disturbances before entering the test section and ensuring the uniformity of the inlet flow velocity profile with low turbulence intensity. The presented set-up, refer to Figure 4.6, is carefully designed following the recommendations made by Loehrke and Nagib [59] and Groth and Johansson [33], especially regarding the separation distances between the elements.

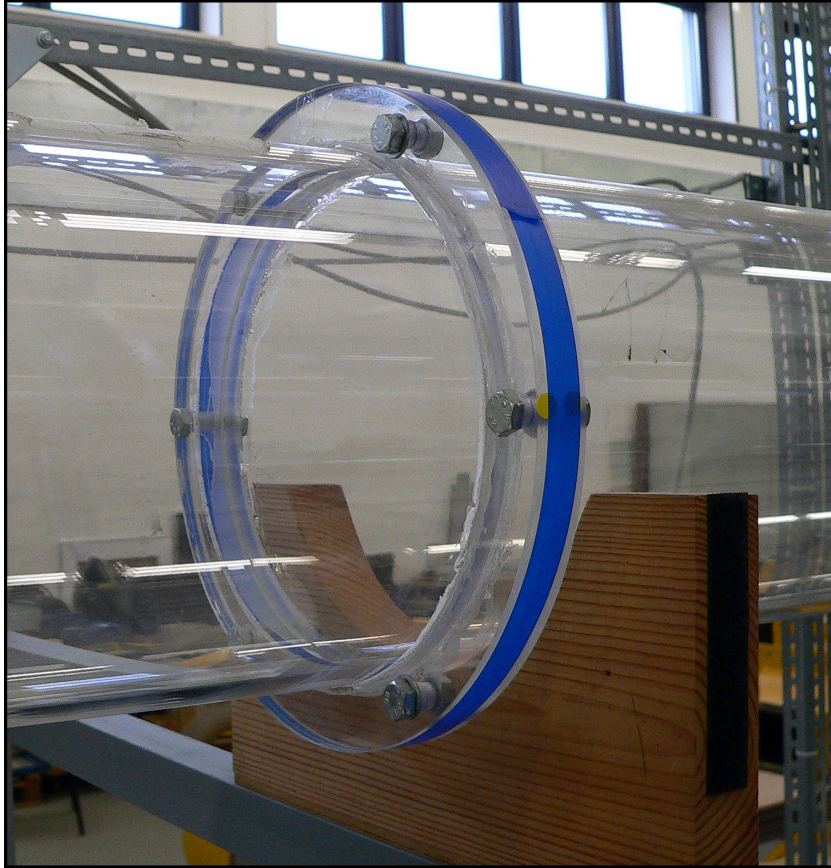


Figure 4.5: Connection of pipe test section through an adhesive bond.

Figure 4.6 depicts the common setup of the settling chamber containing passive flow control devices listed in detail in Table 4.1, where d represents the wire diameter and M the mesh diameter. The most downstream component is a perforated plate (1) with rectangular passages $10 \times 10 \text{ mm}^2$ in size reducing the inlet flow angle. The second flow controlling device is a honeycomb structured plate (2) with a mesh size of $d = 6 \text{ mm}$ and a total tube length of $l = 80 \text{ mm}$ providing a length-to-diameter ratio of $l/d = 12$. The honeycomb cells are aligned to flow direction to reduce and suppress fluctuating variations in transverse velocity with little effect on the streamwise velocity since the pressure drop through a honeycomb is small. Table 4.2 represents the pressure drop for various bulk-based Reynolds numbers and shows the slightly increasing pressure drop with increasing Re_m . It is expected that all pressure losses are mainly due to wall skin friction. In addition, to assure parallel flow conditions the honeycomb is mounted upstream of the main passive flow control device (screen assembly (3)).

This third essential flow controlling device consists of five screens having a solidity of 40%. A summary of the physical dimensions of the screens is given in Table 4.1. Every screen is fixed to a metallic frame to realize a simple assembly as well as disassembly.

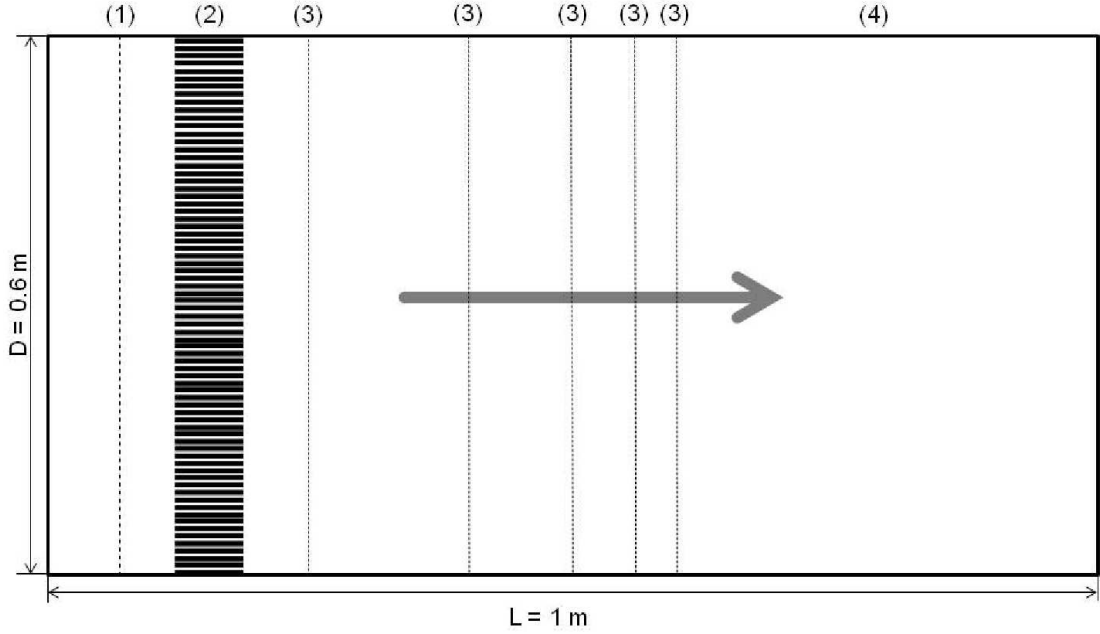


Figure 4.6: Sketch of the settling chamber with flow direction from left to right. (1) perforated plate, (2) honey comb, (3) screen assembly and (4) relaxation part.

Table 4.1: Physical dimensions of the settling chamber.

Device	$d[mm]$	$M[mm]$	Type	Distance from inlet [m]
1	10.00	10.00	perforated plate	0.135
2	6.00	-	honey comb	0.215
3.1	1.00	4.00	screen	0.250
3.2	0.71	2.50	screen	0.400
3.3	0.45	1.40	screen	0.500
3.4	0.16	0.70	screen	0.600
3.5	0.16	0.70	screen	0.700
4	-	-	relaxation part	1.200

The first screen is placed directly behind and in close proximity to the honeycomb to reduce level and structure of turbulence by modifying its shear layers and consequently its instabilities downstream of the honeycomb entire, refer to Loehrke and Nagib [59] for more details. According to Groth and Johansson [33] the minimum separation distance between two consecutive screens is 20 times the mesh size (refer to Table 4.1) that coincides with the region of rapid decay of turbulence intensity. The last part of the settling chamber is the relaxation part (4), between the screen assembly and the inlet contraction, providing a constant flow speed over the cross-section.

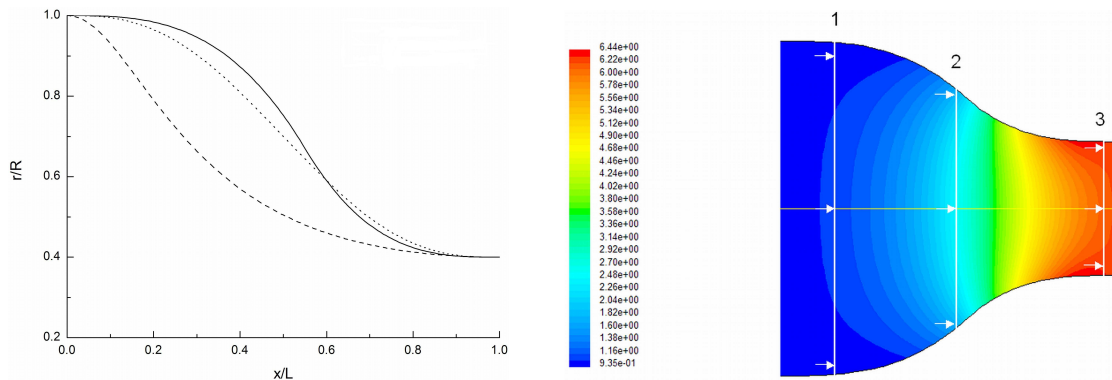
Table 4.2: Pressure drop through honey comb for different bulk-based Reynolds numbers (natural transition case).

$Re_m [\times 10^5]$	0.20	2.00	5.05	6.80	7.70
$\Delta p [Pa]$	5.16	7.31	13.83	19.86	21.93

4.2.1 Inlet Contraction

The contraction at the inlet of the pipe test section usually accelerates the flow coming from the settling chamber. Furthermore it reduces variations of the mean axial velocity in the plane of symmetry. The contraction ratio (CR) and its wall shape represents vital parameters in determining better performance of the contraction. For most of the lower speed wind tunnels a contraction ratio between 6 and 12 is recommended and a variety of wall contours can be found, e.g. in Bell and Mehta [12], Hussain and Ramjee [49], Morel [70] and Bradshaw and Pankhurst [15]. To summarize, the most relevant subjects for well-designed contractions are:

- uniform velocity at the contraction exit with low turbulence intensity level,
- small exit boundary layer thickness and flow free from separation.



(a) Dimensionless representation of three different contraction contours (L is the contraction length and R the inlet radius). — two-cubic arcs contour; \cdots 5th order polynomial contour; - - - Witoszynski (1924)

(b) Selected sample of the mean velocity magnitude for the two-cubic arcs contraction contour.

Figure 4.7: Numerical simulation supporting the design procedure for the contraction ($Re_m = 13650$).

A design procedure for the contraction wall proposed by Cohen and Ritchie [17] has been used applying potential-flow theory. Three different wall contours for contractions are simulated and depicted in Figure 4.7a. A typical result coming from numerical simulation is shown in Figure 4.7b. The present numerical simulations are carried out using the commercial code *Fluent* numerical CFD, incorporating a wide range of physical models for simulating numerous fluid flow problems. Flow characteristics along the axial and radial directions of the three contractions were evaluated.

A potential flow solver is utilized for predicting the internal flow, computing wall pressure, wall velocity distributions, and velocity distribution along the plane of symmetry and at the contraction exit as well. Figure 4.7a represents the wall contours for the three different contractions in normalized coordinates. It is worth noting that the geometrical parameters (C, L, D_i, D_o) for all contractions are similar, where L is the contraction length, D_i is the contraction inlet diameter and D_o is the contraction outlet diameter. A selected sample of the mean velocity magnitude is presented in Figure 4.7b for $Re_m = 13\,650$. It is observed that on the curved wall, near the contraction exit, the wall velocity is slightly higher than the velocity at the plane of symmetry. Boundary layer separation is also observed near the end of the two-cubic arc contraction, which might be attributed to the fact that the contraction length was not long enough. This was surprising since it is generally believed that the boundary layer is less subjected to separation at the exit due to the strong favorable pressure gradient. The sharp change in the concave curvature of the Witoszynski contraction (1924) at the inlet, refer to Figure 4.7a, destabilizes the flow through the contraction leading to flow separation and more higher velocity near the wall at the contraction exit when compared with the two cubic-arcs contraction, refer to Figure 4.7a.

The numerical simulations as well as the scientific experience lead us to the decision of choosing a 5th-order polynomial for the contraction wall contour, having a high area ratio of $CR = 9$.

4.2.2 Cooling System

The closed-loop design of the CoLaPipe, with its advantages and disadvantages, comes along with a specific requirement especially in the case of utilizing the HWA measurement technique. This technique operates based on stable working conditions, i.e. constant working temperature. The measurement system itself and even this temperature dependence as well as the application to the CoLaPipe is discussed in Chapter 5. Hence, the CoLaPipe is equipped with a well-designed cooling system purchased by *GWA - Gesellschaft für Wärme und Anlagentechnik mbH*. The installed cooling system consists

of a heat exchanger, a cooling pump, a piping system, pressure and temperature control devices, for the cooling circuit as well as for the refrigerant circuit, accessories, and a cooling unit. This cooling unit is located outside the laboratory to avoid influencing effects on the fluid flow properties, and to prevent annoyance of the operational safety. Figure 4.8 represents the cooling system showing most of the system parts. Excluded is the cooling unit.



Figure 4.8: Cooling system with heat exchanger (top), piping system (black pipes), pressure control system, valves and accessories.

The power requirement for the cooling system is dependent on the power assembly necessary to run the whole pipe setup. It provides an energy input of 45 kW to the flow, which has to be compensated by the cooling system. Therefore, the cooling unit works with a power of 45 kW , respectively.

Another requirement is a uniform temperature profile at the entry of the test section. This is realized through an installation of the heat exchanger right behind the corner, at the end of the facility. This gives the flow the opportunity to form a well distributed temperature profile.

Hence, the application of this described cooling unit enables a temperature adjustment in the range of 15°C to 21°C corresponding to a maximum deviation of $\Delta T = \pm 0.5\text{ K}$ at the actual measuring location.

4.3 Blower Unit

The first step on the way to apply a blower unit to a system is the consideration of all requirements and boundary conditions. In the case of the CoLaPipe the requirements and boundary conditions are the general design, which is closed-loop, the maximum achievable Reynolds number, the diameter of the test pipe, and the overall length of the test pipe. For a detailed description of the requirements refer to Chapter 1.2 and Chapter 2. The next step, after knowledge of all requirements, it is important to estimate the pressure losses of all additional parts to choose a blower, which is able to overcome it. Hence, a rough estimation of the pressure loss is presented in Table 4.3 for the test section as well as the return line. Both parts have the greatest proportion on the overall pressure loss and are therefor essential. Together, the actual test section as well as the return line produce a pressure loss of approximately 10 kPa, which is next to the nominal power of the blower an important property and has to be considered.

Table 4.3: Summary of calculated pressure losses for various pipe test facility devices with respect to a sufficient blower unit selection.

device	pressure loss [Pa]
CoLaPipe test section	8892.63
return line	357.9

The power assembly working with a nominal power of 45 kW contains a powerful radial blower connected to the pipe on its suction side, a three-phase motor, and a frequency converter. The three-phase motor works with a nominal rotation speed of 2940 Hz and the frequency converter within a control range of 1 – 50 Hz. The assembly provides a flow rate of 0.05 m³/s – 2.5 m³/s, which can be controlled by changing the frequency of the radial blower blades utilizing the frequency converter unit. With these properties and in conjunction with the inner diameter of 0.19 m of the lower test section the power assembly provides a maximum velocity of 80 m/s at the contraction exit. The turbulence intensity level at this position is less than 0.5%, see Chapter 6.1.1. In order to ensure a stable test facility, the radial blower is installed at the end of the lower pipe test section and is mechanically decoupled. Additionally, it delivers its output directly to the 340 mm diameter return line.



Figure 4.9: Centrifugal blower with motor and blower support equipped with damping elements. Coupling parts between blower and suction side, and blower and return line to avoid transmission of vibrations.

4.4 Final Setup of CoLaPipe

After designing, purchasing and mounting all parts we were able to finish the setup of the CoLaPipe test facility. The whole phase took a time of approximately four years. The following figures show the complete setup with all parts.

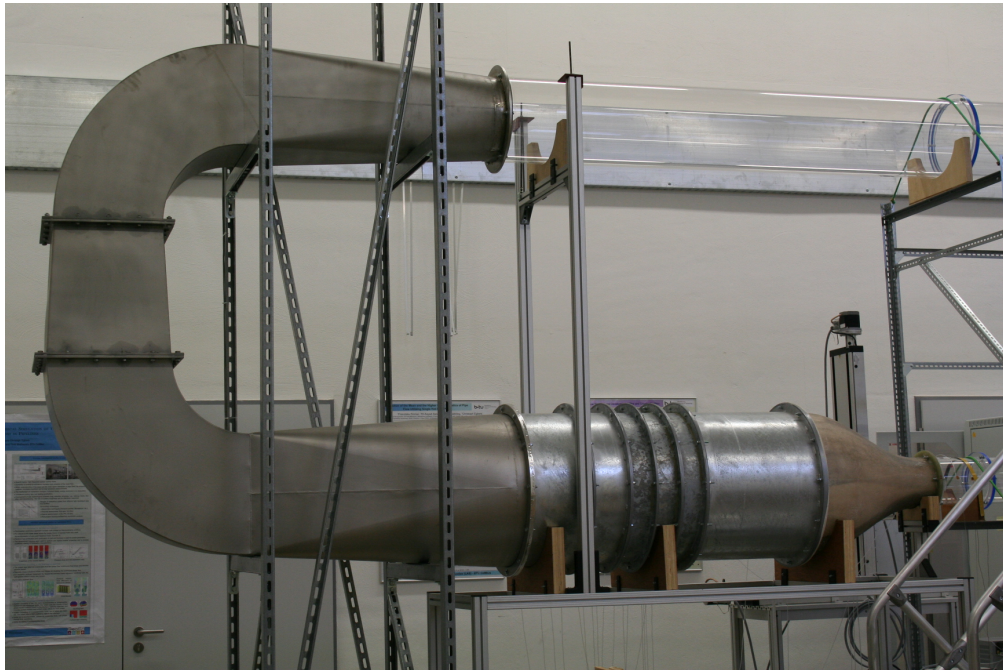


Figure 4.10: Corners with guide vanes, settling chamber and inlet contraction as well as a short piece of the actual test section (bottom) and the return line (above).

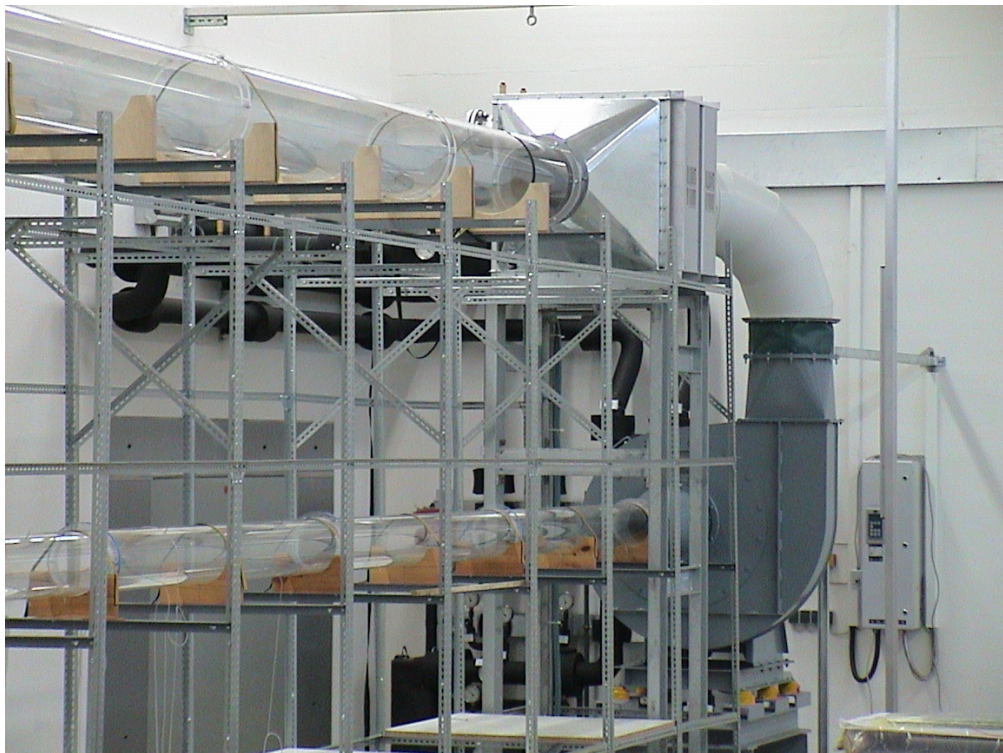


Figure 4.11: Blower and cooling unit with its connection to the return line and actual test section. In the background the mounting of the frequency converter.



Figure 4.12: Cooling unit with accessories and piping system.



Figure 4.13: Rear view of the test facility from the blower and cooling unit with the actual test section and the return line.

5 Measurement Techniques and Data Acquisition System

This chapter serves as a summary on the applied measurement techniques as well as the data acquisition system, with an additional discussion on advantages and arising limitations.

5.1 Pressure Measurements

The total pressure and its definition is described in Chapter 3. The particular components, i.e. static and dynamic pressure, can be measured separately by techniques that are presented in the coming sections. These measurement data are also used to evaluate specific components of the CoLaPipe, e.g. settling chamber, contraction unit or corners, with respect to pressure losses and velocity distributions. The pressure gradient along the pipe test section is investigated, respectively.

5.1.1 Measurement of Ambient Pressure

The ambient conditions comprise the ambient pressure p_{amb} and ambient temperature T_{amb} in the laboratory. Both are monitored and stored before, during and after each test run. For measurements of ambient pressure we use a *9032 - Mensor DPT6000 Barometer* working within a sensor range of 850 – 1150 *mbar*. The accuracy is very high with 0.02 % FS (full scale). This is important with respect to calculating fluid flow properties, like the density of the working fluid using the ideal gas law, and error analysis (Chapter 5.5). Refer to Chapter 5.2 for ambient temperature measurement.

5.1.2 Measurement of Static Pressure

These data sets are used to evaluate fluid flow attributes, like density and wall friction velocity, and provide information on the evolution of the flow field. Components of the

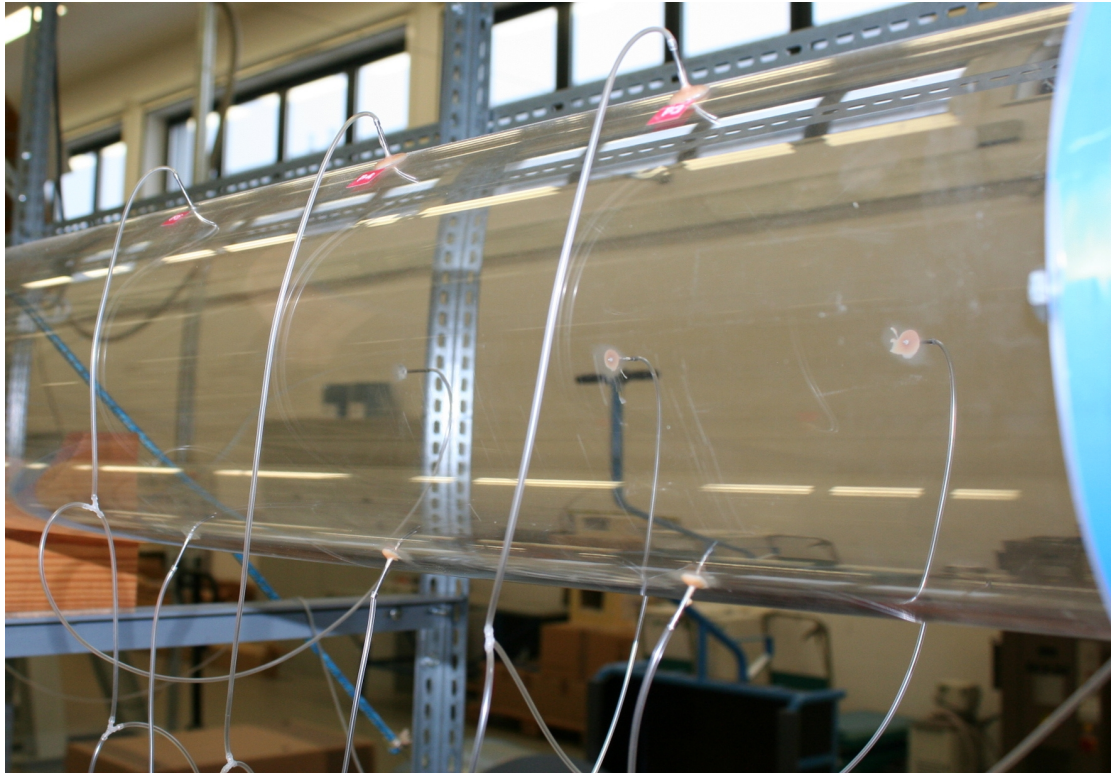


Figure 5.1: Photograph of the pipe test section provided with pressure tapplings for measurement of static pressure along the pipe.

test facility can be characterized, additionally. For realization the CoLaPipe is equipped with static pressure holes having an inner diameter of $D_i = 0.5 \mu\text{m}$ along the test section depicted in Figure 5.1, and along various components shown in Figure 5.2 and Figure 5.3. The tapplings are installed with great care to avoid influences on the flow system and to minimize measurement errors [64]. Small flexible tubes are connected to the tapplings, which are in turn connected to a pressure scanner. This pressure scanner is a *PSI Ethernet Pressure Scanner 9116* with a system accuracy of about 0.05% from full scale (FS). Two sensors are in use, wherewith thirty-two measuring points can be sampled simultaneously. One sensor has a pressure range of 69 *mbar* and the other of 170 *mbar*.

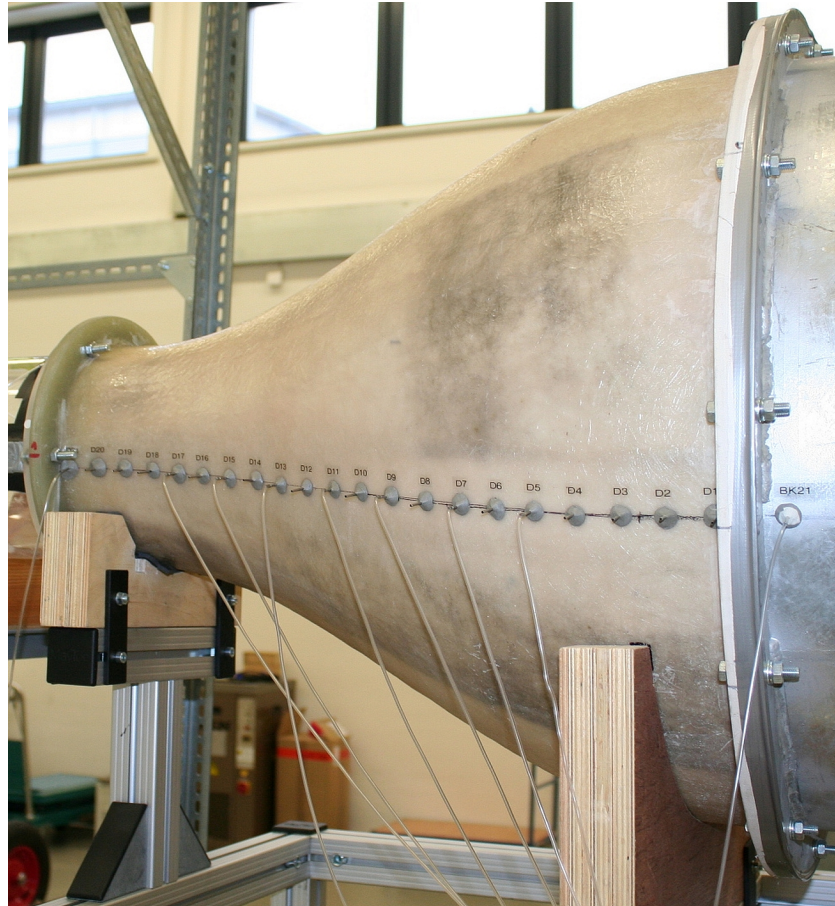


Figure 5.2: The contraction unit provided with pressure tapplings for quantitative characterization.

Pipe Test Section

To measure the static pressure at one cross section or to obtain the pressure gradient along the test section the whole pipe is equipped with static pressure holes. At each measuring station three pressure tapplings are installed around the circumference as depicted in Figure 5.1. The distance between each measuring station can vary between 0.25 m and 1.0 m depending on the required mass of information, i.e. close distances at the entry of the pipe test section as well as the measurement point for velocity measurements and wider distances in between.

Some selected results for different Reynolds numbers are presented in Chapter 6.1.2.

A detailed description of this direct pressure measurement can be found in Zagorola [108] with a conclusion on occurring advantages and even disadvantages. Also McKeon and Smits [64] were concerned with this apparently simple measurement

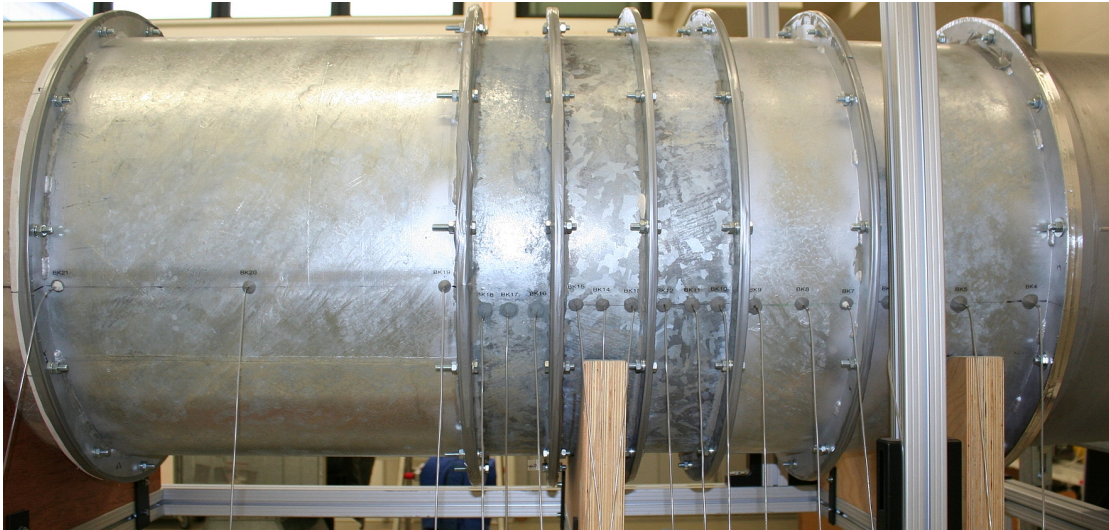


Figure 5.3: The settling chamber also provided with pressure tapings to obtain pressure losses through various parts, e.g. screens and relaxation part.

technique, but it turns out during data acquisition and post-processing of the data that some difficulties come into sight, which are further discussed in Chapter 6.

Facility Components

Information on pressure losses of various facility components are very important with respect to an overall characterization of the test setup, and to check or verify its significant influences on flow conditions. The following parts of the CoLaPipe are equipped with static pressure tapings, which are connected to *PSI Ethernet Pressure Scanner 9116* as well:

- inlet contraction,
- settling chamber with screens and relaxation part.

Figure 5.2 depicts the installation of static pressure measurement points along the inlet contraction contour. The settling chamber is shown as well in Figure 5.3.

5.2 Temperature Measurement

Measuring temperature is easy but important as well to estimate the working fluid density, and to provide and control stable boundary conditions, respectively. Therefore the working temperature inside the tunnel is measured by a thermocouple type T with a temperature range from -40°C to 133°C . The achievable tolerance is $\pm 1^{\circ}\text{C}$. The ambient temperature is recorded by a standard thermometer system with the same tolerance range as the thermocouple.

5.3 Velocity Measurements

Solving pipe flow turbulence comes along with resolving the velocity field. Therefore, different high-quality measurement techniques such as; optical based systems, i.e. PIV or LDA, or thermal anemometry system are available at LAS. A common thermal anemometry method to obtain information on time-averaged mean and fluctuating velocities, and on turbulence quantities, like Reynolds stresses, is the constant-temperature anemometry. It is the preferred measurement system applied to the CoLaPipe, and described in detail in the following. Another technique, namely constant-current anemometry (CCA), can be applied to resolve the flow field, respectively, but this method is not in focus here. For more information regarding CCA see Tropea et al. [97].

5.3.1 Basic Principal

The basic principal of hot-wire anemometry (HWA) is the convective heat transfer from a heated wire with respect to the surrounding fluid. Heating the wire, up to a temperature considerably higher than the fluid temperature, reflects the fluid flow velocity due to the required electrical heating voltage. This procedure is realized through a bridge circuit. A schematic setup of a single wire HWA sensor system is depicted in Figure 5.4. The probe, regardless of single- or multi-wire type, consists of a metallic wire fixed between two slender holders called prongs. In general, the wire material is Platinum coated Tungsten or Platinum Iridium alloy.

All measurements carried out in the CoLaPipe are conducted with single-wire probes provided with different diameter and lengths. Table 5.1 lists the physical dimensions of the applied probes, where l^* is important regarding spatial averaging effects [50].

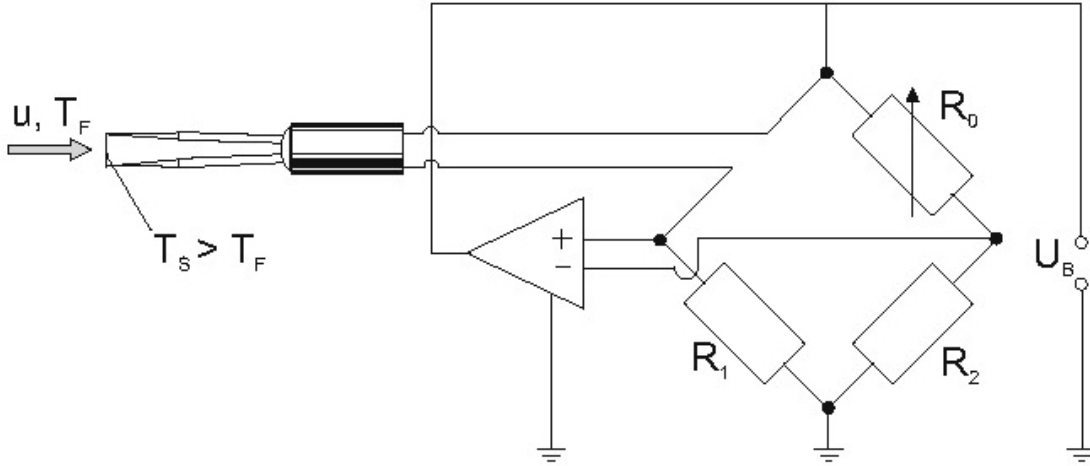


Figure 5.4: Scheme of constant temperature anemometer with bridge circuit [77].

Table 5.1: Overview about HWA probe collection, where D_w is the wire diameter, l_w is the wire length, L/D is the length-to-diameter ratio, and l^+ is the viscous-scaled wire length.

probe type	probe model	D_w [μm]	l_w [μm]	L/D	l^+
single-wire	55P11 (Dantec)	5.0	1250	250	$85 \leq l^+ \leq 247$
single-wire	55P15 (Dantec)	5.0	1250	250	$85 \leq l^+ \leq 247$
single-wire	1210-T1.5 (TSI)	3.8	1270	334	$84 \leq l^+ \leq 251$
single-wire	1218-T1.5 (TSI)	3.8	1270	334	$84 \leq l^+ \leq 251$
single-wire	1218HT-PI2.5 (TSI)	6.3	1270	202	$84 \leq l^+ \leq 251$

5.3.2 Hot-Wire Calibration

Before conducting each set of measurements it is essential to calibrate the probes against a reference velocity to determine the relationship between the anemometer output voltage and the corresponding physical property - in our case the fluid flow velocity [16]. To achieve an accurate calibration we use an ex-situ calibration procedure depicted in Figure 5.5 providing a well-known uniform velocity profile. Using the control unit of the CTA, we are able to adjust the reference velocities in the desired range within an accuracy of 0.15%, and to determine the calibration curve and the related calibration coefficients. A fourth-order polynomial fit is the basis for estimating the reference velocity approaching an accuracy of $\leq 1\%$. One selected calibration curve is presented in Figure 5.6 showing the measured bridge voltage against the reference velocity. The error for the recalculated velocity at every measuring point is shown, respectively.



(a) Ex-situ calibration unit with air supply. (b) Variable angle adjustment. (c) Calibration unit contraction with probe to be calibrated.

Figure 5.5: Details of the ex-situ calibration unit.

In addition, the air temperature inside the calibration unit is always measured by a thermocouple type T within an accuracy range of $\pm 1.0^{\circ}\text{C}$ to correct any temperature drift instantaneously allowing a point by point correction.

5.3.3 Application at CoLaPipe

The option of applying the constant-temperature HWA at the CoLaPipe is easy due to its great acceptance in the fluid mechanics community despite its limitations [50, 56, 58, 115]. But the application at the experiments is more difficult due to its sensitivity and lean mechanical resistance. To prevent a decrease in the lifetime of HWA probes the pipe test section is well prepared to guaranty an access without difficulty. A three-dimensional traverse system gives the possibility to move measuring probes independently in the streamwise, spanwise and vertical direction, depicted in Figure 5.7. The movements are controlled through three two-phase stepper motors mounted on top of each rail guiding system. The whole traverse system is set up on a special aluminum I-beam working table independently of the pipe test facility to avoid influences like vibrations. To reduce further vibrations and to balance imperfections, the traverse is additionally elastically based. Every data set is sampled with a sampling frequency of 10 kHz over a time period of 26.2 sec .

With the great care of the experimentalist and the supporting systems the HWA probe

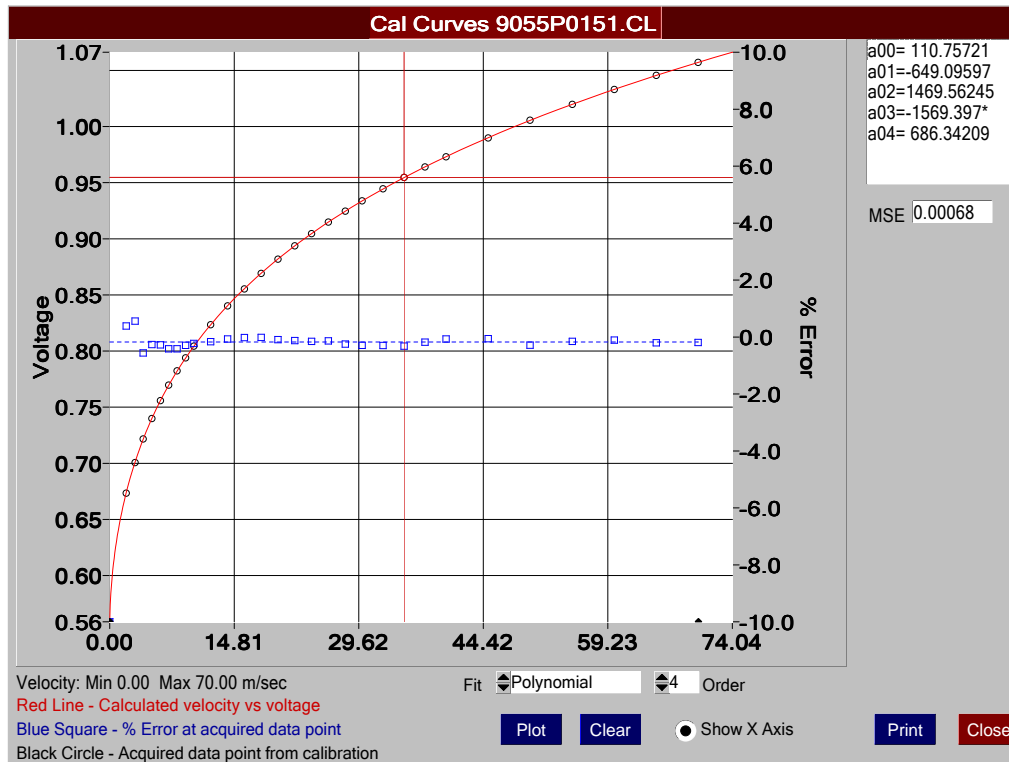


Figure 5.6: Selected example for a HWA calibration depending on a fourth-order polynomial. The data set is fitted using *ThermalPro* - the official software for the TSI IFA300 CTA.

and the probe support can be placed comparatively accurate within the test section. This is depicted schematically in Figure 5.8, where also the wire orientation with respect to the flow direction is presented.

5.4 Data Acquisition

All the measuring equipment is connected to an A/D converter board with a 16-bit resolution. In addition, a computer-based programming system is used for acquiring and processing all measurement data. The huge amount of incoming measurement data is treated with caution due to storage capacity and possible misapplication. Hence, only the direct incorporated experimentalist have an access to these data. And the data sets are stored on two independent systems to avoid data loss.

The post-processing of the data is executed with a commercial software for data analysis and graphing - *OriginPro*.



Figure 5.7: Traverse mechanism with independently moving components.

5.5 Quantification of Measurement Uncertainties

A not negligible fact is the uncertainty of measurements due to inaccuracies of applied measurement systems, e.g. temperature and pressure measurements. These measurement errors influence the post-processing of the sampled data, and have to be kept in mind. Table 5.2 represents uncertainties of used systems, which are in the following processed within an error propagation.

The presented list shows the sources of error, where mainly the temperature measurement influences the error propagation. This is in turn a possibility to reduce errors by changing the thermocouple towards a better accuracy or smaller temperature range. It

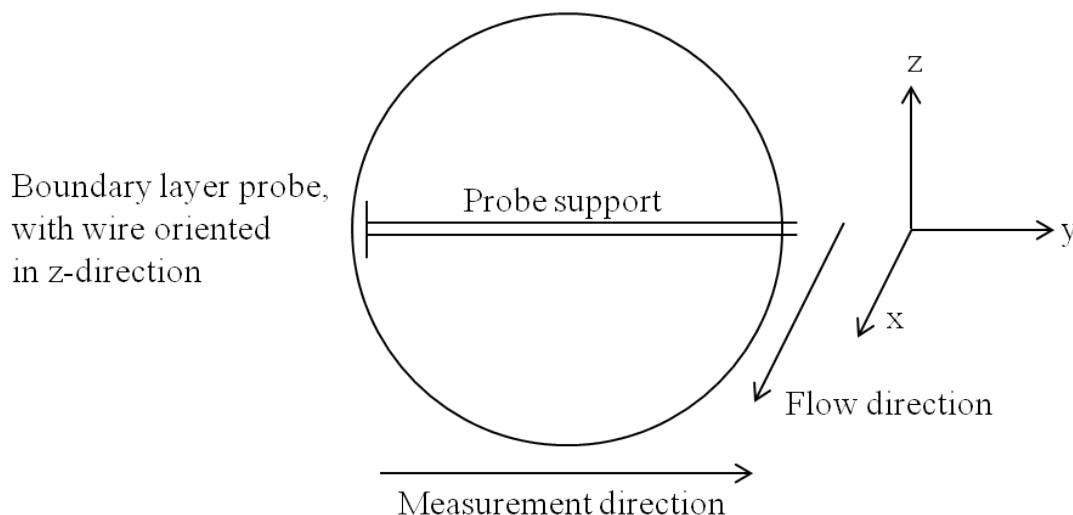


Figure 5.8: Schematic wire orientation in the CoLaPipe test section.

would also reduce the HWA calibration uncertainty (see Table 5.3) with respect to the temperature correction. For measurements of static pressure it is difficult to define an absolute error due to influences of shape and diameter of the holes [64]. As a practical guide it is suggested by McKeon and Smits [64] to have (1) a large and constant l/d , at least $l/d \geq 2$, where l is the tapping depth and d is the pressure tapping diameter, and (2) a small d/D ratio, where D is the pipe diameter. In the case of the CoLaPipe arise a ratio of $d/D = 0.00263$ and $l/d = 6$, wherewith it is supposed that the static pressure error is very small.

The next step is an error propagation to get information about the uncertainties of estimated values, like working fluid density or wall friction velocity. The uncertainties are calculated following the proposed method by Holman [42]. The results are presented in Table 5.3.

The error propagation shows significant influences of measurement uncertainties on estimated fluid flow properties. Despite this the error values are always less than 1.5% providing a good basis to support a deeper knowledge of pipe flow turbulence.

5.6 Determination of Fluid Flow Properties

The determination of the fluid flow properties, i.e. density and kinematic viscosity, is one of the most constitutional objects in fluid dynamics. This results out of the basic *Navier-Stokes-Equations*, refer to Chapter 3. Another important fact regarding the determination is the utilization of ρ and ν for the purpose of data normalization using

Table 5.2: Uncertainty estimation for different measurement parts with respect to manufacturer's instructions.

Source	Uncertainty (\pm)	Remarks
Temperature		Sec. 5.2
ambient	0.75 %	
working	0.75 %	
Pressure		Sec. 5.1
ambient	0.02 %	
static	≤ 0.5 %	
Pipe radius or diameter	0.12 %	Sec. 4.1.3
Pipe test section length	0.10 %	
Traversing system	0.02 mm	repeat accuracy Sec. 5.3
Blower	0.2 %	Sec. 4.3

Table 5.3: Error propagation for important estimated fluid flow properties based on the rms-method. The uncertainties for the HWA calibration as well as the cooling unit are represented, respectively, to quantitatively characterize the experiment.

Source	Uncertainty (\pm)
Working fluid density (perfect gas law)	0.37 %
Kinematic viscosity (Sutherland's correlation)	0.50 %
Pressure gradient	0.51 %
Wall friction	0.90 %
Wall friction velocity	0.50 %
Viscous length scale	1.54 %
Time-averaged fluid flow velocity	1.26 %
Normalized velocity (u^+)	1.50 %
Reynolds number	0.93 %
Kármán number	0.75 %
HWA calibration error	1.25 %
Cooling unit	0.75 %

u_τ . Hence, both values have to be calculated in the most accurate way since the product of ρ and ν form the dynamic viscosity μ

$$\mu = \nu \rho, \quad (5.1)$$

and

$$\tau_w = \mu \frac{\partial U}{\partial y} \quad (5.2)$$

$$u_\tau = \sqrt{\frac{\tau_w}{\rho}}. \quad (5.3)$$

A detailed description for the derivation of τ_w in Equation 5.2 is discussed in Chapter 6.4.2.

In the following the process of calculating ρ and ν is substantially presented.

Calculation of Fluid Density

Calculating the density ρ of the working fluid is rather simple due to the simpleness of the perfect gas law, refer to Equation 5.4, with the assumptions of incompressibility, stationarity and inviscid conditions,

$$\rho = \frac{p}{R_{gas} T}. \quad (5.4)$$

Due to the closed setup of the CoLaPipe the pressure p in Equation 5.4 is defined as the sum of the static pressure inside the test section and the ambient pressure, which prevails in the laboratory. Hence, Equation 5.4 can be rearranged as follows:

$$\rho = \frac{p_{amb} + p_{stat}}{R_{gas} T}. \quad (5.5)$$

Despite the simpleness of the perfect gas law great attention has to be payed to the estimation of T , p_{amb} and p_{stat} , i.e. these values can be measured directly but have to be with high accuracy due to measurement uncertainty analysis. These facts are discussed in Chapter 5.5.

The calculation of the fluid flow density is an automated part in the analyzing procedure

for the experimental data. The resultant values are within a range of $1.16 \text{ kg/m}^3 \leq \rho \leq 1.25 \text{ kg/m}^3$ depending on the working temperature T and the directly measured pressure.

Calculation of Kinematic Viscosity

Due to the quasi-independence of the kinematic viscosity ν of air with respect to the pressure, the calculation of ν is insensitive in comparison to the calculation of ρ . Hence, the well-known *Sutherland's correlation* [3]¹ is depending on only one dimension: the working temperature T .

$$\nu = 1.458 \times 10^6 \frac{T^{3/2}}{\rho(T + 110.4)} \quad (5.6)$$

Nevertheless, it is important to minimize measurement errors, since they increase the uncertainty of, e.g. the wall friction velocity, respectively. It is also obvious, that ν is slightly changing with changing temperature. Therefore, the calculation of ν is an automated part of the post-processing of the experimental data as well. The range of the kinematic viscosity of air is $1.52 \times 10^{-5} \text{ Pa/sec} \leq \nu \leq 1.56 \times 10^{-5} \text{ Pa/sec}$.

5.7 Accurate Positioning of HWA Probes

A precise wall distance determination is of great importance in the field of turbulence measurements especially at high Reynolds numbers where the thickness of the viscous sublayer diminishes. Accordingly, different methods exist, particularly, for hot-wire measurements like the calibration positioning procedure proposed by Bhatia et al. [13] and [23], or the optical method by Janke [51]. Another new method is published by Alfredsson et al. [1] exploit the self-similarity of the distribution functions of the stream-wise velocity fluctuations within the viscous sublayer. There are much more methods concluded in detail by Örlü et al. [88] showing that classical as well as new developed methods to estimate the absolute wall distance and also the wall friction velocity u_τ exist. Maybe a combination of various methods is a good decision to achieve results with the required accuracy, but this discussion is not in focus here.

Within these investigations the optical method is used, which is described in the following.

¹[3]; refer to p. 19 for description of *Sutherland's correlation*

5.7.1 Application of Optical Method to CoLaPipe

As already described in Chapter 4.1 the optical accessibility to the test section is given through the used pipe material - acrylic glass. Hence, it is relatively simple to position a probe and its support, like a single-wire HWA probe as in this case, as close as possible to the wall. It is realized by driving the traversing system together with the probe assembly step-by-step until the maximum point, which can be monitored with no other helping device except the eyes. But it is obvious that this can only be a first approach, because of different influence, like the human eye itself and the wall curvature, which generates a deformed view. To overcome this problem the optical method presented by Janke [51] is applied. This method uses the mirror effect. The effect deals with the distance between the original and the image, where the observed distance is half of the absolute distance. For the CoLaPipe application it means, that this specific distance has to be monitored and controlled. This is realized by taking pictures to measure the distance. Figure 5.9 shows as representative a picture with the mirror effect. An important fact, which as to

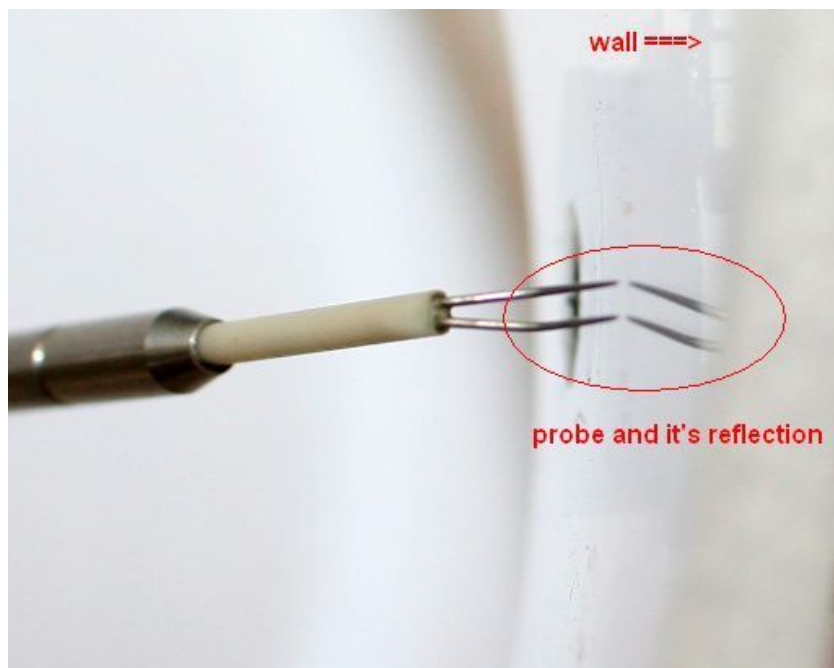


Figure 5.9: Schematic of the mirror effect showing a single-wire HWA probe with probe support and the mirrored image. The wall normal distance is non zero.

be considered, is the scale in the picture with respect to the absolute distance. For the application and the accurate positioning of the probes it means that the closest position to the wall is, where the distance between the original and the image is zero. And here another fact has to be considered. This is the deflection of the probe and the probe support under flowing conditions due to the force coming from the high velocity.

This deflection changes the wall distance significantly in comparison to no or low flow conditions. If this circumstance is not well considered the probe can be broken due to its sensitivity.

6 Results

6.1 Boundary Conditions

Prior to the classification of the obtained pipe flow results it would be essential to discuss different boundary conditions under which all investigations are conducted. Hence, through the following sections the applied boundary conditions are discussed, which cover the inlet flow conditions, the ruling pressure distribution and the fact that either natural or artificial transition is investigated.

6.1.1 Inlet Flow Conditions

The design requirements for the CoLaPipe claim for high-quality results in all fields of interest, especially in turbulence. This implies fully developed turbulent pipe flow and consequently a developed velocity profile. To approach the mentioned aims well defined inlet flow conditions, i.e. a uniform velocity profile with low turbulence intensity level at the exit of the contraction, have to be provided. This is achieved by combination of two well designed parts:

1. settling chamber and
2. inlet flow contraction,

which are described in detail in Chapter 4. The effect on the flow is depicted in Figure 6.1, where the slightly increasing turbulence intensity ($\sqrt{u'^2}/\bar{U}_c$) is shown as a function of the bulk-based Reynolds number Re_m ¹. Nevertheless the turbulence intensity is always less than 0.45 %, which is commonly a good result. To confirm the high-quality conditions Figure 6.2 shows uniform mean velocity profiles for some selected bulk-based Reynolds numbers. Here, the normalized wall normal distance $y(R)/R$ is depicted as a function of the time-averaged mean velocity \bar{U} . In this case, $y(R)/R = 1.0$ represents the pipe

¹Note that in some publications the notation for the bulk-based Reynolds number is Re_b .

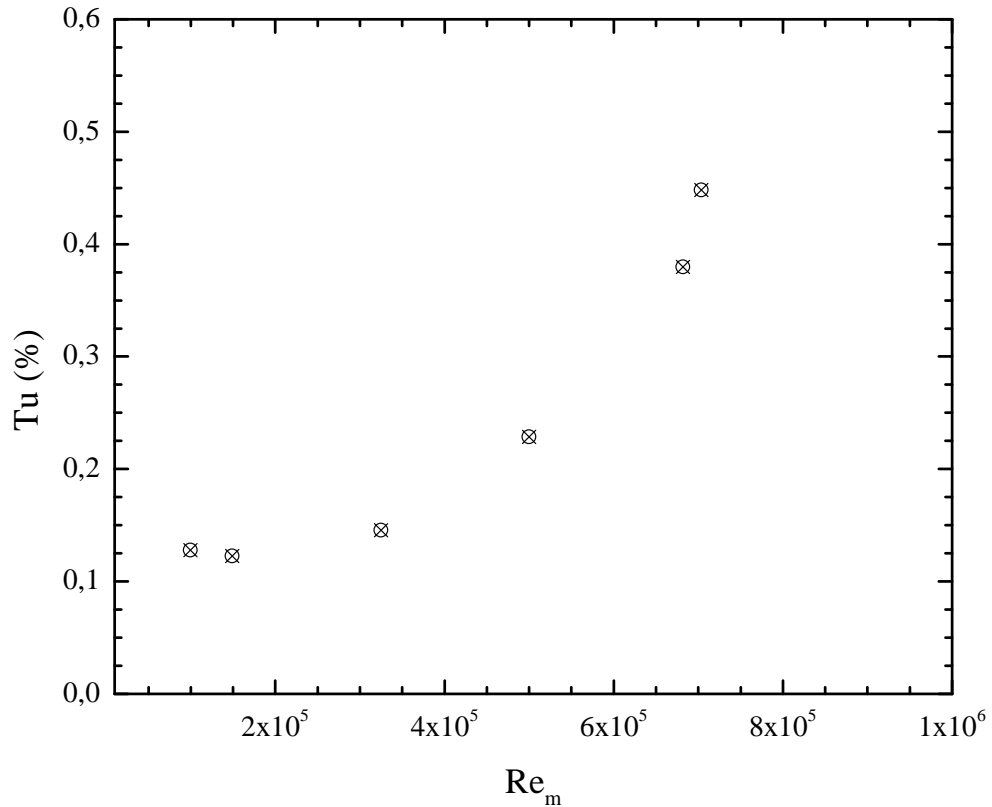


Figure 6.1: Turbulence intensity level ($\sqrt{u'^2}/\bar{U}_c$) versus bulk-based Reynolds number (Re_m) at the contraction exit without triggering the flow.

wall, where $y(R)/R = 0.0$ corresponds to the center part of the test section. Hence, the presented velocity profiles are plotted for half of the pipe diameter. This representation of mean velocity profiles is also common due to the symmetry effect in pipes with respect to the circular cross section.

As it can be observed in Figure 6.2 there is no variation in \bar{U} for the lower Reynolds numbers cases, which is a result due to the careful design of the settling chamber and inlet contraction. For higher Reynolds numbers ($Re \geq 6.8 \times 10^5$) a slight variation of the mean velocity profiles is obtained. It is believed, that this deviation is due to the stronger interaction between the fluid flow load and the measurement technique hardware, i.e. the HWA probe support. Note that the no-slip boundary conditions show its validity, certainly, thus zero fluid flow velocity at the wall is measured. It even results in the large velocity gradient (dU/dy). Therewith the great influence of the viscous force in the vicinity of the wall is shown. Thus, the CoLaPipe provides uniform velocity profiles at the entrance region of the pipe test section.

Concluding from the mentioned points, the presented inlet flow conditions of the introduced CoLaPipe are in good agreement with the literature. This is the basis for our recent pipe flow investigations within a high Reynolds number range and gives us the possibility to compare the results with the literature.

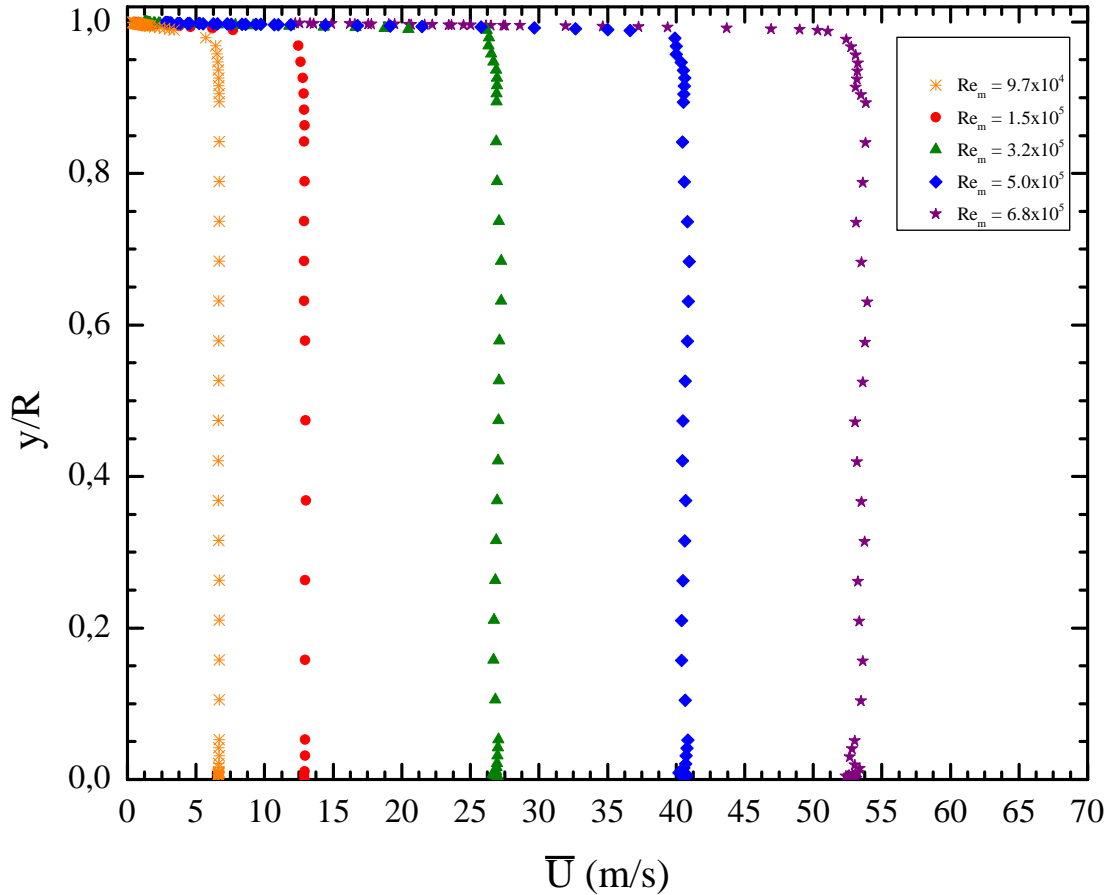


Figure 6.2: Uniform velocity profiles for selected bulk-based Reynolds numbers (Re_m) without triggering the flow.

6.1.2 Pressure Distribution

One decision during the design phase of the CoLaPipe is the utilization of the pressure force to drive the flow. This fact plays an important role regarding the estimation of the wall shear stress τ_w and to evaluate some parts of the pipe, which can be critical; e.g. due to high pressure losses. Thus, the following part deals with the interaction of the pressure force and the pipe test section.

Pipe Test Section

As mentioned before the flow concept of the CoLaPipe is the utilization of the pressure force to drive the flow. Hence, to characterize the flow conditions for varying Reynolds numbers it is obvious that detailed information regarding the pressure distribution along the pipe test section are essential. These can be obtained from careful and precise pressure gradient measurements. These results are also very important with respect to the estimation of τ_w (refer to Chapter 6.4). To give an insight into this, the theoretical background is described in Chapter 3 and the technical realization is presented in detail in Chapter 5.1. Thus, a representative pressure distribution for one Reynolds number ($Re_m = 6.3 \times 10^5$) is discussed and depicted in Figure 6.3 to illustrate the experimental approach and realization at the CoLaPipe.

In Figure 6.3 the static pressure, measured via static pressure holes, is shown as a function of the pipe test section length. Here, $x = 0$ m marks the pipe inlet. The two measurement points before $x = 0$ m mark the reference points along the contraction. Note that they are not accounted estimating the pressure gradient for the pipe test section.

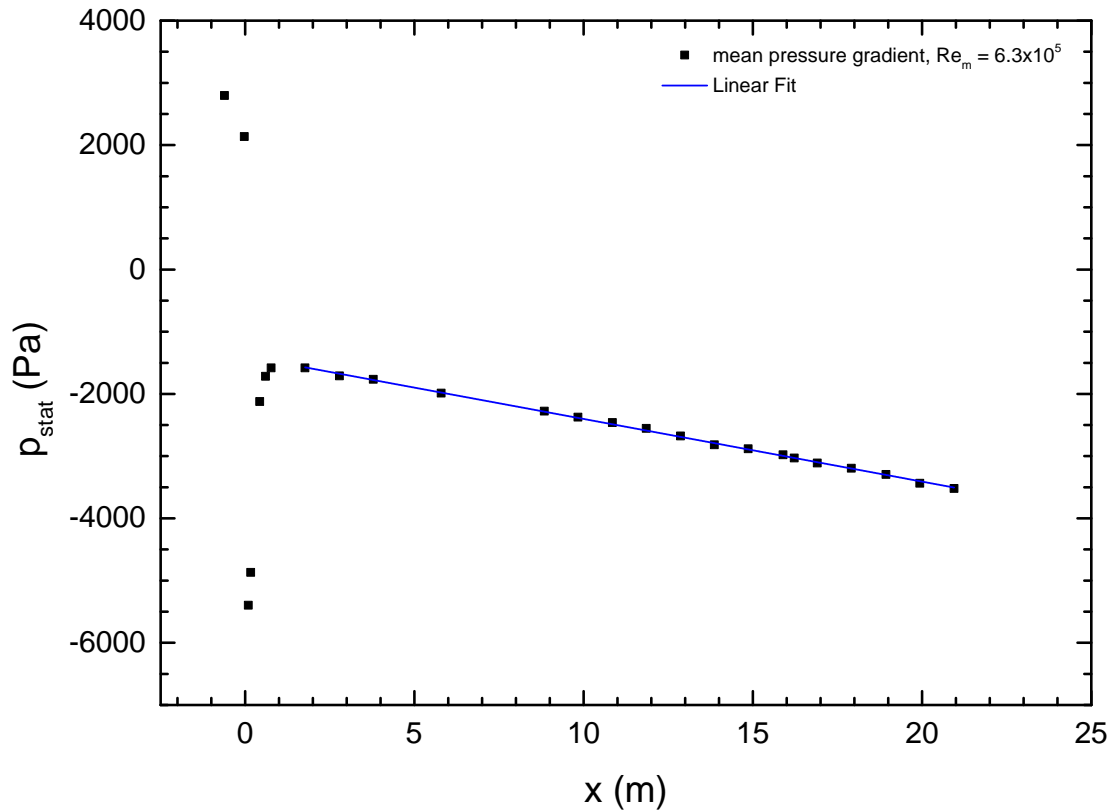


Figure 6.3: Pressure distribution along pipe axis.

A closer consideration of Figure 6.3 shows a sharp variation in the pressure distribution at the inlet of the pipe. This significant pressure loss is characteristic due to a sudden reduction in cross section. Within this thesis an orifice is used as tripping device. This circumstance is described in Chapter 6.1.3 and hence no further discussion on it is presented within this section. Following the pressure distribution after a relative short length of nearly $x = 2$ m, compared to the overall length of the test facility, the pressure variation disappears and the pressure distribution now follows a linear behavior. This is shown more precisely by the blue line representing a linear fit. Additionally, the pressure distribution shows a negative slope, which results also in a negative pressure gradient. This is due to the working mode of the blower, which is the suction side working mode. Hence, the working fluid is pulled through the pipe and the static pressure drop is negative.

After checking the linearity of the pressure distribution the pressure gradient dP/dx is estimated for every data set and boundary condition, respectively. As mentioned before, this step is very important with respect to the evaluation of the wall shear stress and hence the wall friction velocity. For the presented example, depicted in Figure 6.3, the pressure gradient is evaluated to be:

$$\frac{dP}{dx} = \frac{-3500 \text{ Pa} - (-1600 \text{ Pa})}{21 \text{ m} - 1,5 \text{ m}} = \underline{\underline{-97.44 \text{ Pa/m}}}$$

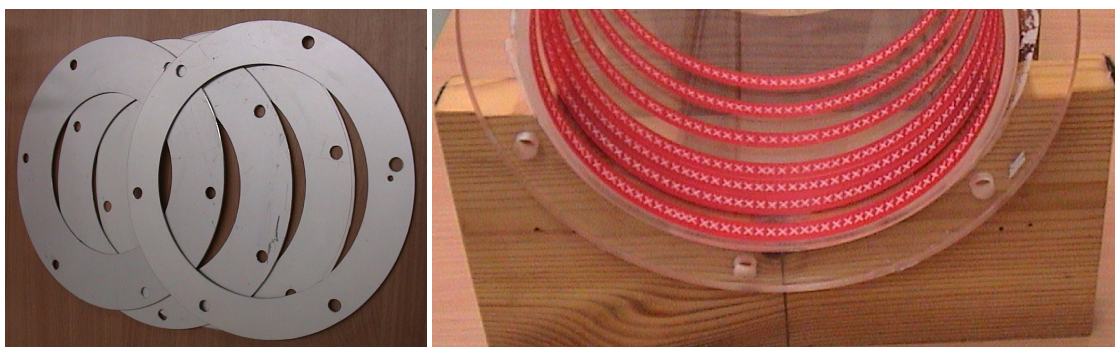
Further on, the estimated pressure gradients are applied to Equation 3.21, relation to calculate the wall shear stress, wherewith the wall friction velocity u_τ (Equation 3.22) is then estimated. This is the general procedure with the final aim of scaling the mean velocity profile. But this simple method shows beside useful advantages some disadvantages, which is discussed in detail in Chapter 6.6.

6.1.3 Transition Scenario

Investigating pipe flow turbulence is usually possible for two transition scenarios. One is called natural transition, where the flow is not externally disturbed, and therefor has the possibility to develop from scratch. The other is called artificial transition, where the test facility is modified to manipulate the flow and to trigger turbulence. This means the approach to the turbulent flow state is forced by defined disturbances at the inlet part of the pipe test facility. Both methods are common and therefor well known. Due to the fact, that scientists use these methods or scenarios, a variety of tripping methods are available. In the case of air as the working fluid cylindrical wires, sand papers, partial inlet blockage, i.e. orifices, organized tape letters, turbulence grids and other methods

are utilized. If water is the suitable working fluid, as in many cases for investigations on low Reynolds numbers, different methods are employed, like fluid injection [82] or simultaneous injection and withdrawal [41].

The presented study contains results on both transition scenarios, either natural and artificial transition, described in Chapter 6.2 and Chapter 6.3, respectively. For the artificial transition case, orifices are utilized, and an example is depicted in Figure 6.4a. These orifices block the entrance cross-section of the pipe by a certain percentage. Usually, the orifice is mounted at the inlet of the test section, i.e. at $x = 0$, to trigger the flow over the circumference of the pipe. The blockage area in percentage can be varied between 5% to 40% by changing the orifice height according to investigations by Fischer [30]. Due to the conclusion of Fischer [30], who has claimed a critical blockage ratio of about 20% beyond the flow is not further influenced, it was decided to limit the investigations to a maximum blockage of 23% cross section in this study. Hence, if further investigations are necessary, e.g. due to resultant inconsistencies, the cross section blockage can be increased with no additional effort since the orifices are at hand. Another technique, which is often used for triggering the flow, especially in TBL investigations, is gluing of sand paper stripes on the inner surface of the entrance region in a pipe or even flat plate as well as utilizing organized tape letters, see Figure 6.4b. With this variety of tripping devices the influence on the development of the mean and fluctuating flow properties over a wide range of Reynolds numbers can be investigated. In addition, similarities and differences between natural, i.e. transition without certain disturbances, and artificial transition in pipe flow can be reviewed and possible effects detected. Note that such a detailed series of experiments is not the focus of the present study, and hence such results and the related discussion might extend the present technical work.



(a) Orifices with different blockage ratios.

(b) Arrangement of organized tape letters.

Figure 6.4: Different tripping devices for investigations of air as working medium.

6.2 Development Length - Natural Transition Case

As mentioned before a fundamental part of this thesis is the investigation of the natural transition scenario, i.e. no disturbances at the inlet of the pipe to trigger earlier transition. These measurements are conducted in an open pipe test facility. This setup was built as a pre-stage before finishing the CoLaPipe setup as a closed-loop facility, which has been already introduced in Chapter 4.4. The former configuration is depicted in Figure 6.5. At this point a detailed description of this setup is omitted due to the same basic considerations, which are described in detail in Chapter 4. Nevertheless, the basic parts are mentioned, which are mounted together and shown in Figure 6.5 starting at the point of incoming flow, i.e. from left to right:

- bell mouth
- settling chamber
- inlet contraction
- pipe test section
- diffuser
- blower unit
- circuit for the outgoing air
- air exit through laboratory wall

Due to the novelty of the CoLaPipe the first measurements at this test facility are to characterize the flow along the pipe test section. This means it is important for later experiments on pipe flow turbulence to know the flow states at different positions in the pipe. Hence, the first results show centerline measurements of the mean axial velocity with respect to the overall length. Those information are commonly known as development length, i.e. the length the flow needs to reach the fully turbulent flow state. Figure 6.6 shows these first results, where the statistical quantities Tu (turbulence intensity level), $S_c(\overline{u'^2})$ (skewness factor) and $F_c(\overline{u'^2})$ (flatness factor) are presented as a function of the normalized streamwise distance. The mathematical relations for all

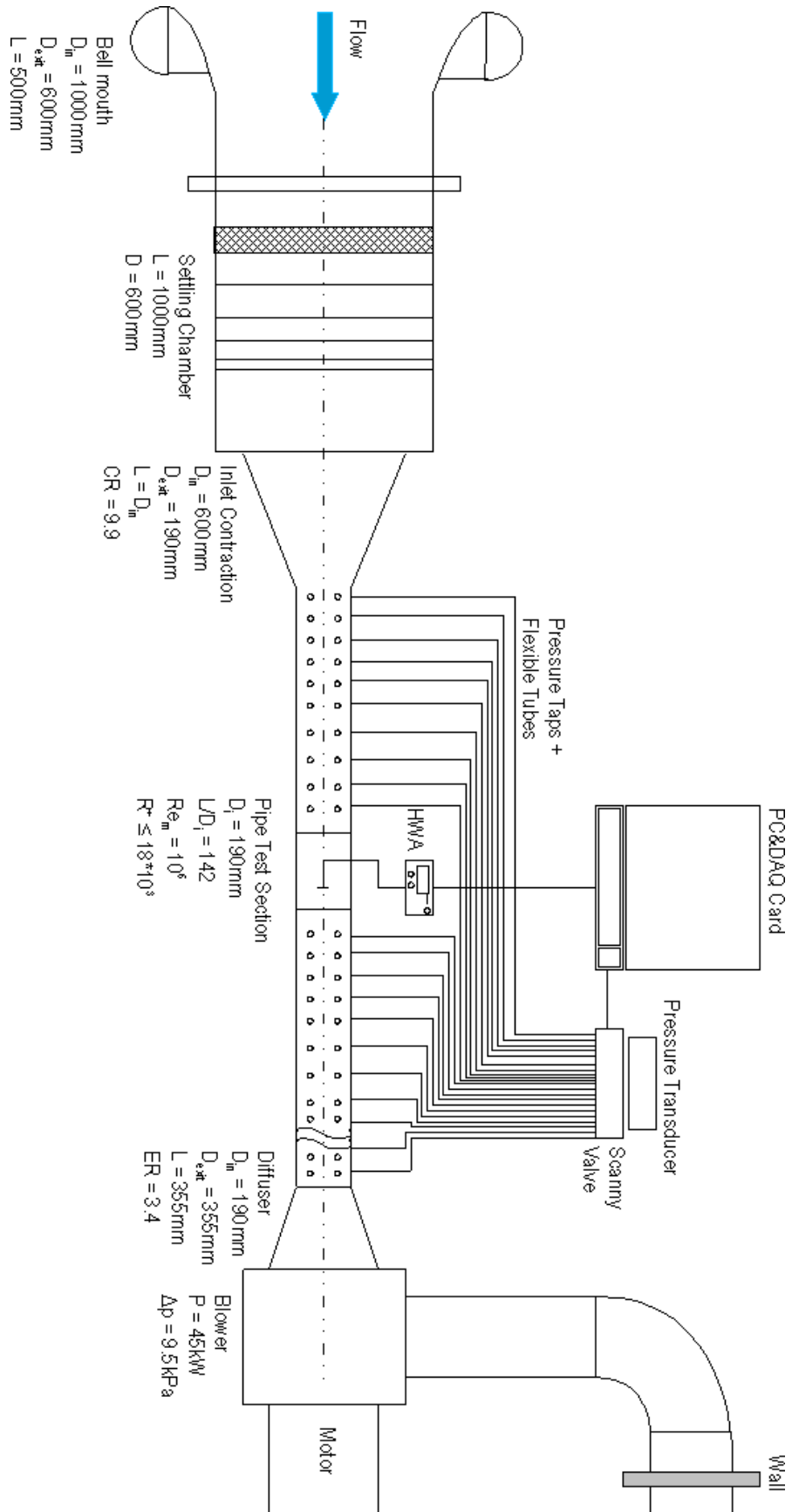


Figure 6.5: Former pipe facility (open wind tunnel).

three quantities are:

$$Tu = \frac{\sqrt{\overline{u'^2}}}{\overline{U_c}}, \quad (6.1)$$

$$S_c(\overline{u'}) = \frac{\overline{u'^3}}{\sqrt{\overline{u'^2}}^3} \quad (6.2)$$

$$F_c(\overline{u'}) = \frac{\overline{u'^4}}{\sqrt{\overline{u'^2}}^4} = \frac{\overline{u'^4}}{\overline{u'^2}^2} \quad (6.3)$$

The presented results, which are in a similar way shown in Zimmer et al. [117], for the statistical quantities, named the second, third and fourth-order moment about the mean show all a similar behavior. They start to develop from their initial value until its maximum is approached. This length, in this case at around $x/D = 38$, is believed to be the length the flow needs to become transient, i.e. from uniform flow conditions at the pipe inlet to laminar flow state until beginning of transition. After the complete transition from laminar to turbulent flow the turbulence intensity level, the skewness factor and the flatness factor approach to a constant value. Here, the turbulence intensity $Tu \approx 3.4$, $S_c(\overline{u'^2}) = -0.5$, and $F_c(\overline{u'^2}) = 3.5$. These values confirm earlier investigations by Kreplin and Eckelmann [55] and Sreenivasan and Antonia [94], with slight deviations, for fully developed channel flow. This process is completed at approximately $x/D = 75 - 80$. Thereafter it is believed that the flow is fully developed turbulent due to the invariant behavior of the statistical quantities with respect to the pipe test section length x [116]. This is confirmed by the mathematical relation for n-moments about the mean

$$\frac{\partial \overline{M^n}}{\partial x} = 0, \quad \forall x_1 > x_{1,v}, \quad (6.4)$$

The above relation yields a good criterion to fulfill the assumptions of the fully turbulent flow state by carrying out intensive centerline measurements. It turns out [116] that Equation 6.4 is valid even for channel flow, and is in good agreement with the proposed criteria of Patel and Head [78] and Zagarola and Smits [110], respectively.

In conclusion, the recently introduced measurements are the very first experimental data conducted at the new CoLaPipe test facility. They are treated as a calibration necessary

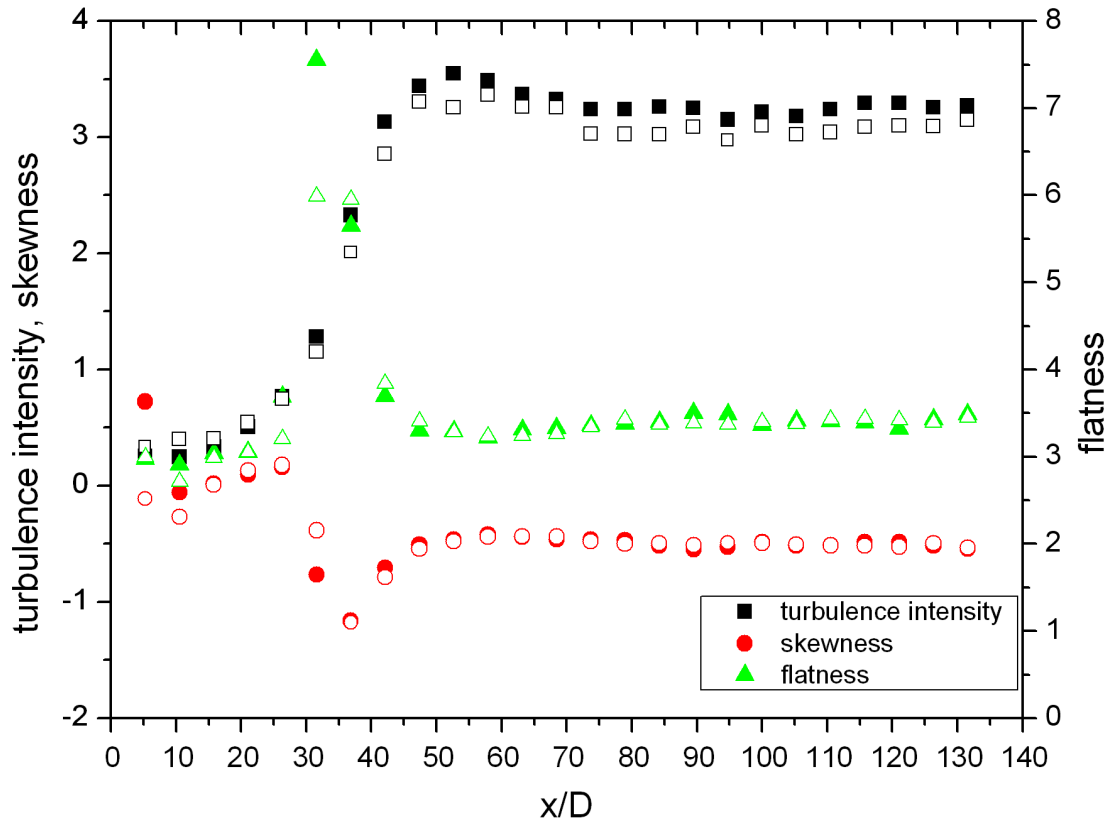


Figure 6.6: Development of statistical quantities along pipe test section for two different Reynolds numbers. The open symbols represent a bulk-based Reynolds number of 1.8×10^5 , whereas the filled symbols represent a bulk-based Reynolds number of 4×10^5 .

to confirm or even disprove the design considerations described in detail in Chapter 4. Hence, with these first results the development length for the natural transition scenario within the CoLaPipe is estimated, and confirms the investigation by Patel and Head [78] and Zanoun et al. [116], who verified a minimum development length of $x/D = 70$. On the other side the presented results disproves the suggestions from the *SuperPipe*, where a minimum development length of $x/D = 145$ is appropriate [108]. Therewith it is clear, that the CoLaPipe is a suitable facility to investigate high Reynolds number turbulent pipe flow.

6.3 Development Length - Artificial Transition Case

As we know from literature the influence of the development length on experimental design is significant, e.g. the necessary physical laboratory space to build up a large

pipe test facility with the application at high and very high Reynolds numbers. In the case of the CoLaPipe our design considerations are on the basis of investigations by Nikuradse [74], Laufer [57], Patel and Head [78], Doherty et al. [22] and the preliminary results obtained by Zanoun et al. [116]. These assumptions are validated in the previous chapter. Nevertheless, there are further considerations on this sensitive topic, like a possible reduction of the development length with respect to an earlier transition. Regarding this reduction a common method exists, which is applied by; e.g.; Laufer [57] in a pipe facility and by Fischer [30] for channel flow. This method aims for an earlier transition from laminar to turbulent flow utilizing well-defined perturbations. These disturbances are applied to the inlet of the test facility, where the uniform velocity profile is dominant, and initiates artificial transition with a reduced development length. Such considerations and results [30, 57] are the basis for further experiments at the CoLaPipe to investigate the aforementioned influence on the development length. If a reduction is successful this would have a great impact on the remaining length of a test section to investigate fully developed pipe flow turbulence, and additionally in the design phase of such an experiment the overall test section length can be considered smaller. To realize a well-defined perturbation on the inlet flow different methods are available, like orifices depicted in Figure 6.4a or organized tape letters shown in Figure 6.4b. Both techniques are described in Chapter 6.1.3. Within this thesis only investigations using orifices are presented. Measurements on organized tape letters are planned in the near future.

The procedure for the investigation of artificial transition and the possible influence on the development length is the same as for the natural transition case. This means that single-wire HWA centerline measurements are conducted starting at the inlet part of the pipe, along the pipe test section until the very end of the facility is reached. The measured data sets, which include the mean and fluctuating velocity, are then evaluated based on the Equations 6.1, 6.2 and 6.3. The resulting statistical quantities, i.e. Tu , $S_c(\overline{u'^2})$ and $F_c(\overline{u'^2})$, are shown as a function of the normalized pipe length L/D , respectively, in Figure 6.7, Figure 6.8 and Figure 6.9.

One main difference between the results for either natural and artificial transition is the initial value for all three statistical quantities. In the case of artificial transition the initial value for the turbulence intensity is very high ($Tu_{art} \approx 8$) compared to natural transition ($Tu_{nat} \approx 0.5\%$ at maximum Reynolds number). Figure 6.7 shows six different Reynolds numbers ($9.9 \times 10^4 \leq Re_m \leq 7.03 \times 10^5$) and the proper turbulence intensities, which are $7.5\% \leq Tu \leq 8\%$. This increase in Tu right at the beginning of the pipe test section can be explained through the utilization of an external disturbance to force early transition. During the evolution of the flow the turbulence intensity value at the center part of the pipe decreases. Hence, the flow damps the disturbance and the

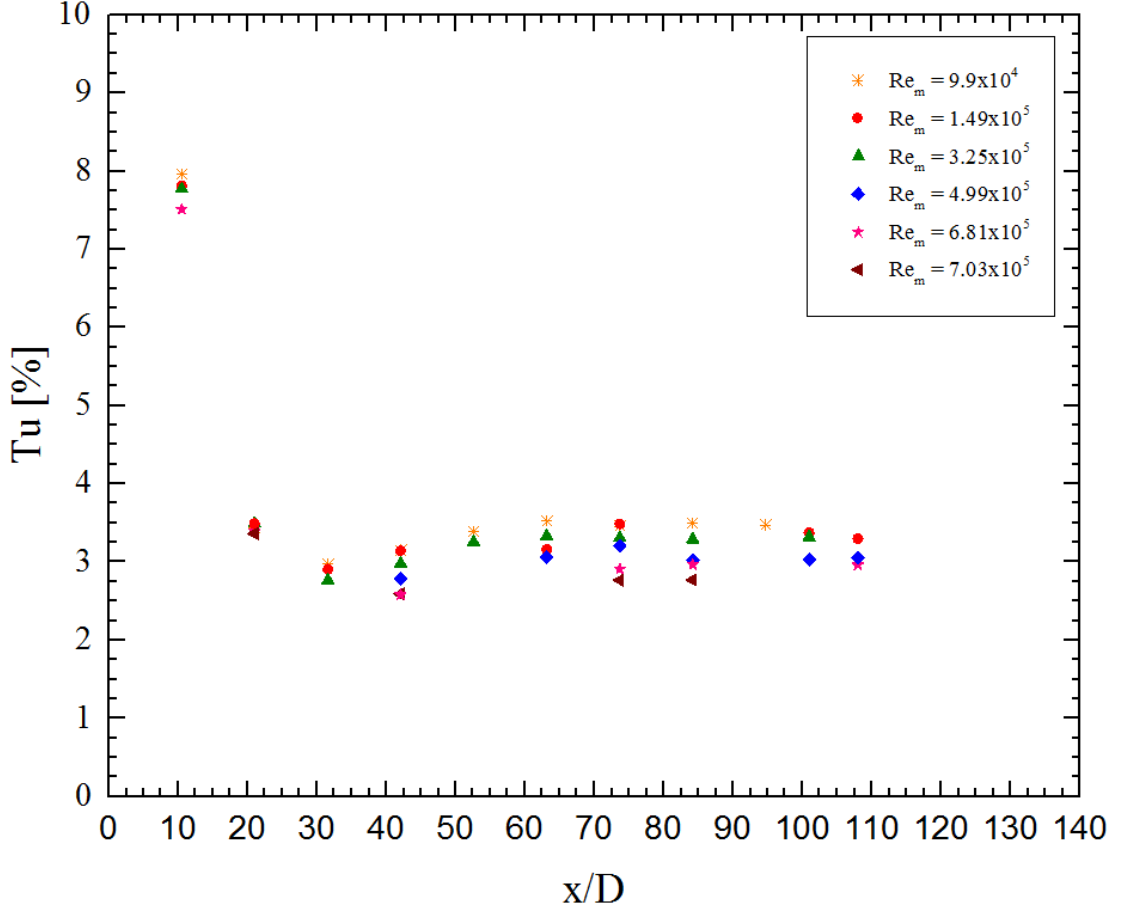


Figure 6.7: Development of centerline turbulence intensity along pipe test section representing six different Reynolds numbers ($9.9 \times 10^4 \leq Re_m \leq 7.03 \times 10^5$).

influence on the flow development also decreases. Finally, the turbulence intensity level Tu approaches a constant value ($\approx 3.15\%$) at $x/D \approx 70$. Further on it is invariant in streamwise direction. A similar results is found for natural transition. Based on the proposed criteria for higher order moments (Equation 6.4) the fully developed turbulent flow state is identified [57]. Nevertheless, further investigations by Zagarola [108] and Zanoun et al. [116] have shown, that merely the first and second-order moment about the mean are not appropriate, and that the third and fourth-order moment have to be taken into account, too.

The behavior of the skewness factors, representing the third-order moment about the mean, as a function of the centerline mean velocity are shown in Figure 6.8 also for six different Reynolds numbers. And it is obvious from the presented figure that the trend is the same as for the turbulence intensity Tu . The initial value is higher ($S_c(\overline{u'^2}) \approx 0.5$) compared to the natural transition scenario ($S_c(\overline{u'^2})_{nat} = -0.01$). But after approaching the minimum value, at around $x/D \approx 31$, the skewness factor approaches a constant

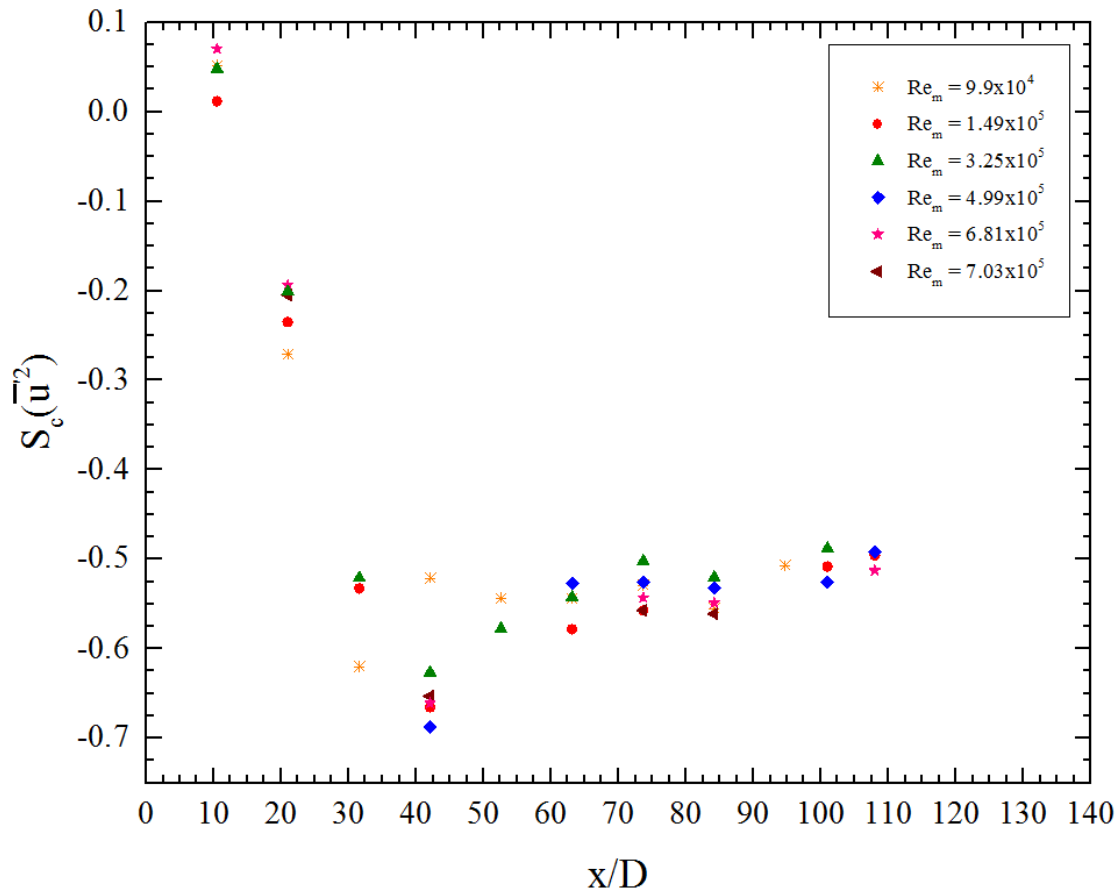


Figure 6.8: Development of centerline skewness factor along pipe test section representing six different Reynolds numbers ($9.9 \times 10^4 \leq Re_m \leq 7.03 \times 10^5$).

value and remains constant for the rest of the pipe length, i.e. invariant behavior in streamwise direction. With this data set a minimum development length of $x/D \approx 70$, respectively, is estimated.

Facing the fourth-order moment shows no significant differences in the overall behavior with respect to the test section length, which can be followed in Figure 6.9. The entrance boundary conditions, note the application of a disturbance at the inlet of the pipe test section, have no significant influence on the initial value of $F_c(\overline{u'^2})$, which is $F_c(\overline{u'^2}) \approx 2.92$. Nearly the same value can be obtained from Figure 6.6 for natural transition. Further on, the flatness factor becomes maximal, which is nevertheless considerably smaller as for natural transition. This occurs between a pipe length of $x/D = 31$ and $x/D = 40$. After the complete transition process the flow state changes to fully turbulent and hence the flatness factor approaches a constant value, $F_c(\overline{u'^2}) \approx 3.45$. This final value is nearly the same as for natural transition.

To summarize, the influence of well-defined disturbances, i.e. partial inlet block-

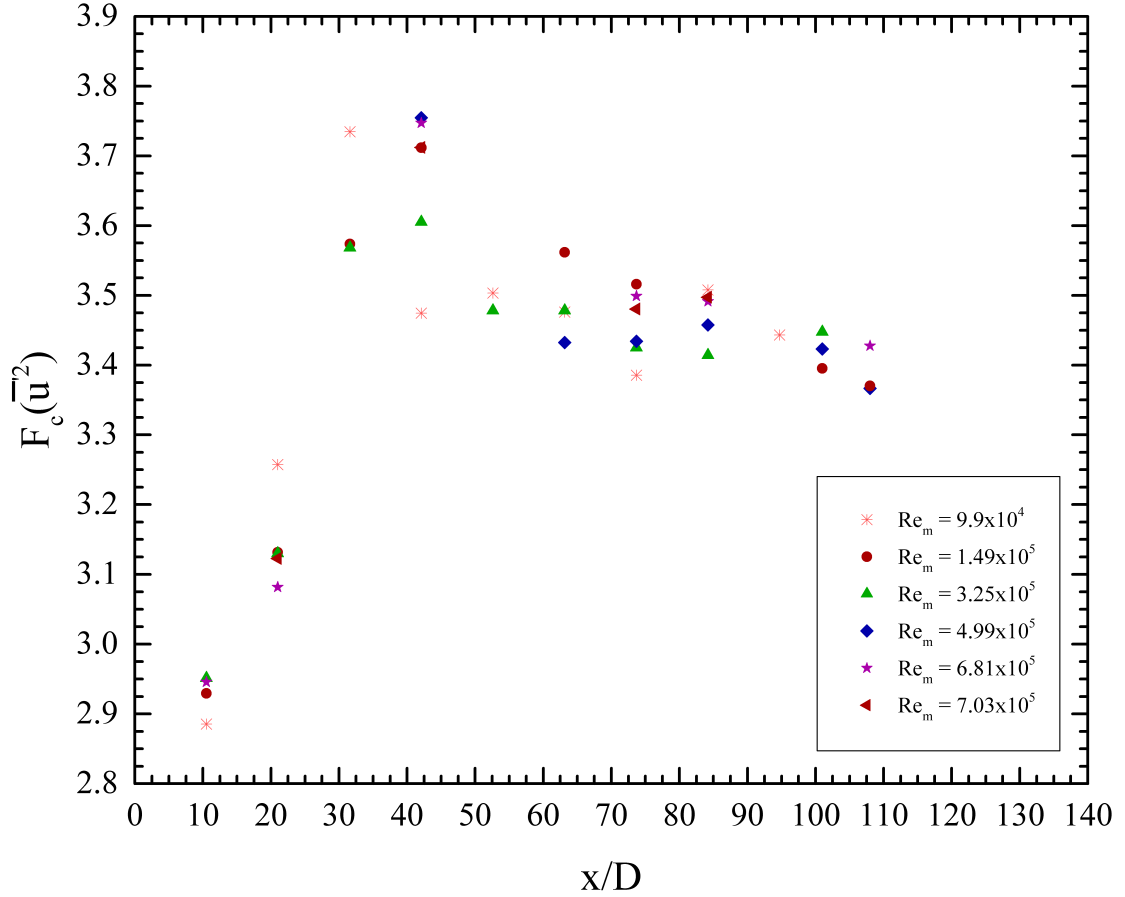


Figure 6.9: Development of centerline flatness factor along pipe test section representing six different Reynolds numbers ($9.9 \times 10^4 \leq Re_m \leq 7.03 \times 10^5$).

age, on the development length, which is defined as the minimum length the flow needs to develop from laminar flow to fully turbulence is investigated. The main result from these intensive centerline measurements, starting at the pipe inlet and going to the very end of the test facility, is that there is no significant influence on the development length when using an orifice with a blockage ratio of 25%. This is in contrast to the results of Fischer [30], who found out that partial blockage is an effective triggering mechanism to force early transition, hence to minimize the development length. He also suggests, that a blockage ratio of more than 20% does not increase the influence, and therewith a critical blockage ratio is defined. These results can not be supported. Possible reasons for such varying results can be the different flow types. Fischer [30] investigates channel flow, which is also an internal wall-bounded flow, but is difficult to treat due to possible side wall effects. Maybe these effects, which are not negligible, have a great impact, too, when early transition is forced. Another reason for these deviations can results from the blockage ratio itself. It is possible that for pipe flow the critical blockage ratio has

to be higher to use the effect of decreasing the development length. To proof this option additional measurement series using tripping devices with a blockage ratio of 30%, 40% and 50% are recommended. A third reason, which is conceivable, is the resistance of pipe flow against such partial perturbation, like orifices. Perhaps, another triggering mechanism, like a turbulence grid, would be the way to success.

6.4 Estimation of Time-Averaged Wall Shear Stress

Estimating an accurate wall friction velocity u_τ is one of the basic topics when investigating pipe flow since u_τ is believed to be the appropriate scaling parameter when scaled on inner variables. Due to this importance it is obvious that the estimation has to be as accurate as is possible with respect to the available measuring technique to avoid uncertainty propagation. The occurring uncertainty is related to the density of the working fluid (ρ) and the wall shear stress (τ_w), which form the wall friction velocity:

$$u_\tau = \sqrt{\frac{\tau_w}{\rho}}. \quad (6.5)$$

For this presented work the density is estimated directly due to static pressure measurements. The underlying process is described in detail in Chapter 5.1. Whereas the estimation of τ_w is more difficult since there are some methods, which can be used. In the following some possible methods, like

- mean pressure gradient method,
- viscous sublayer profile method and
- Clauser chart method

are presented and discussed. Finally, the above mentioned methods are compared and a conclusion is drawn.

6.4.1 Mean Pressure Gradient Method

One of the key features of the CoLaPipe facility is the direct estimation of the wall shear stress $\overline{\tau_w}$ utilizing the mean pressure gradient method. It is believed [97] that this method, where it holds the requirements:

- i a fully developed flow state and
- ii the two-dimensionality of the flow (axisymmetric flow conditions),

is the most accurate one. The definition of $\overline{\tau_w}$ within circular pipe flow related to the mean pressure gradient is

$$\overline{\tau_w} = \frac{dp}{dx} \frac{R}{2} = \frac{dp}{dx} \frac{D}{4}. \quad (6.6)$$

To provide measurement data of the mean pressure gradient dp/dx with high accuracy (refer to Chapter 5.5), the overall pipe test section is equipped with pressure tappings. A detailed description of the installation, alignment and working procedure during the measurements is presented in Chapter 5.1.

The proceeding of calculating $\overline{\tau_w}$ using the mean pressure gradient method is rather simple. The mean pressure gradient is recorded for different boundary conditions, i.e. different Re_m . Then the raw data are imported to the commercial data analysis software OriginPro and plotted as a function of the streamwise distance x . In the following a linear fit in the form of

$$p = \frac{dp}{dx} x + a,$$

where a is a variable, is applied and the resulting slope delivers the desired value for dp/dx . A schematic is depicted in Figure 6.10.

For the calculation of dp/dx sufficient data points are taken into account, i.e. in general 15 - 20 distributed along the pipe test section length. The characteristic behavior of the inlet, the intersection from the settling chamber and the contraction unit to the pipe test section, is excluded due to the (i) requirement. The so derived value for the pressure gradient is then inserted in Equation 6.6. One exemplary result is presented in Table 6.1. Finally, the result is the time-averaged wall shear stress τ_w wherewith the scaling parameter u_τ can be calculated using Equation 6.5.

Table 6.1: Overview of exemplary wall shear stress data.

Re_m	dp/dx [Pa/m]	τ_w [N/m ²]	u_τ [m/s]	L/D
5.7×10^5	-99.04	4.705	2.014	84.2

The advantages of this direct method are clear. But during the application some disadvantages or difficulties have become apparent. The major problem is the number of

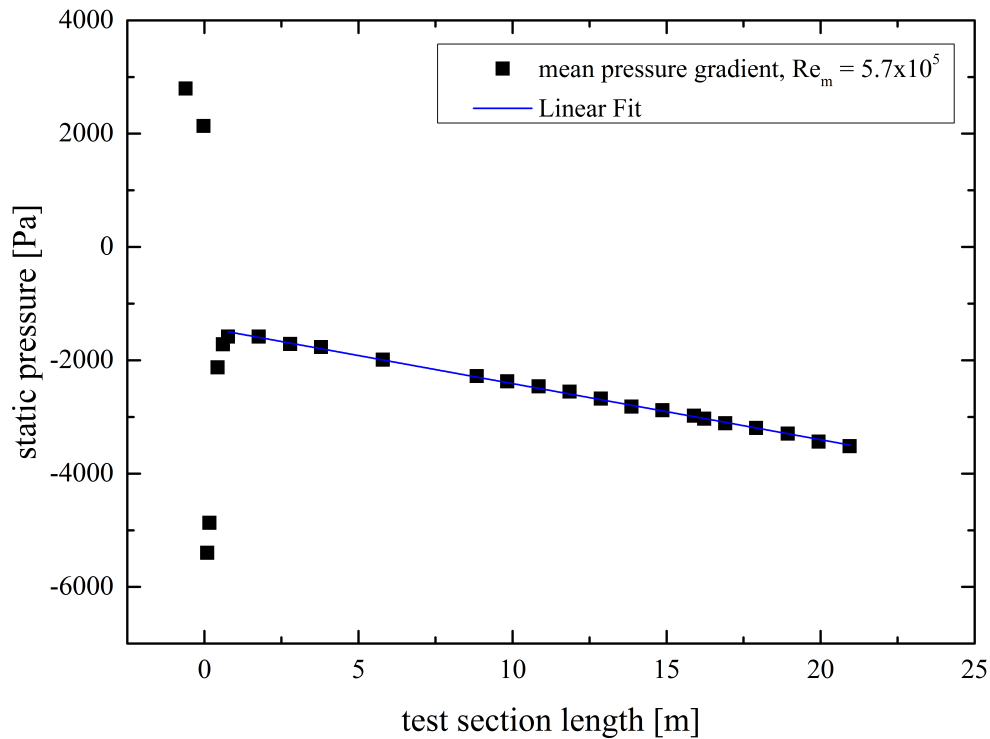


Figure 6.10: Filled symbols represent the development of the mean static pressure with respect to the streamwise distance x . Blue line indicates the applied linear fit to calculate the pressure gradient dp/dx in streamwise direction.

data points, which are taken into account while calculating the pressure gradient. This has a great impact on dp/dx and hence results in a broad deviation of u_τ . This is in a first step graphically shown in Figure 6.11, Figure 6.12, Figure 6.13 and Figure 6.14. Within a next step the deviation in u_τ is demonstrated and presented in Table 6.2. Also listed within this table is the error coefficient R_c , which is a statistical quantity to evaluate the result. It is obvious from the shown results that the wall friction velocity deviates between each other from about 4 % for the smallest mean pressure gradient. The minimal deviation is 0.88 % for a wall friction velocity of approximately 2.014 m/s.

This described disadvantage of the direct method to estimate the wall friction velocity comes also along with the problematic of the right scaling parameter for the mean velocity profile. This is furthermore discussed in Chapter 6.6.

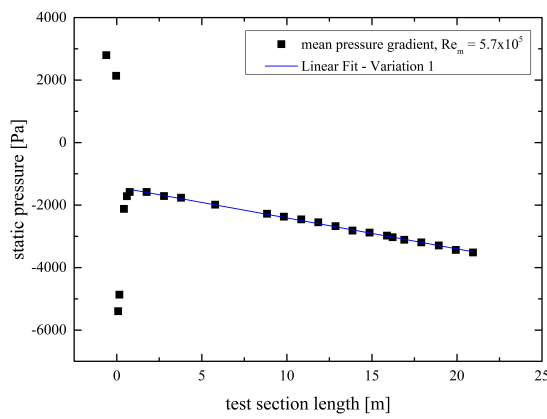


Figure 6.11: Development of the mean pressure gradient along the pipe test section.

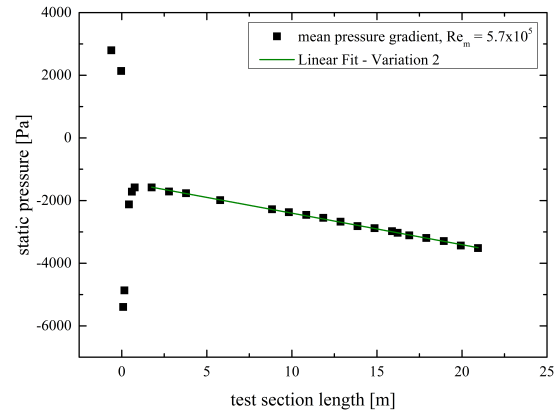


Figure 6.12: Development of the mean pressure gradient along the pipe test section with a first variation in data points.

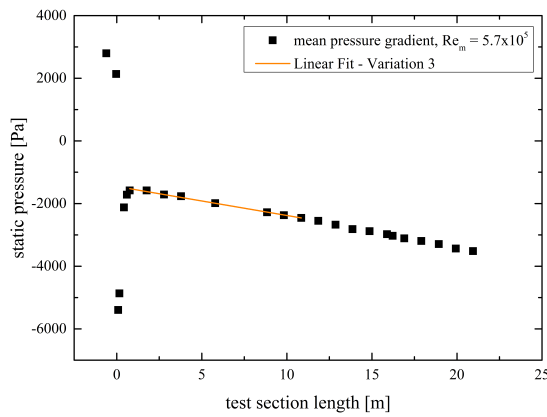


Figure 6.13: Development of the mean pressure gradient along the pipe test section with a second variation in data points.

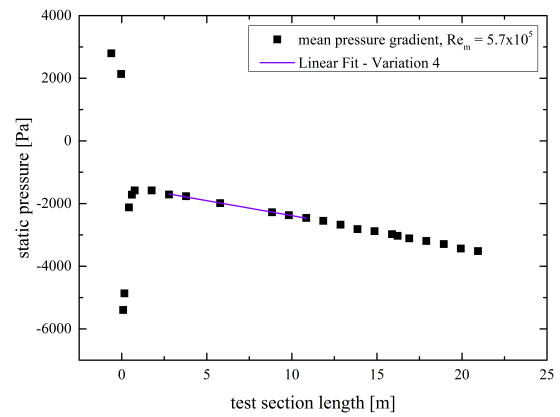


Figure 6.14: Development of the mean pressure gradient along the pipe test section with a third variation in data points.

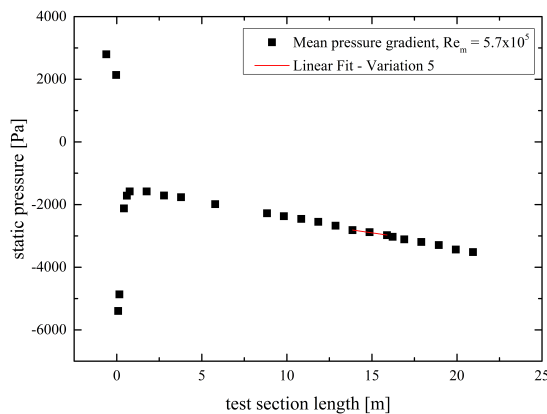


Figure 6.15: Development of the mean pressure gradient along the pipe test section with a fourth variation in data points.

Table 6.2: Comparison of wall friction velocity variation due to the change in the mean pressure gradient.

Re_m	dp/dx [Pa/m]	τ_w [N/m ²]	u_τ [m/s]	R_c	L/D
5.7×10^5	-99.04	4.705	2.014	0.99762	84.2
	-100.73	4.78	2.032	0.99894	
	-92.57	4.39	1.95	0.99176	
	-95.75	4.55	1.98	0.99746	

6.4.2 Viscous Sublayer Profile Method

The underlying basis for this method, to estimate the wall friction velocity u_τ from Equation 6.5, is the following relation:

$$\overline{\tau_w} = \mu \frac{\partial U}{\partial y}, \quad (6.7)$$

where $\partial U/\partial y$ is the velocity gradient in wall normal direction. This method can be considered as direct due to the quantification of the mean axial velocity gradient in the vicinity of the wall and with the assumption of knowing μ of the working fluid. The dynamic viscosity μ is a fluid property depending on the used working fluid, which calculation is presented in detail in Chapter 5.6.

An important requirement for the application of this method is a clear existence of a linear region in the velocity profile, where

$$U^+ = y^+ \quad (6.8)$$

is valid. This is given in the case of hydraulically smooth surfaces as in this study, which is verified in Chapter 4.1.2. The existence of this region comes along with certain challenges:

- i The viscous sublayer has a small physical dimension, typically a fraction of a millimeter, which has to be sufficiently resolved with the used measurement technique. It is believed [97] that the HWA-technique with a wire diameter of 5 μm or even smaller is small enough to obtain adequate data points, which is shown in the following.
- ii An accurate positioning of the hot-wire in the vicinity of the wall (refer to Chap-

ter 5.7) is important, respectively, due to the influence of the wall on the measurement results [50], i.e. thermal conductivity and aerodynamic blockage effects.

- iii The low velocities in the vicinity of the wall require an accurate calibration of the used HWA probes. Refer to Chapter 5.3.2 for a detailed description of the calibration procedure for single wire HWA probes.

Due to the validation of a hydraulically smooth inner pipe surface and the consideration of the above difficulties the approach to estimate $\overline{\tau}_w$ is as follows.

The raw data, here the time series resulting from the HWA measurements, are imported to OriginPro, and the time-averaged mean velocity \overline{U} is plotted as a function of the wall normal distance y , refer to Figure 6.16. Then a linear fit in the form of

$$\overline{u} = \frac{\partial u}{\partial y} y$$

is applied to determine the velocity gradient in wall normal direction. With $\partial u/\partial y$

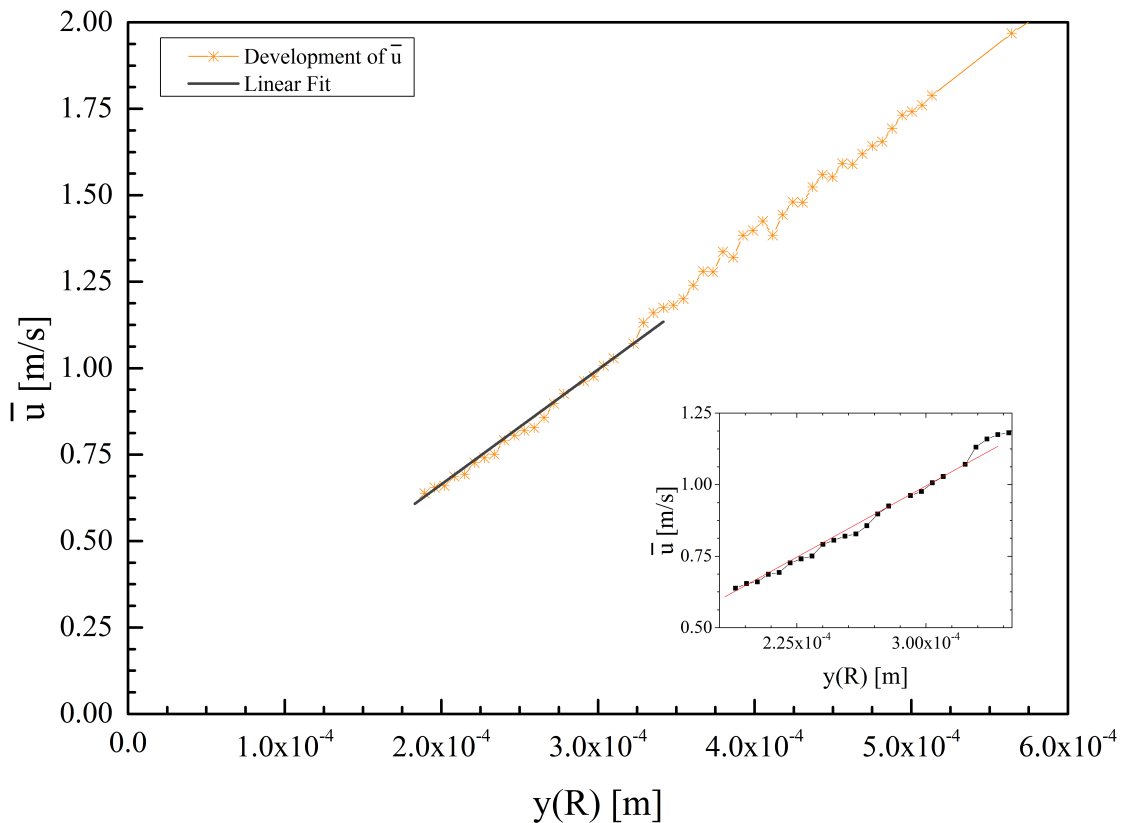


Figure 6.16: Symbols represent the linear behavior of the mean velocity in the vicinity of the wall. Additionally, the linear fit to derive the velocity gradient in wall normal direction.

and the determined dynamic viscosity μ the wall shear stress can be directly calculated using Equation 6.7. The final step is the derivation of the wall friction velocity u_τ utilizing Equation 6.5. An example is presented in the following table. As already

Table 6.3: Overview of exemplary wall friction velocity using the viscous sublayer profile method.

Re_m	$\partial u/\partial y$ [1/s]	τ_w [N/m ²]	μ [m ² /s]	u_τ [m/s]	Distance from inlet [m]
7.23×10^4	3302.23	0.051	1.55×10^{-5}	0.209	84.2

mentioned above this method has its major limitation in the utilization of sufficient data points within the viscous sublayer. Hence, for higher Reynolds numbers this method is unsuitable due to the decreasing viscous sublayer and therewith the increasing difficulty to resolve this layer with the common HWA measurement technique. An example for this is presented in the following.

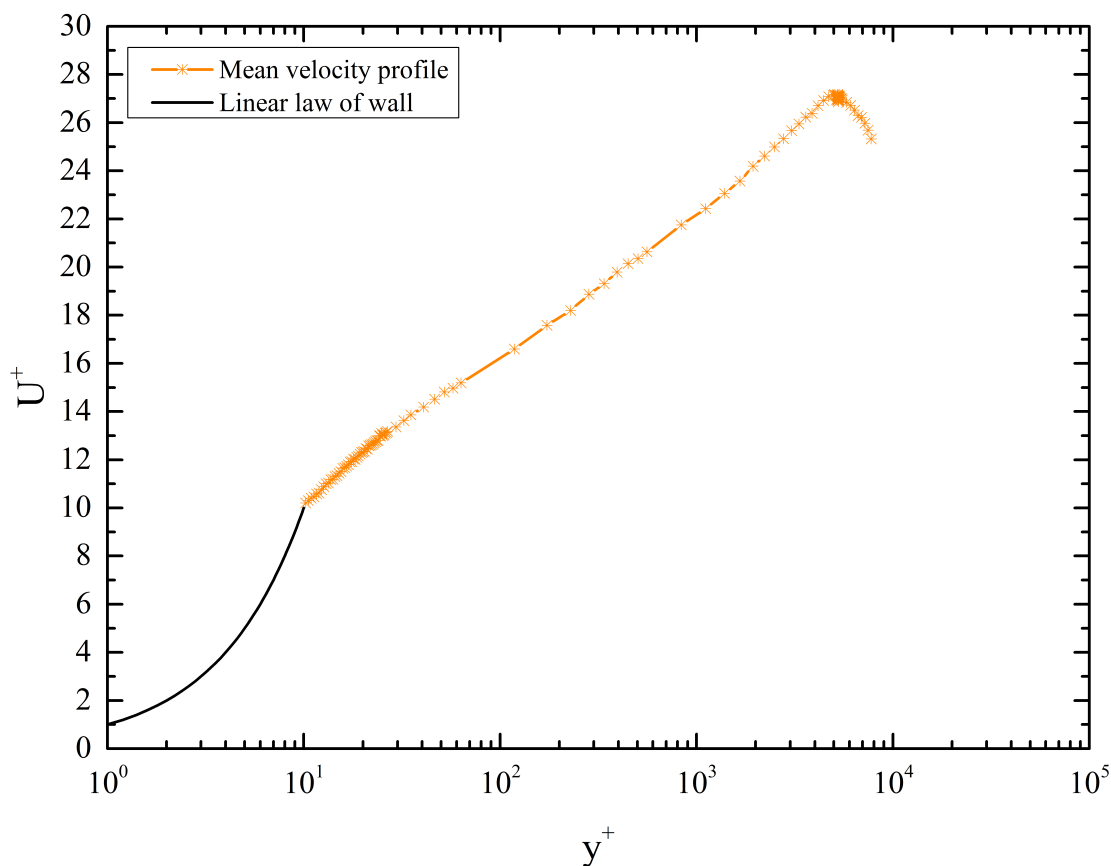


Figure 6.17: Mean velocity profile for $R^+ = 5.25 \times 10^3$ as a function of the dimensionless wall distance. The black line represents schematically the linear law of wall and therewith the viscous sublayer.

Figure 6.17 shows clearly that the viscous sublayer ($y^+ \leq 10$) can not be approached with the used HWA single-wire probe due to insufficient data points and hence the viscous sublayer profile method is not applicable. The consequence, which results out of this fact, is that the wall shear stress τ_w and therewith the wall friction velocity u_τ has to be calculated using either the direct mean pressure gradient method (refer to Chapter 6.4.1) or the indirect Clauser chart method. This procedure is described in detail in the following chapter.

6.4.3 Clauser Chart Method

The Clauser chart method is usually a graphical or indirect method to estimate the wall friction velocity u_τ . The underlying basis is the behavior of the time-averaged mean velocity profile in the logarithmic portion of the boundary layer, refer to Chapter 3.3. This requirement implies at the same time that this method is inappropriate if the flow system deviates from canonical behavior, i.e. no clear logarithmic part can be identified as in the case of rough surfaces. The mean velocity profiles presented within this work follow the required logarithmic behavior, and the inner pipe surface is considered as hydraulically smooth (refer to Chapter 3.3.3 and Chapter 4.1.2).

In the literature one can find different methods to calculate τ_w or u_τ [97], but compared to these, e.g. mean pressure gradient and viscous sublayer profile method, the greatest benefit of the Clauser chart method is that measurements within the viscous part of the boundary layer, which are difficult to obtain, are not required. A crucial disadvantage of this method is the not exactly allocable accuracy due to the indirectness and the dependence on the judiciously chosen parameter. In general the accuracy is approximately $\pm 5\%$. Nevertheless the Clauser chart method delivers useful information on the wall shear stress, which can be compared to other methods if possible, and serves at the same time as a validation for those (refer to Chapter 6.5).

Figure 6.18 represents the Clauser chart, which is constructed using the following basic definitions for the logarithmic law of the wall, the wall friction velocity and the friction coefficient, respectively:

$$\frac{U}{u_\tau} = \frac{1}{\kappa} \ln\left(\frac{y u_\tau}{\nu}\right) + B, \quad (6.9)$$

$$u_\tau = \sqrt{\frac{\tau_w}{\rho}}, \quad (6.10)$$

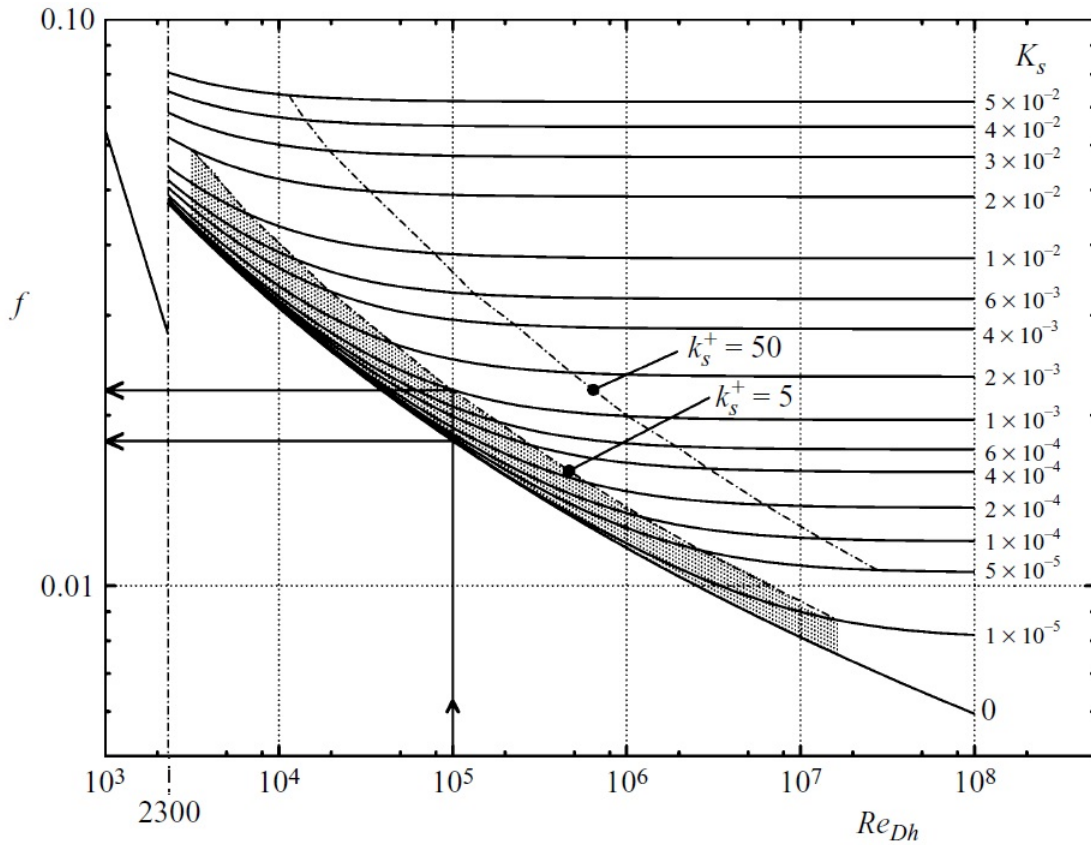


Figure 6.18: Clauser chart for pipes. From H. Herwig, D. Gloss, and T. Wenterodt, A new approach to understanding and modelling the influence of wall roughness on friction factors for pipe and channel flows, *Journal of Fluid Mechanics*, 613(-1), p. 37, reproduced with permission.

$$f = -\frac{dp}{dx} \frac{2 D_h}{\rho \bar{U}^2} = 8 \left(\frac{u_\tau}{\bar{U}} \right)^2, \quad (6.11)$$

$$Re_{D_h} = \frac{\bar{U} D_h}{\nu}. \quad (6.12)$$

Here, Re_{D_h} represents the Reynolds number based on the hydraulic diameter concept [35]. The parameter f is the friction factor and k_s^+ is the equivalent sand grain roughness [91]. The Grey shaded area in Figure 6.18 marks the part for hydraulically smooth surfaces.

In accordance to the logarithmic law assumptions κ and B in Equation 6.9 are constants,

which vary from source to source depending on the boundary conditions [7]. Hence, the value for κ is 0.41 and $B = 5.0$, respectively, according to the most often cited values of von Kármán [99]. The Clauser chart itself represents the friction factor f as a function of the Reynolds number based on the hydraulic diameter. The logarithmically varying lines in the Clauser chart are derived from Equation 6.11 through certain values for f . If the measured mean velocity is then plotted onto the Clauser chart through Equation 6.11 with respect to the Reynolds number the corresponding value for the wall friction velocity can be estimated by the best fit compared to the varying f -lines.

To prove the results from the direct measurement of τ_w using the mean pressure gradient method the friction factors for four different Reynolds numbers are estimated and plotted as a function of the Reynolds number. Here, different friction factors for one Reynolds number are shown, which arise from a variation in the calculated mean pressure gradient. This circumstance is described in details in Chapter 6.4.1. Hence, a Clauser chart shown in Figure 6.19 is reproduced using CoLaPipe results. To compare these results the famous measurement data of Nikuradse [74] and Blasius [14] are presented, as well as the friction factor results from the *SuperPipe* published by McKeon et al. [66]. We can see from this chart that the calculation of the friction factor is very sensitive if we take the mean pressure gradient method into account. But this figure shows also that at higher Reynolds numbers this effect becomes less important. If we now use the Clauser chart in the original way, which means that the friction factor is read from the chart itself and than the wall friction velocity is estimated, the CoLaPipe Clauser chart can be rearranged as in Figure 6.20.

Table 6.4: Calculated wall friction velocity u_τ from Clauser chart for different Reynolds numbers.

Re_m	friction factor f	wall friction velocity u_τ
7.28×10^4	0.0193	0.28999
2.55×10^5	0.139	0.86311
3.91×10^5	0.0126	1.25833
4.99×10^5	0.01185	1.53765
5.68×10^5	0.0117	1.7915

From the above described procedure we are now able to calculate the friction velocity u_τ using Equation 6.11. The results are presented in Table 6.4. They are further used to scale the mean velocity profiles, which is presented in Chapter 6.6.

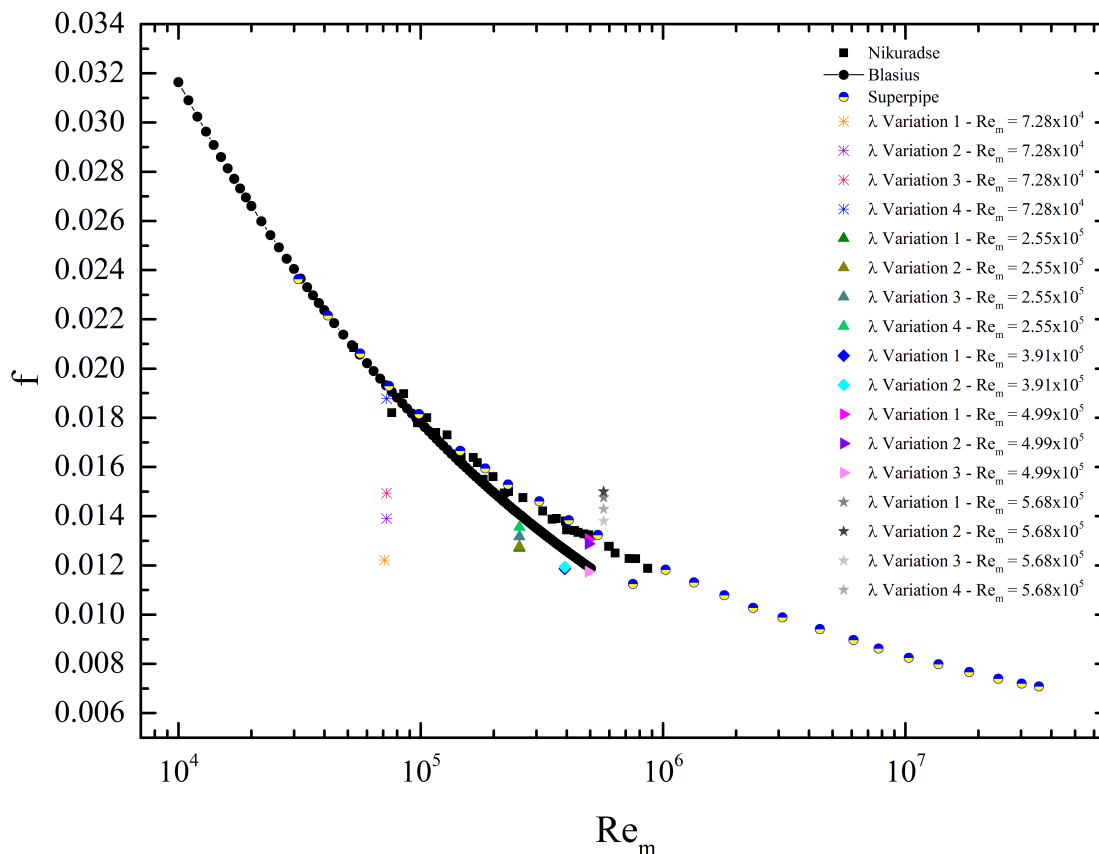


Figure 6.19: CoLaPipe Clauser chart with results from Nikuradse [74], Blasius [14] and McKeon et al. [66]. Represented is the friction factor f as a function of the bulk based Reynolds number.

6.5 Comparison of Different Methods

The aforementioned chapter deal with the measurement of τ_w and the calculation of the wall friction velocity u_τ , which is of vital importance due to the scaling of the mean velocity profile in pipe flow. This important value is either computed using a direct or indirect procedure. This chapter serves as a summary for the three presented methods and shows in a comparison the advantages and disadvantages, refer to Table 6.5, when applying them onto measurement data sets.

The first introduced method is the mean pressure gradient method. It combines a direct procedure with a high accuracy result. But the disadvantages unfortunately prevail, which are the difficult implementation at the test facility due to the size of the pressure tappings [64], and the requirement of well defined data points over which the pressure gradient is estimated [108]. At the CoLaPipe the necessity of an integral determination of the bulk velocity turned out to be a problem as well due to artificial transition,

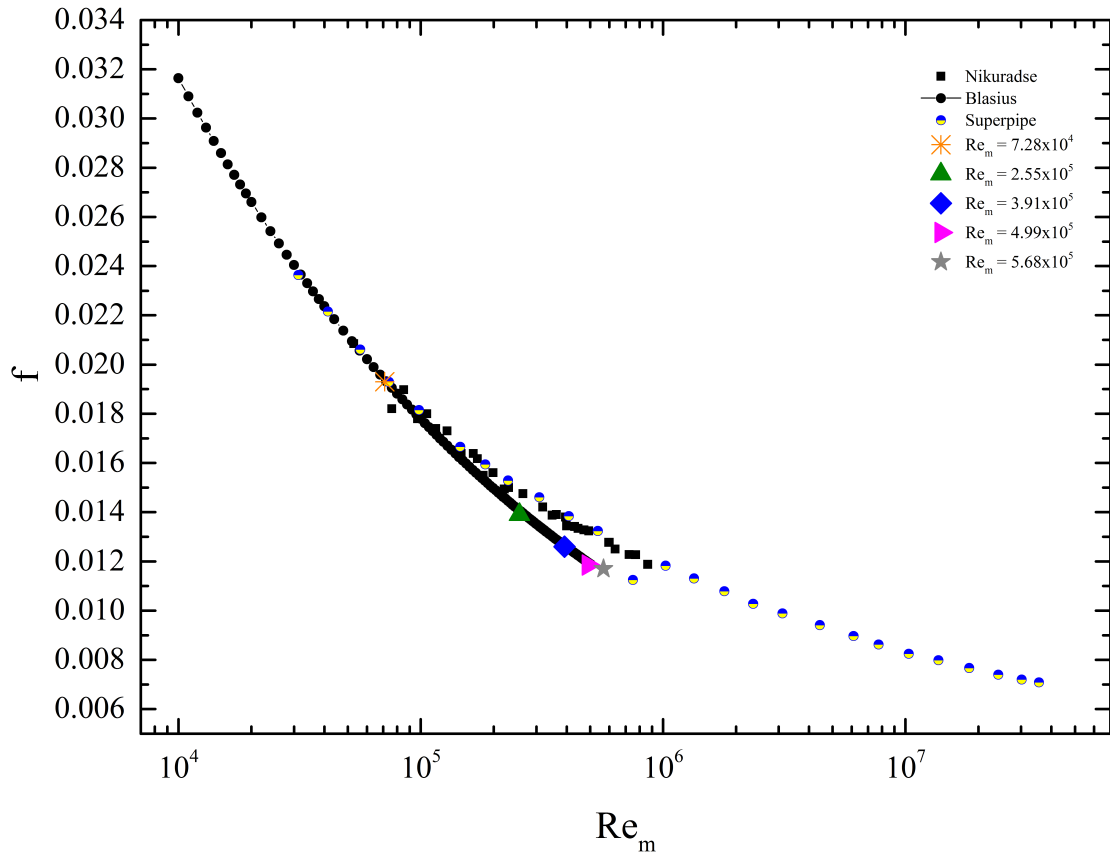


Figure 6.20: Clauser chart with CoLaPipe results. Shown is the friction factor f as a function of the bulk based Reynolds number.

which precludes the possibility of measuring the bulk velocity at the inlet of the pipe test section. The second described method is also a direct method - the viscous sublayer profile method. This procedure has the advantage of a high accuracy result, too. But the problem in practice deepens with increasing Reynolds number since the viscous sublayer diminishes and hence it is not possible to sufficiently resolve this very small layer with the utilized HWA. The third presented method is the Clauser chart method, which is an often used engineering solution. It is an indirect, graphical procedure wherewith no data points within the viscous sublayer are required. This strongly relieves the estimation of the wall friction velocity u_τ . But it shows a great disadvantage, which is the predefinition of the constants κ and B in the logarithmic law. Here, the long lasting discussion on the universality of κ is very active since Bailey et al. [7] introduced some new findings covering a broad range of data sets. Nevertheless, this method works well and serves as a reference in comparison to the other two direct methods.

To give the best overview about the differences of these introduced methods Table 6.6 lists the estimated wall friction velocities. The range of u_τ for the mean pressure gradient results out of the different possibilities in defining the pressure gradient. It is obvious

Table 6.5: Advantages and disadvantages of different methods to calculate the wall shear stress u_τ .

method	advantages	disadvantages
mean pressure gradient	- direct - high accuracy	- well defined range for pressure gradient is required - integral determination of bulk velocity is required due to artificial transition - difficult implementation
viscous sublayer profile	- direct - high accuracy	- sufficient data points within viscous sublayer are required
Clauser chart	- no data points within viscous sublayer required - graphical method	- imprecise due to predefined constants κ and B

from this table that the variation in the wall friction velocity is broad and hence the effect on the scaling of the mean velocity profile using inner variables is great. To show this and to compare with the literature again the following chapter deals with the topic mean velocity scaling.

Table 6.6: Results for the wall friction velocity u_τ with different basic principles.

method	Re_m	wall friction velocity u_τ [m/s]
mean pressure gradient	7.23×10^4	$0.226 \leq u_\tau \leq 0.286$
viscous sublayer profile	7.23×10^4	0.209
Clauser chart	7.23×10^4	0.289

6.6 Mean Velocity Scaling

The scaling of the mean velocity is a highly debated topic, which engages scientist since the pioneering experiments of Reynolds [85] in the late 19th century. A very recent topic

on this comes from Bailey et al. [7], who analyzed 5 different data sets with the focus on the *von Kármán* constant κ . Their finding supports the well known controversy of defining the *von Kármán* constant κ as a universal parameter. Within their results κ is differing between $0.39 \leq \kappa \leq 0.421$, with κ estimated from least-squares fit of friction factor fit and centerline velocity fit. Nevertheless, they state a value for the *von Kármán* constant of 0.4 ± 0.02 , but with the background of an insufficient confidence interval [7]. This fact can not be solved, recently, by using modern established measurement techniques. Hence, they claim an improvement of the instrumentation to overcome this problem and to resolve κ more precisely. At the end the problem of estimating κ is due to the resolution of the mean and fluctuating velocity in the vicinity of the pipe wall, the estimation of the wall friction velocity u_τ either using a direct or an indirect technique, and the integration methods of estimating bulk properties [7]. This is also shown in the following mean velocity scaling results measured at the CoLaPipe test facility, where the differences come from the different procedures, which were discussed in the chapter before, to calculate the inner scaling parameters τ_w and u_τ , respectively.

Figure 6.21 shows a comparison of the influence of the evaluation method to estimate the wall friction velocity u_τ for an intermediate Reynolds number $Re_m = 7.23 \times 10^4$, when used as the scaling parameter. Also presented is the linear law of the wall, which is very important on one side for the viscous sublayer profile method, where an adequate resolution of this near wall field is necessary. And on the other side to collect information about the distance between the pipe wall and the HWA single-wire probe. These information are very sensitive due to the resulting uncertainty in u_τ [88]. For the shown bulk-based Reynolds number it is possible with the utilized measuring technique to sufficiently resolve the near wall flow field. Hence, a minimum value for y^+ of about 3 can be obtained. This is also the minimum value for y^+ presented by Hultmark [46] and Hultmark et al. [48]. Even depicted within Figure 6.21 is the logarithmic law, but for three different parameter sets, which were used to construct them. The classical and well known parameter come from von Kármán [99], which are represented by the pink line. Modified values for κ and B come from Zanoun and Durst [114], refer to the brown line. And McKeon et al. [65] also presented varying values for κ and B, which are represented by the turquoise line.

It is clear from this figure that the scaling of the mean velocity profile strongly depends on the scaling parameter, which is in the case of an inner scaling the wall friction velocity u_τ . The applied methods for an estimation of u_τ all provide different values, and hence the slope of the mean velocity profiles vary. This fact is indicated through the black arrow within Figure 6.21, which shows also the direction of the increasing wall friction velocity. The first, second and third variation of the mean pressure gradient to calculate u_τ result in an underestimated value. The same result is obtained for the

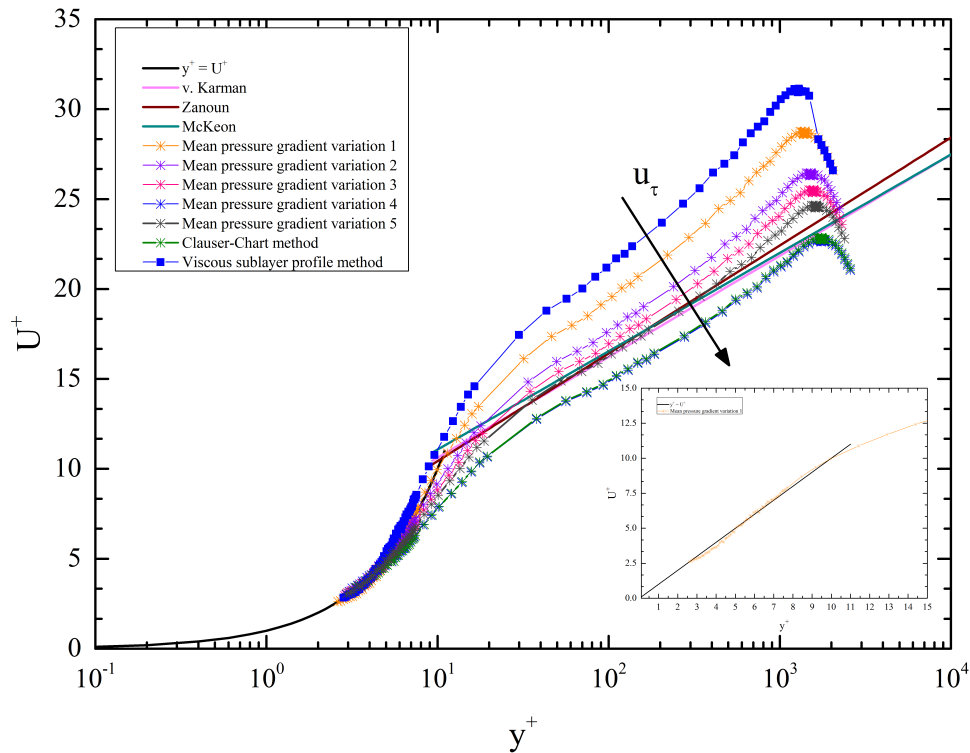


Figure 6.21: Mean velocity profiles for $Re_m = 7.23 \times 10^4$ obtained by different manipulation procedures. The black line represents the linear law of the wall. The pink (von Kármán [99]), brown (Zanoun and Durst [114]) and turquoise (McKeon et al. [65]) lines represents the logarithmic law with varying constants κ and B .

viscous sublayer profile method. Whereas the fourth variation of the mean pressure gradient and the Clauser-Chart technique generate an overestimated value. An exception is the dark gray colored mean velocity profile, where the mean pressure gradient variation is manipulated until the scaling parameter u_τ matches with the logarithmic law. This procedure is comparable with the in Chapter 6.4.1 described one, but for a higher bulk-based Reynolds number. The found deviation of the CoLaPipe mean velocity profiles due to the under- and overestimation of the wall friction velocity from the logarithmic law is therewith clear. And hence, this is believed to be an artifact due to the already claimed problems by Bailey et al. [7], which are:

- resolution of mean and fluctuating velocity in vicinity of wall,
- estimation of bulk properties using integration methods,

- application of direct methods for estimation of wall friction velocity, and
- implementation of indirect procedures to estimate wall friction velocity.

These results show also, that only one mean velocity profile follows the linear law of the wall, which is the mean pressure gradient variation 1 represented by the orange colored line. This is in detail shown within the cutout in the lower right part of Figure 6.21.

A second example for the scaling of the mean velocity profile is depicted in Figure 6.22. It shows also the differences in the wall friction velocity u_τ , when using different estimation methods, the linear law of the wall, and the logarithmic law for different constants κ and B, for a bulk-based Reynolds number of $Re_m = 5.7 \times 10^5$. Not shown is the result for the viscous sublayer profile method due to the absent data points in the linear part of the velocity profile. Hence, an estimation of u_τ using this method is not possible.

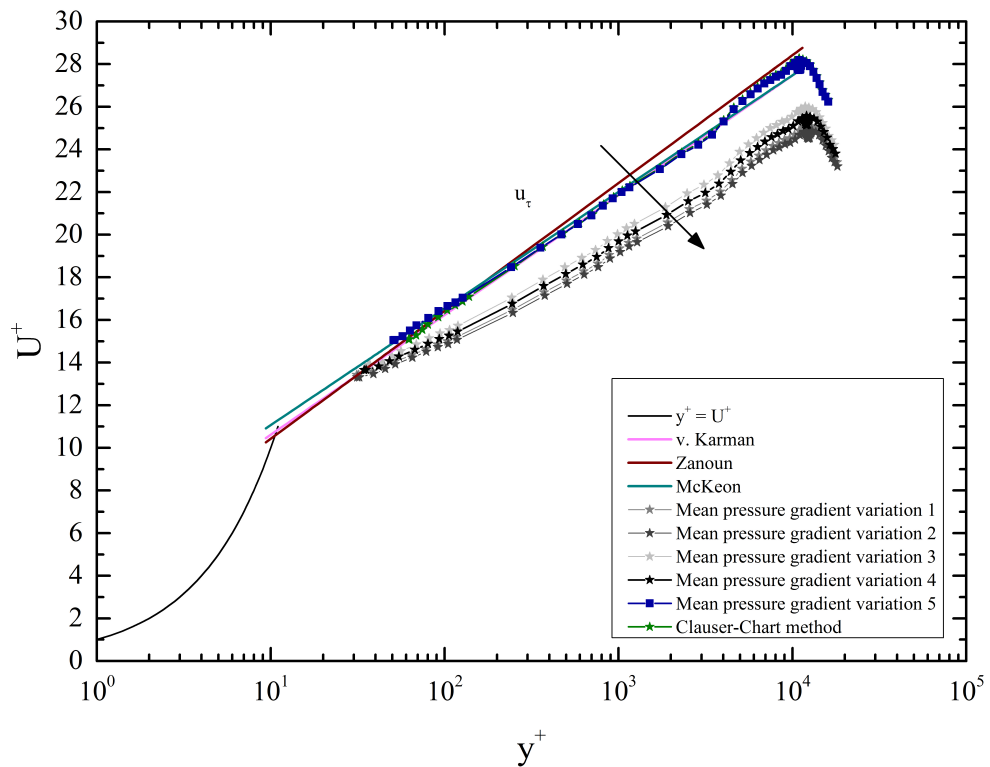


Figure 6.22: Mean velocity profiles for $Re_m = 5.7 \times 10^5$ obtained by different manipulation procedures. The black line represents the linear law of the wall. The pink (von Kármán [99]), brown (Zanoun and Durst [114]) and turquoise (McKeon et al. [65]) lines represents the logarithmic law with varying constants κ and B.

From Figure 6.22 we see that the variation 1-4 of the mean pressure gradient results in an overestimated value for the wall friction velocity u_τ . But that a stronger manipulation of the pressure gradient leads to an agreement with the logarithmic law defined by κ and B of von Kármán [99], refer to the blue line. This can also be seen more clearly in Chapter 6.4.1, where the 5 variations in the mean pressure gradient are depicted in discussed. The same result is obtained by applying the Clauser-Chart method on the data set, which is represented within Figure 6.22 by the green line. It is even obvious from these results that with the used HWA single-wire measurement technique no adequate resolution of the near wall region is possible. Hence, the mean velocity profile starts at $y^+ \geq 30$. This is a well known problem because on one side the viscous sublayer diminishes with increasing Reynolds number, wherewith a sufficient resolution of the flow field is difficult when utilizing such a measurement technique. And on the other side the air load on the probe and the probe support increases, respectively, and hence a resulting bend of the system hinders a more accurate positioning of the HWA single-wire.

6.7 Scaling of Fluctuating Velocity

Next to the already discussed inconsistencies, which come along with the scaling of the mean velocity profile, the scaling of the fluctuating velocity is not less debated. Here, recent publications [2, 47, 50, 86, 87] deal with:

- independence of inner peak with respect to Reynolds number,
- spatial and temporal resolution of fluctuating velocity,
- emergence of second outer peak in fluctuating velocity profile,
- arising artifacts due to utilized measurement techniques, like hot-wire length-to-diameter ratio.

To support the ongoing discussion on this topic broad data sets of the measured fluctuating velocity from the CoLaPipe are presented and analyzed. Here, the first figure (Figure 6.23) represents a summary of the raw fluctuating velocity profiles for five different bulk-based Reynolds numbers, which are merely scaled with the inner scaling

parameter u_τ . Here, u'^+ and y^+ are defined as in the following:

$$u'^+ = \frac{\sqrt{u'^2}}{u_\tau}, \quad (6.13)$$

$$y^+ = \frac{y * u_\tau}{\nu}. \quad (6.14)$$

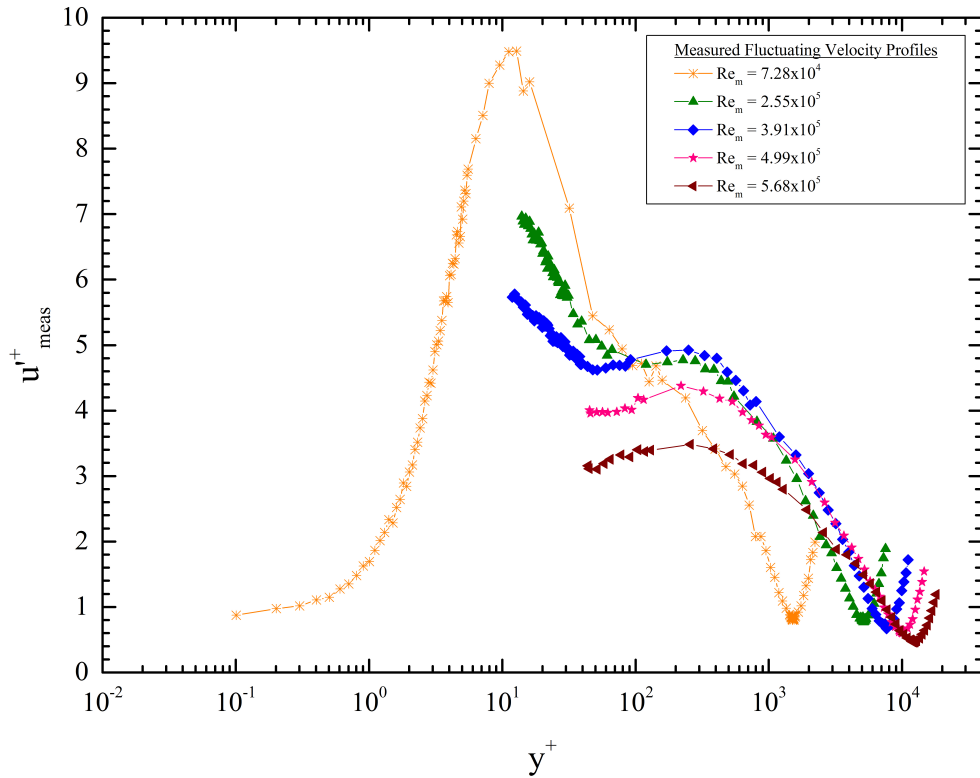


Figure 6.23: Overview of the raw fluctuating velocity profiles for different Re_m scaled by the wall friction velocity u_τ as a function of the normalized wall distance y^+ .

From Figure 6.23 the problematic situation is clear, which arises if an analysis and discussion of the profiles is aspired. The above criteria, recently discussed in certain publications, are obvious. At first, the inner peak approaches a maximum value for the lowest bulk-based Reynolds number and is therefore decreasing with increasing Re_m .

This is in contrast to the assumption that the inner peak is invariant with the Reynolds number [47]. Even deviant is the magnitude of the peak, which is in this case at around 9.5, for the lowest Reynolds number, respectively. The second case is the emergence of the so-called "outer peak" with increasing bulk-based Reynolds number. Here, it is clear from Figure 6.23 that this second outer peak becomes more present until it approaches a higher magnitude than the inner peak, i.e. for $Re_m = 4.99 \times 10^5$ and $Re_m = 5.68 \times 10^5$. A possible explanation for these concerns is the spatial and temporal resolution of the fluctuating velocity profiles as well as the possibility of the not negligible influence of the hot-wire length-to-diameter ratio. Here, the viscous scaled hot-wire length is determined to $l^+ = 251$, which exceeds the preferred value of $l^+ \leq 50 - 60$ proposed by Hutchins et al. [50]. Another very important reason, especially in the case of the CoLaPipe data sets, is, as already discussed in the chapter before, the estimation of the inner scaling parameter u_τ . This well-known problem is further discussed by the help of Figure 6.24, where for the bulk-based Reynolds number $Re_m = 7.28 \times 10^4$ seven fluctuating velocity profiles are depicted. The difference between the shown profiles is the estimation method for the wall friction velocity u_τ , refer to Chapter 6.4 for a detailed description of each method, which is in the recent study the suitable scaling parameter. For clearance the parameter variation is again listed in the following table and hence no further description for each velocity profile is presented within Figure 6.24.

Table 6.7: List of parameter variation for the estimation of the wall friction velocity u_τ . The table serves as additional information connected to Figure 6.24 and Figure 6.25.

Symbol/Color	Parameter Variation	wall friction velocity u_τ
Cross/Orange	Mean pressure gradient variation 1	0.226
Cross/Violet	Mean pressure gradient variation 2	0.246
Cross/Pink	Mean pressure gradient variation 3	0.255
Cross/Light Blue	Mean pressure gradient variation 4	0.286
Cross/Black	Mean pressure gradient variation 5	0.264
Cross/Blue	Viscous sublayer profile method	0.209
Cross/Olive	Clouser chart method	0.289

From Figure 6.24 the clear trend in the decreasing magnitude for the "inner peak" can be seen. This fact is due to the decreasing value of u_τ . If we consider the purple colored fluctuating velocity profile representing the second mean pressure gradient variation as the initial one, than the blue and orange colored fluctuating velocity profiles representing the first mean pressure gradient variation as well as the viscous sublayer profile method are overestimated. This means, that the magnitude is artificially increased due to a lower

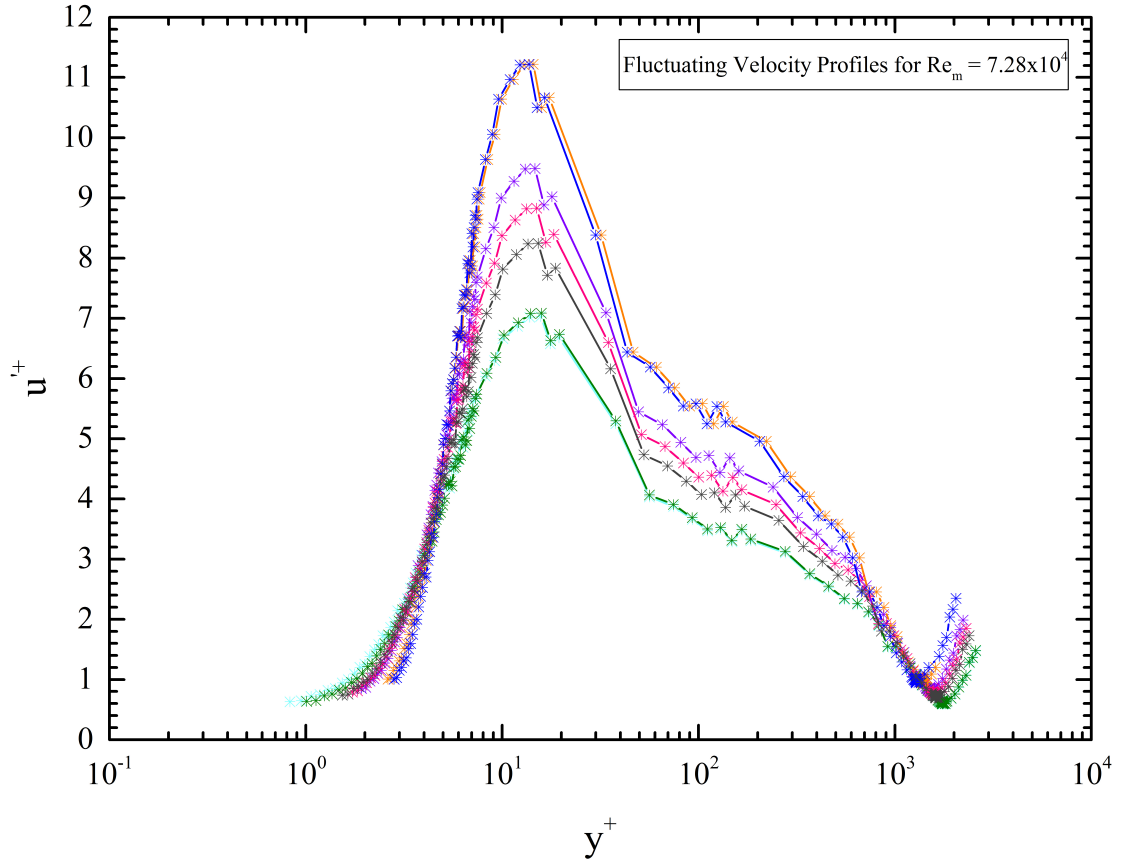


Figure 6.24: Overview of the influence of the wall friction velocity, when used as the appropriate scaling parameter, on the fluctuating velocity profile for the bulk-based Reynolds number $Re_m = 7.28 \times 10^4$. The nomenclature is denoted within Table 6.7.

value of the wall friction velocity u_τ . Nevertheless, the maximum value is found to occur at $y^+ \approx 15$. This is valid for all manipulated fluctuating velocity profiles represented in Figure 6.24, and even for the two intermediate Reynolds numbers ($Re_m = 2.55 \times 10^5$, $Re_m = 3.91 \times 10^5$) fluctuating velocity profiles, which are shown in Figure 6.23. For the higher bulk-based Reynolds numbers ($Re_m = 4.99 \times 10^5$, $Re_m = 5.68 \times 10^5$) this can not be clearly decided since no adequate resolution of the velocity profiles in the vicinity of the wall is available. The lower four fluctuating velocity profiles in Figure 6.24 show a decreasing magnitude of the "inner peak" with respect to an increasing value for the wall friction velocity u_τ . Here, it is very interesting to recognize that for the fifth mean pressure gradient variation the magnitude of the "inner peak" approaches the value of 8.24 at $y^+ = 15.25$, which is exactly the peak value for $\overline{u'^2}$ stated by Vallikivi et al. [98] within the estimated deviation. But this result has to be discussed critically due to the strong manipulation of the mean pressure gradient, which was done with the background of the highest convergence to the logarithmic law (refer to Chapter 6.4).

The second "outer peak" is not present for such low Reynolds numbers, which suggests

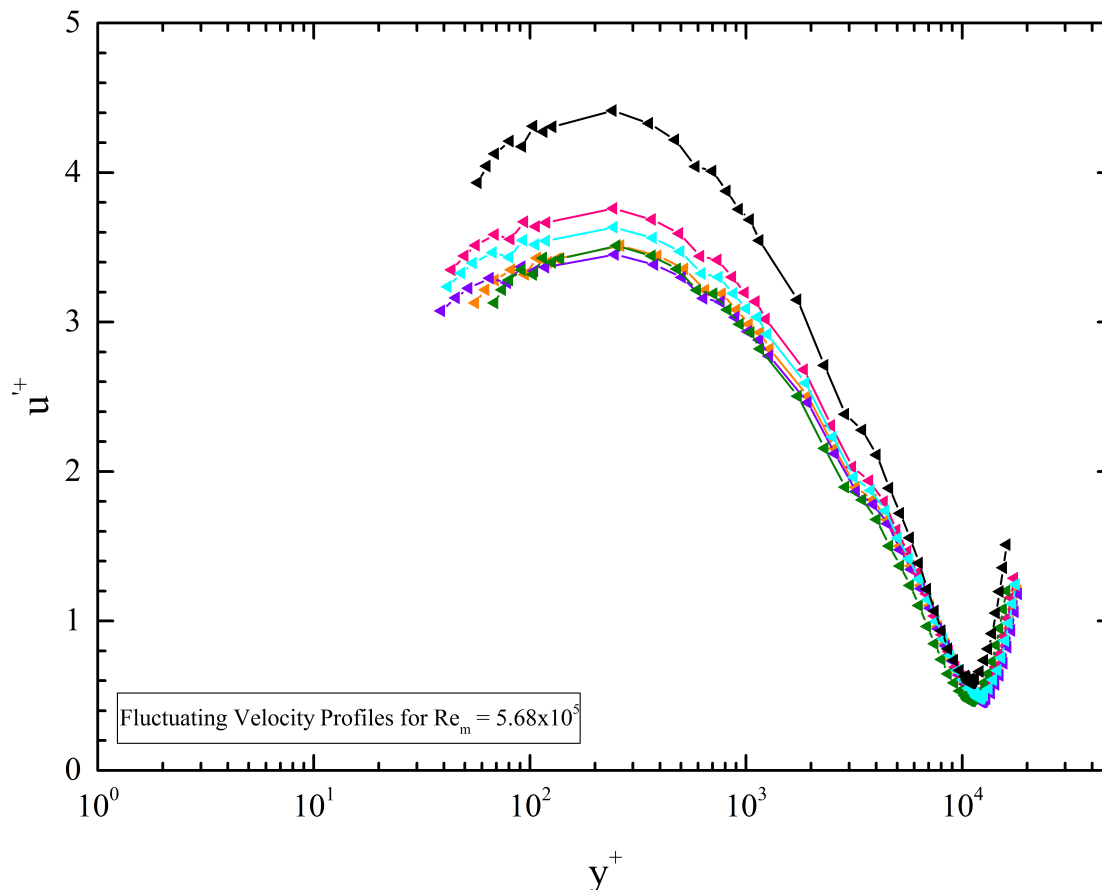


Figure 6.25: Overview of the influence of the wall friction velocity, when used as the appropriate scaling parameter, on the fluctuating velocity profile for the bulk-based Reynolds number $Re_m = 5.68 \times 10^5$. The nomenclature is denoted within Table 6.7.

itself to be a resolution problem in the case of high and very high Reynolds numbers. To conclude at this point the scaling behavior of the fluctuating velocity profiles for low Reynolds numbers depends strongly on the estimation of the wall friction velocity since this parameter is believed to be the correct scaling factor. Thus, no sufficient prediction of the magnitude of the "inner peak" is possible. Hence, according to this no further correction of the fluctuating velocity profiles is necessary. But if the fluctuating velocity profiles for higher Reynolds numbers are analyzed, the situation changes, which is presented graphically in Figure 6.25 for the bulk-based Reynolds number $Re_m = 5.68 \times 10^5$. Within Figure 6.25 the same manipulation of the fluctuating velocity profile as in Figure 6.24 is depicted, which is the different methods to calculate the wall friction velocity, here the variation of the mean pressure gradient as well as the application of the Clauser-Chart method. Not shown is the viscous sublayer profile method due to the missing data points within the linear part of the boundary layer. From this overview the strong influence on the magnitude of the second "outer peak" is detectable. The maximum is

approached for the fifth mean pressure gradient variation at a wall-normal position of $y^+ = 242$ and with a depending value for $u'^+ \approx 4.42$. This magnitude is decreasing with an increasing value of the wall friction velocity u_τ . It occurs in the absence of the "inner peak", because the location of this maximum is at $y^+ = 15$ in wall-normal direction, and this part of the velocity profile could not be resolved with the utilized measurement technique. If the results for the "outer peak" are compared with the fluctuating velocity profiles for $Re_m = 2.55 \times 10^5$ and $Re_m = 3.91 \times 10^5$ shown in Figure 6.23, where the "inner peak" is resolved, the position of the emerging second "outer peak" at $y^+ \approx 250$ is consistent. Nevertheless, Hutchins et al. [50] presented and described in detail, that this is an artifact due to the insufficient spatial ($l^+ \geq 50 - 60$) and temporal resolution.

6.7.1 Spatial Resolution Correction

With the justified doubts, which were raised since the detailed description of the spatial and temporal resolution issues claimed by Hutchins et al. [50], scientists tried to develop correction schemes to overcome the problem during post-processing. Here, a procedure is applied to the CoLaPipe data sets to reproduce the mechanism and, if possible, to draw a conclusion on it.

The utilized correction scheme is valid for wall-bounded turbulence measurements and was developed in 2011 by Smits et al. [93]. The basis builds the attached eddy hypothesis, wherewith insufficient spatially resolved measurement data can be manipulated to avoid filtering effects. A detailed description of the theory behind the rather simple function for the corrected fluctuating velocity $\overline{u'^2}_T$

$$\overline{u'^2}_T = [M(l^+)f(y^+) + 1]\overline{u'^2}_m, \quad (6.15)$$

can be found in [93]. Within Equation 6.15 the subscribed letters T represents the true value and m represents the measured value for the fluctuating velocity. The parameter $M(l^+)$ is a constant since it depends only on the viscous scaled wire length and $f(y^+)$ is a function representing the characteristic form based on the attached eddy hypothesis in wall-normal direction, like:

$$f(y^+) = \frac{15 + \ln(2)}{y^+ + \ln[e^{(15-y^+)} + 1]}. \quad (6.16)$$

Prior to the manipulation of the data sets using Equation 6.15 and Equation 6.16 one has to clarify if the measurement of the fluctuating velocity profile resolves the "inner

peak" at $y^+ = 15$ or if the spatial resolution is insufficient due to high or very high pipe flow Reynolds number. This plays an important role on the calculation of the constant $M(l^+)$. If the Reynolds number is low enough and $\overline{u'^2}_m|_{y^+ = 15}$ can be obtained with e.g. conventional hot-wire anemometry, $M(l^+)$ is calculated using this functional relationship:

$$M = \frac{\Delta \overline{u'^2}^+}{\overline{u'^2}_m} \Big|_{y^+ = 15} = \frac{A \tanh(\alpha l^+) \tanh(\beta l^+ - E)}{\overline{u'^2}_m} \Big|_{y^+ = 15}, \quad (6.17)$$

where $A = 6.13$, $\alpha = 5.6 \times 10^{-2}$, $\beta = 8.6 \times 10^{-3}$ and $E = -1.26 \times 10^{-2}$ are fitting parameters with no particular physical meaning [93]. But if $\overline{u'^2}_m|_{y^+ = 15}$ can not be obtained, e.g. due to high Reynolds number, one can use the regression fit [93]

$$M = 0.0091 l^+ - 0.069. \quad (6.18)$$

The above described correction scheme is now applied to the same data set, which is presented and discussed in Figure 6.23. The resulting fluctuating velocity profiles are similarly depicted in Figure 6.26. For the lower three Reynolds numbers, i.e. $Re_m = 7.28 \times 10^5$, $Re_m = 2.55 \times 10^5$ and $Re_m = 3.91 \times 10^5$, the constant $M(l^+)$ is calculated using Equation 6.17. Thereafter Equation 6.15 and 6.16 are applied onto the data to entirely manipulate the profiles. The high Reynolds number fluctuating velocity profiles ($Re_m = 4.99 \times 10^5$, $Re_m = 5.68 \times 10^5$) are corrected by the application of Equation 6.18 as well as Equation 6.15 and Equation 6.16. It is obvious from Figure 6.26 that the second "outer peak" disappears, and that the profiles collapse onto a single curve for $15 \leq y^+ \leq 50$. The maximum value of the "inner peak" is invariant with the Reynolds number and can be determined to be $\overline{u'^2}_T = 9.25$.

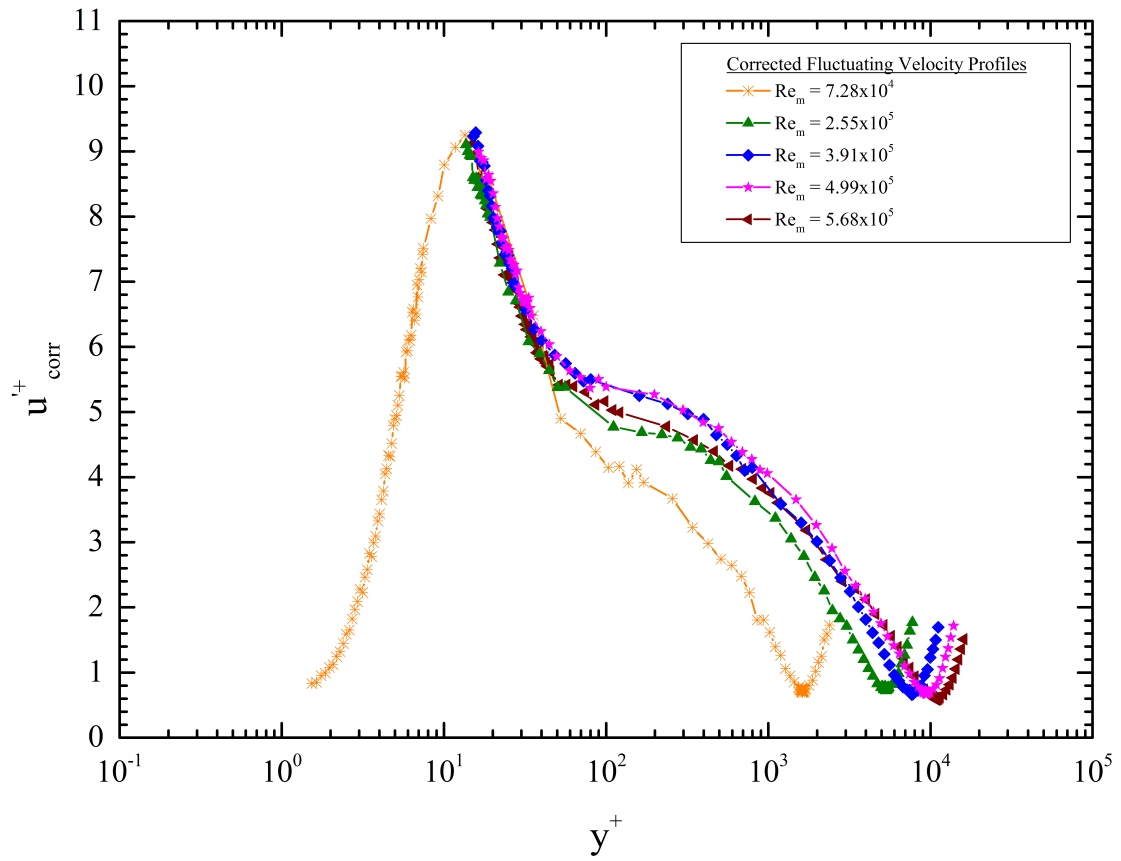


Figure 6.26: Overview of the corrected fluctuating velocity profiles for different bulk-based Reynolds numbers scaled by the wall friction velocity u_τ as a function of the normalized wall distance y^+ .

7 Summary and Outlook

7.1 Summary

Within this thesis a novel experiment concerning pipe flow is presented. The focus during the first two chapters is on the motivation of designing such a new high Reynolds number pipe test facility and the preliminary results as well as a detailed review on more than 100 years of research on this topic. Here, the differentiation between low, intermediate, high and very high Reynolds number experiments is discussed and an unambiguous assignment for the CoLaPipe can be established. Therewith the CoLaPipe is among high and very high Reynolds numbers and can be considered as a contributor beside the established *SuperPipe*. It can also be treated as a bridge until the finish of the CICLoPE facility.

The presented experimental setup with its novelty is successfully introduced, which shows even the publication in a well known journal:

Franziska Koenig, El-Sayed Zanoun, Emir Oenguener and Christoph Egbers
The CoLaPipe - The new Cottbus Large Pipe Test Facility at Brandenburg
University of Technology Cottbus-Senftenberg
Review of Scientific Instruments 85, 075115 (2014) [54].

It also contributes the scientific discussion on the field of pipe flow. With the improved spatial and temporal resolution related to the *Princeton SuperPipe* the CoLaPipe provides measurement data, which are interesting and in some cases necessary for planned and also existing pipe test facilities, e.g. the influence of the development length. Here, one conclusion is that, in contrast to the general assumption, no effort is achieved by triggering pipe flow artificially. This means, that the development length for the flow, which is needed to develop full turbulence in such a wall-bounded flow system, can not be sufficiently decreased. This fact is intensively discussed in Chapter 6.2 and Chapter 6.3. The presented experimental results are also important concerning common theories re-

garding the scaling behavior of the mean flow as well as the fluctuating velocity profiles, which are discussed in Chapter 6.4ff.. The main results on this can be summarized as follows:

1. Great attention has to be paid on the estimation of the inner scaling parameter: the wall friction velocity u_τ . Hence, different methods are available, some are direct and other are indirect methods, to measure or to calculate this parameter. For the recent results presented within this thesis, the strong manipulation of the mean pressure gradient method shows the best results with respect to the logarithmic law and the used constants proposed by von Kármán [99].
2. The other presented methods, like the viscous sublayer profile method or the Clauser-Chart method, under- or overestimate the calculated value for the wall friction velocity u_τ . Thus, a strong deviation of these scaled mean velocity profiles from the logarithmic law are obtained.
3. The magnitude of the "inner peak" within the fluctuating velocity profiles decrease with increasing Reynolds number, when they are not corrected. Hence, no invariant behavior with respect to the Reynolds number is obtained.
4. Without the manipulation of the fluctuating velocity profiles the so-called second "outer peak" emerges.
5. If an correction scheme is applied onto the data sets two results are achieved:
 - The magnitude of the "inner peak" becomes invariant with the Reynolds number.
 - The "outer peak" disappears based on the attached eddy hypothesis.

7.2 Outlook

The knowledge about pipe flow is broad, but we know from this thesis and from other scientific work ([7, 54, 61]) that not all mechanisms are fully understood. But to contribute engineering work and to improve the utilization of piping systems in varying technical applications it is one great goal to resolve the dynamics within such a simple flow geometry like pipe flow. Hence, the future work at the CoLaPipe should be a more detailed investigation on the scaling behavior of mean and fluctuation velocity

with improved measurement techniques. Here the novel nano-scale thermal anemometry (NSTAP) developed by Vallikivi et al. [98] can be helpful. But also LDA and PIV, in a high-speed mode, can yield the desired goal.

Another important fact, which could not be investigated within the recent work, is the discovery of the structural behavior within this wall-bounded flow system. The existence of the so-called large scale (LSM) and very large scale motions (VLSM), already reported by Kim and Adrian [53] and [92], respectively, is proved. But structures and patterns are although not fully uncovered much less understood. To support such important investigations with the CoLaPipe some preliminary results are obtained and presented by Öngüner et al. [73]. Nevertheless, a different arrangement of the measurement technique has to be approached due to the necessity of collecting velocity information in stream-wise and spanwise direction as well as in azimuthal direction to completely resolve the large and very large scale motions. Hence, the solution can be the utilization of x-wire probes to measure u_x and u_r and the distribution around the circumference to collect information about the azimuthal dependence. The following figures show such possible rearrangements of three x-wire HWA probes.

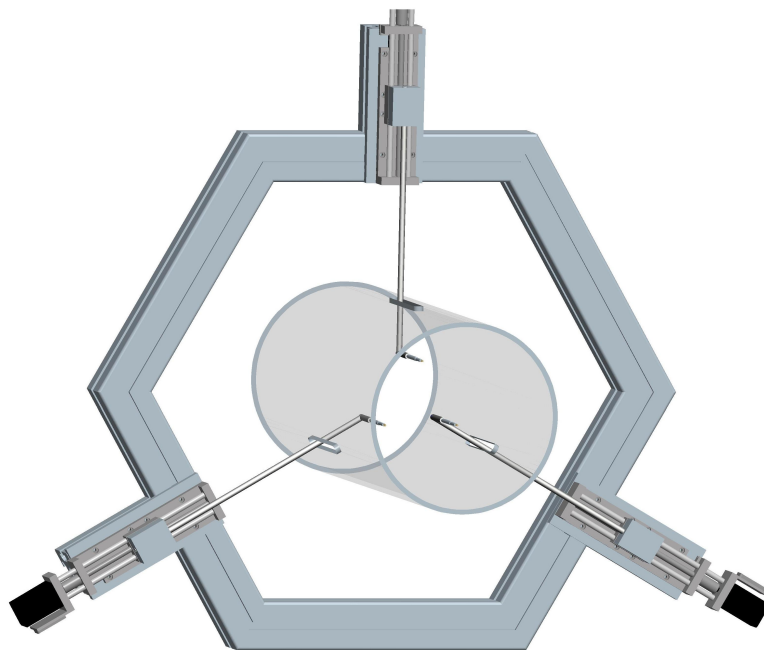


Figure 7.1: Possible arrangement of three x-wire HWA probes with probe support around the circumference of the test section.

To further support the efforts on the correction of the partly insufficiently resolved fluctuating velocity profiles, investigations on different sensor lengths and hence an improved l^+ should be tasked. Though, the Reynolds number should be matched to guaranty a

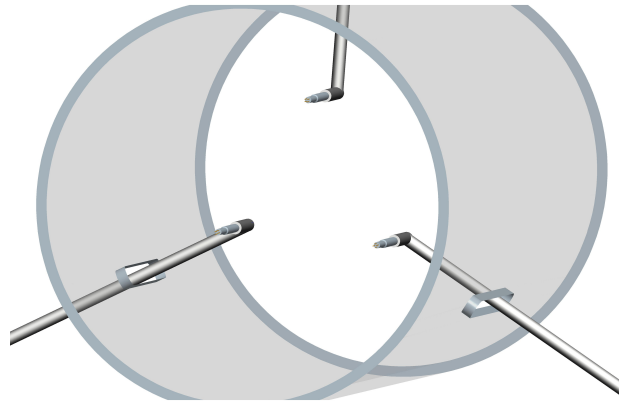


Figure 7.2: Detailed view on the HWA probe arrangement with visible accesses to the test section.

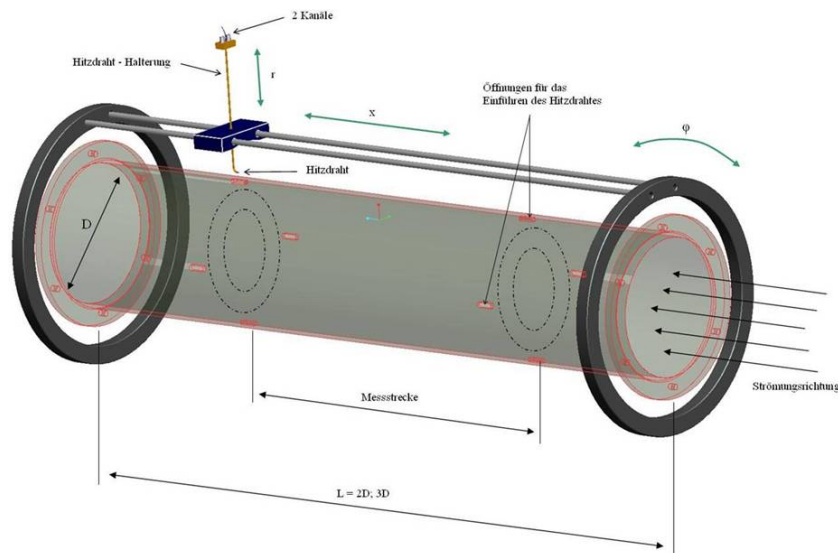


Figure 7.3: Alternative HWA probe arrangement using a special equipped part of the pipe test section.

high-quality comparison. It is even possible with this unique pipe test facility to study in a broader range the influence of different boundary conditions on the behavior of wall-bounded pipe flow. Thus, a comparison between hydraulically smooth and rough surfaces can be one aim. The development of artificial transition mechanisms can also be helpful to possibly decrease the development length of pipe flow. At the end I want to draw the interest on the development of innovative measurement technique, like nano-scale thermal anemometry (NSTAP), for which the CoLaPipe test facility is predestined due to the optical accessibility to the facility itself and the possibility to utilize the return line of the CoLaPipe, which has an improved spatial resolution.

Bibliography

- [1] P. H. Alfredsson, R. Örlü, and P. Schlatter. The viscous sublayer revisited—exploiting self-similarity to determine the wall position and friction velocity. *Experiments in Fluids*, 51(1):271–280, 2011.
- [2] P. H. Alfredsson, A. Segalini, and R. Örlü. A new scaling for the streamwise turbulence intensity in wall-bounded turbulent flows and what it tells us about the "outer" peak. *Physics of Fluids*, 23(4), 2011.
- [3] AMES Research Staff. Equations, tables, and charts for compressible flows. Technical report, National Advisory Committee for Aeronautics, 1953.
- [4] K. Avila, D. Moxey, A. de Lozar, M. Avila, D. Barkley, and B. Hof. The onset of turbulence in pipe flow. *Science*, 333(192):192 – 196, 2011.
- [5] M. Avila, A. P. Willis, and B. Hof. On the transient nature of localized pipe flow turbulence. *Journal of Fluid Mechanics*, 646(-1):10, 2010.
- [6] S. C. C. Bailey and A. J. Smits. Experimental investigation of the structure of large- and very-large-scale motions in turbulent pipe flow. *Journal of Fluid Mechanics*, 651:339–356, 2010.
- [7] S.C.C. Bailey, M. Vallikivi, M. Hultmark, and A.J. Smits. Estimating the value of von Kármán's constant in turbulent pipe flow. *Journal of Fluid Mechanics*, 749: 79–98, 2014.
- [8] B. J. Balakumar and R. J. Adrian. Large- and very-large-scale motions in channel and boundary-layer flows. *Philosophical Transactions of the Royal Society A*, 365: 17, 2007.
- [9] G. I. Barenblatt. Scaling laws for fully developed turbulent shear flows. part 1. basic hypotheses and analysis. *Journal of Fluid Mechanics*, 248:513–520, 1993.
- [10] G. I. Barenblatt, A. J. Chorin, and V. M. Prostokishin. Scaling laws for fully developed turbulent flow in pipes: Discussion of experimental data. *Proceedings*

- of the National Academy of Sciences of the United States of America, 94:773–776, 1997.
- [11] G. K. Batchelor. *An Introduction to Fluid Mechanics*. Cambridge Mathematical Library. Cambridge University Press, 2002.
- [12] J. H. Bell and R. D. Mehta. Boundary-layer predictions for small low-speed contractions. *American Institute of Aeronautics and Astronautics, Inc. - AIAA*, 27(3):372 – 374, 1989.
- [13] J. C. Bhatia, F. Durst, and J. Jovanovic. Corrections of hot-wire anemometer measurements near walls. *Journal of Fluid Mechanics*, 122:411–431, 1982.
- [14] H. Blasius. The Boundary Layers in Fluids with little Friction - Translation of "Grenzschichten in Flüssigkeiten mit kleiner Reibung". *Zeitschrift für Mathematik und Physik*, 56(1), 1908.
- [15] P. Bradshaw and R. C. Pankhurst. The design of low-speed wind tunnels. *Progress in Aerospace Sciences*, 5(0):1–69, 1964. doi: 10.1016/0376-0421(64)90003-X.
- [16] H. H. Bruun, M. A. Khan, H. H. Al-Kayiem, and A. A. Fardad. Velocity calibration relationships for hot-wire anemometry. *Journal of Physics E: Scientific Instruments*, 21:8, 1988.
- [17] J. Cohen and N. J. B. Ritchie. Low-Speed Three-Dimensional Contraction Design. *Journal of the Royal Aeronautical Society*, 66:231 – 236, 1962.
- [18] D. Coles. The law of the wake in the turbulent boundary layer. *Journal of Fluid Mechanics*, 1(02):191–226, 1956.
- [19] A. G. Darbyshire and T. Mullin. Transition to turbulence in constant-mass-flux pipe flow. *Journal of Fluid Mechanics*, 289(-1):83–114, 1995.
- [20] A. de Lozar and B. Hof. An experimental study of the decay of turbulent puffs in pipe flow. *Philosophical Transactions of the Royal Society A: Mathematical, Physical and Engineering Sciences*, 367(1888):589–599, 2009.
- [21] J. M. J. den Toonder and F. T. M. Nieuwstadt. Reynolds number effects in a turbulent pipe flow for low to moderate Re. *Physics of Fluids*, 9(11):3398–3409, 1997.
- [22] J. Doherty, P. Ngan, J. P. Monty, and M. S. Chong. The development of turbulent pipe flow. In *16th Australasian Fluid Mechanics Conference*, 2007.

-
- [23] F. Durst, E.-S. Zanoun, and M. Passtrapanska. In Situ Calibration of Hot-Wires close to Highly Heatconducting Walls. *Exp. Fluids*, 31:8, 2001.
- [24] F. Durst, S. Ray, Bülent Ünsal, and O. Bayoumi. The Development Lengths of Laminar Pipe and Channel Flows. *Transactions of the A.S.M.E.*, 127:7, 2005.
- [25] B. Eckhardt. Turbulence transition in pipe flow: some open questions. *Nonlinearity*, 21(1), 2008.
- [26] B. Eckhardt. Introduction. Turbulence transition in pipe flow: 125th anniversary of the publication of Reynolds' paper. *Philosophical Transactions of the Royal Society A: Mathematical, Physical and Engineering Sciences*, 367(1888):449–455, 2009.
- [27] J. G. M. Eggels, F. Unger, M. H. Weiss, J. Westerweel, R. J. Adrian, R. Friedrich, and F. T. M. Nieuwstadt. Fully developed turbulent pipe flow: a comparison between direct numerical simulation and experiment. *Journal of Fluid Mechanics*, 268:35, 1994.
- [28] H. Faisst and B. Eckhardt. Traveling Waves in Pipe Flow. *Physical Review Letters*, 91(22):224502, 2003.
- [29] H. Faisst and B. Eckhardt. Sensitive dependence on initial conditions in transition to turbulence in pipe flow. *Journal of Fluid Mechanics*, 504:10, 2004.
- [30] M. Fischer. *Turbulente Wandgebundene Strömungen bei kleinen Reynoldszahlen*. PhD thesis, Universität Erlangen-Nürnberg, 1999.
- [31] M. Friedmann, J. Gillis, and N. Liron. LAMINAR FLOW IN A PIPE AT LOW AND MODERATE REYNOLDS NUMBERS. *Applied Scientific Research*, 19(1): 426–438, 1968.
- [32] W. K. George. Is there a universal log law for turbulent wall-bounded flows? *Philosophical Transactions of the Royal Society A: Mathematical, Physical and Engineering Sciences*, 365(1852):789–806, 2007.
- [33] J. Groth and A. V. Johansson. Turbulence reduction by screens. *Journal of Fluid Mechanics*, 197:139–155, 1988.
- [34] J. M. Hamilton, J. Kim, and F. Waleffe. Regeneration mechanisms of near-wall turbulence structures. *Journal of Fluid Mechanics*, 287(-1):317–348, 1995.
- [35] H. Herwig, D. Gloss, and T. Wenterodt. A new approach to understanding and modelling the influence of wall roughness on friction factors for pipe and channel flows. *Journal of Fluid Mechanics*, 613:35–53, 2008.

-
- [36] B. Hof, A. Juel, and T. Mullin. Scaling of the Turbulence Transition Threshold in a Pipe. *Physical Review Letters*, 91(24):4, 2003.
- [37] B. Hof, C. W. H. van Doorne, J. Westerweel, F. T. M. Nieuwstadt, H. Faisst, B. Eckhardt, H. Wedin, R. R. Kerswell, and F. Waleffe. Experimental Observation of Nonlinear Traveling Waves in Turbulent Pipe Flow. *Science*, 305:6, 2004.
- [38] B. Hof, C. W. H. van Doorne, J. Westerweel, and F. T. M. Nieuwstadt. Turbulence Regeneration in Pipe Flow at Moderate Reynolds Numbers. *Physical Review Letters*, 95(21):4, 2005.
- [39] B. Hof, J. Westerweel, T. M. Schneider, and B. Eckhardt. Finite lifetime of turbulence in shear flows. *Nature*, 443(7):4, 2006.
- [40] B. Hof, A. de Lozar, D. J. Kuik, and J. Westerweel. Repeller or Attractor? Selecting the Dynamical Model for the Onset of Turbulence in Pipe Flow. *Physical Review Letters*, 101(214501):4, 2008.
- [41] B. Hof, A. de Lozar, M. Avila, X. Tu, and T. M. Schneider. Eliminating Turbulence in Spatially Intermittent Flows. *Science*, 327:4, 2010.
- [42] J.P. Holman. *Experimental methods for engineers*, volume 7. Boston : McGraw-Hill, 2001.
- [43] R. W. Hornbeck. Laminar flow in the entrance region of a pipe. *Applied Scientific Research*, 13(1):224–232, 1964.
- [44] S. Hoyas and J. Jiménez. Scaling of the velocity fluctuations in turbulent channels up to $Re_\tau = 2003$. *Physics of Fluids*, 18(1):–, 2006.
- [45] L. M. Huang and T. S. Chen. Stability of the developing laminar pipe flow. *Phys. Fluids*, 17:3, 1973.
- [46] M. Hultmark. A theory for the streamwise turbulent fluctuations in high Reynolds number pipe flow. *Journal of Fluid Mechanics*, 707:575–584, 2012.
- [47] M. Hultmark, S. C. C. Bailey, and A. J. Smits. Scaling of near-wall turbulence in pipe flow. *Journal of Fluid Mechanics*, 649(-1):103–113, 2010.
- [48] M. Hultmark, M. Vallikivi, S. C. C. Bailey, and A. J. Smits. Logarithmic scaling of turbulence in smooth- and rough-wall pipe flow. *Journal of Fluid Mechanics*, 728:376–395, 2013.
- [49] A. K. M. F. Hussain and Y. Ramjee. Effects of the Axisymmetric Contraction Shape on Incompressible Turbulent Flow. *Journal of Fluids Engineering*, 1976.

-
- [50] N. Hutchins, T. B. Nickels, I. Marusic, and M. S. Chong. Hot-wire spatial resolution issues in wall-bounded turbulence. *Journal of Fluid Mechanics*, 635(-1):103–136, 2009.
- [51] G. Janke. Hot wire in wall proximity. In *Advances in Turbulence*. Springer, Berlin, 1987.
- [52] J. Kim, P. Moin, and R. Moser. Turbulence statistics in fully developed channel flow at low Reynolds number. *Journal of Fluid Mechanics*, 177(-1):133–166, 1987.
- [53] K. C. Kim and R. J. Adrian. Very large-scale motion in the outer layer. *Physics of Fluids*, 11, 1999.
- [54] F. König, E. S. Zanoun, E. Öngüner, and C. Egbers. The CoLaPipe - The new Cottbus Large Pipe Test Facility at Brandenburg University of Technology Cottbus-Senftenberg. *Review of Scientific Instruments*, 85:075115, 2014.
- [55] H.-P. Kreplin and H. Eckelmann. Behavior of the three fluctuating velocity components in the wall region of a turbulent channel flow. *Physics of Fluids (1958-1988)*, 22(7):1233–1239, 1979.
- [56] L. V. Krishnamoorthy, D. H. Wood, R. A. Antonia, and A. J. Chambers. Effect of wire diameter and overheat ratio near a conducting wall. *Experiments in Fluids*, 3(3):121–127, 1985.
- [57] J. Laufer. The structure of turbulence in fully developed pipe flow. Technical Report 1174, National Bureau of Standards, 1953.
- [58] J. D. Li, B. J. McKeon, W. Jiang, J. F. Morrison, and A. J. Smits. The response of hot wires in high Reynolds-number turbulent pipe flow. *Measurement Science and Technology*, 15(5):789, 2004.
- [59] R. I. Loehrke and H. M. Nagib. Control of Free-Stream Turbulence by Means of Honeycombs: A Balance Between Suppression and Generation. *Journal of Fluids Engineering*, 98(3):342–351, 1976.
- [60] N. N. Mansour, J. Kim, and P. Moin. Reynolds-stress and dissipation-rate budgets in a turbulent channel flow. *Journal of Fluid Mechanics*, 194:15–44, 1988.
- [61] I. Marusic, B. J. McKeon, P. A. Monkewitz, H. M. Nagib, A. J. Smits, and K. R. Sreenivasan. Wall-bounded turbulent flows at high Reynolds numbers: Recent advances and key issues. *Physics of Fluids*, 22(6):065103, 2010.
- [62] I. Marusic, J. P. Monty, M. Hultmark, and A. J. Smits. On the logarithmic region in wall turbulence. *Journal of Fluid Mechanics*, 716, 2013.

-
- [63] B. J. McKeon. *HIGH REYNOLDS NUMBER TURBULENT PIPE FLOW*. PhD thesis, Princeton, 2003.
- [64] B. J. McKeon and A. J. Smits. Static pressure correction in high Reynolds number fully developed turbulent pipe flow. *Measurement Science and Technology*, 13: 1608–1614, 2002.
- [65] B. J. McKeon, J. Li, W. Jiang, J. F. Morrison, and A. J. Smits. Further observations on the mean velocity distribution in fully developed pipe flow. *Journal of Fluid Mechanics*, 501:135–147, 2004.
- [66] B. J. McKeon, C. J. Swanson, M. V. Zagarola, R. Donnelly, and A. J. Smits. Friction factors for smooth pipe flow. *Journal of Fluid Mechanics*, 511:4, 2004.
- [67] B. J. McKeon, M. V. Zagarola, and A. J. Smits. A new friction factor relationship for fully developed pipe flow. *Journal of Fluid Mechanics*, vol. 538:14, 2005.
- [68] C.B. Millikan. A critical discussion of turbulent flows in channels and circular tubes. In *Proceedings of the fifth International Congress for Applied Mechanics*, Harvard University and the Massachusetts Institute of Technology, Cambridge, Massachusetts, 1938.
- [69] J. P. Monty. *Developments In Smooth Wall Turbulent Duct Flows*. PhD thesis, Melbourne, 2005.
- [70] T. Morel. Comprehensive Design of Axisymmetric Wind Tunnel Contractions. *Journal of Fluids Engineering*, 1975.
- [71] J. F. Morrison, B. J. McKeon, W. Jiang, and A. J. Smits. Scaling of the streamwise velocity component in turbulent pipe flow. *Journal of Fluid Mechanics*, 508:99–131, 2004.
- [72] H. M. Nagib and K. A. Chauhan. Variations of von Kármán coefficient in canonical flows. *Physics of Fluids*, 20(10):101518, 2008.
- [73] E. Öngüner, E.-S. Zanoun, and Ch. Egbers. Turbulent Pipe Flow Investigations at High Reynolds Numbers. In *EFMC10 - 10th Euromech Fluid Mechanics Conference*, 14-18.09.2014.
- [74] J. Nikuradse. Gesetzmäßigkeiten der turbulenten Strömung in glatten Röhren. *VDI Forschungsheft*, 356, 1932.
- [75] J. Nikuradse. Strömungsgesetze in rauen Röhren. *VDI Forschungsheft*, 361, 1933.

-
- [76] Mi. Nishi, B. Ünsal, F. Durst, and G. Biswas. Laminar-to-turbulent transition of pipe flows through puffs and slugs. *Journal of Fluid Mechanics*, 614(-1):425–446, 2008.
- [77] W. Nitsche and A. Brunn. *Strömungsmesstechnik*. Springer, 2006.
- [78] V. C. Patel and M. R. Head. Some observations on skin friction and velocity profiles in fully developed pipe and channel flows. *Journal of Fluid Mechanics*, 38(01):181–201, 1969.
- [79] J. Peixinho and T. Mullin. Decay of Turbulence in Pipe Flow. *Physical Review Letters*, 96(9):094501, 2006.
- [80] A. E. Perry and C. J. Abell. Scaling laws for pipe-flow turbulence. *Journal of Fluid Mechanics*, 67(02):257–271, 1975.
- [81] A. E. Perry, S. Hafez, and M. S. Chong. A possible reinterpretation of the Princeton superpipe data. *Journal of Fluid Mechanics*, 439(-1):395–401, 2001.
- [82] J. Philip and J. Cohen. Formation and decay of coherent structures in pipe flow. *Journal of Fluid Mechanics*, 655(-1):258–279, 2010.
- [83] S. B. Pope. *Turbulent Flows*. Cambridge University Press, 2013.
- [84] L. Prandtl and A. Betz. *Ergebnisse der Aerodynamischen Versuchsanstalt zu Göttingen IV. Lieferung*. Göttinger Klassiker der Strömungsmechanik Bd. 7. Rein, M., Göttingen, 1932.
- [85] O. Reynolds. An Experimental Investigation of the Circumstances Which Determine Whether the Motion of Water Shall Be Direct or Sinuous, and of the Law of Resistance in Parallel Channels. *Philosophical Transactions of the Royal Society of London*, 174:935–982, 1883.
- [86] R. Örlü and P. Alfredsson. On spatial resolution issues related to time-averaged quantities using hot-wire anemometry. *Experiments in Fluids*, 49(1):101–110, 2010.
- [87] R. Örlü and P. H. Alfredsson. Comment on the scaling of the near-wall streamwise variance peak in turbulent pipe flows. *Experiments in Fluids*, 54(1):1–5, 2012.
- [88] R. Örlü, J. H. M. Fransson, and H. P. Alfredsson. On near wall measurements of wall bounded flows - The necessity of an accurate determination of the wall position. *Progress in Aerospace Sciences*, 46(8):353–387, 2010.
- [89] J. Rotta. Experimenteller Beitrag zur Entstehung turbulenter Strömung im Rohr. *Archiv of Applied Mechanics*, 24(4):258–281, 1956.

-
- [90] K. Schlichting, H. und Gersten. *Grenzschicht-Theorie*. Springer-Verlag, Berlin, Heidelberg, 2006.
- [91] M. A. Shockling, J. J. Allen, and A. J. Smits. Roughness effects in turbulent pipe flow. *Journal of Fluid Mechanics*, 564(-1):267–285, 2006.
- [92] A. J. Smits, B. J. McKeon, and I. Marusic. High-reynolds number wall turbulence. *Annual Review of Fluid Mechanics*, 43(1):25, 2010.
- [93] A. J. Smits, J. Monty, M. Hultmark, S. C. C. Bailey, N. Hutchins, and I. Marusic. Spatial resolution correction for wall-bounded turbulence measurements. *Journal of Fluid Mechanics*, 676:41–53, 2011.
- [94] K. R. Sreenivasan and R. A. Antonia. Properties of Wall Shear Stress Fluctuations in a Turbulent Duct Flow. *Journal of Applied Mechanics*, 44:389 – 395, 1977.
- [95] J. M. Österlund, A. V. Johansson, and H. M. Nagib. Comment on “A note on the intermediate region in turbulent boundary layers”. *Physics of Fluids*, 12(9): 2360–2363, 2000.
- [96] A. Talamelli, F. Persiani, J. H. M. Fransson, P. H. Alfredsson, A. V. Johansson, H. M. Nagib, J.-D. Ruedi, K. R. Sreenivasan, and P.A. Monkewitz. CICLoPE - a response to the need for high Reynolds number experiments. *Fluid Dynamics Research*, 41:22, 2009.
- [97] C. Tropea, A. C. Yarin, and J. F. Foss. *Handbook of Experimental Fluid Mechanics*. Springer, 2007.
- [98] M. Vallikivi, M. Hultmark, S. Bailey, and A. Smits. Turbulence measurements in pipe flow using a nano-scale thermal anemometry probe. *Experiments in Fluids*, 51(6):1521–1527, 2011.
- [99] Th. von Kármán. Mechanische Ähnlichkeit und Turbulenz. *Nachrichten von der Gesellschaft der Wissenschaften zu Göttingen, Fachgruppe 1 (Mathematik)*, 5:58–76, 1930.
- [100] F. Waleffe. On a self-sustaining process in shear flows. *Physics of Fluids*, 9:18, 199.
- [101] F. Waleffe. Three-Dimensional Coherent States in Plane Shear Flows. *Physical Review Letters*, 81(19):4140–4143, 1998.
- [102] F. Waleffe. Exact coherent structures in channel flow. *Journal of Fluid Mechanics*, 435:93–102, 2001.

-
- [103] F. Waleffe. Homotopy of exact coherent structures in plane shear flows. *Physics of Fluids*, 15(6):1517–1534, 2003.
- [104] H. Wedin and R. R. Kerswell. Exact coherent structures in pipe flow: travelling wave solutions. *Journal of Fluid Mechanics*, 508:39, 2004.
- [105] A. P. Willis and R. R. Kerswell. Critical Behavior in the Relaminarization of Localized Turbulence in Pipe Flow. *Physical Review Letters*, 98(1):014501, 2007.
- [106] X. Wu and P. Moin. A direct numerical simulation study on the mean velocity characteristics in turbulent pipe flow. *Journal of Fluid Mechanics*, 608(-1):81–112, 2008.
- [107] I. J. Wygnanski and F. H. Champagne. On transition in a pipe. Part 1. The origin of puffs and slugs and the flow in a turbulent slug. *Journal of Fluid Mechanics*, 59(02):281–335, 1973.
- [108] M. V. Zagarola. *Mean-flow scaling of turbulent pipe flow*. PhD thesis, Princeton, 1996.
- [109] M. V. Zagarola and A. J. Smits. Scaling of the Mean Velocity Profile for Turbulent Pipe Flow. *Physical Review Letters*, 78:239–242, 1997.
- [110] M. V. Zagarola and A. J. Smits. Mean-flow scaling of turbulent pipe flow. *Journal of Fluid Mechanics*, 373:33–79, 1998.
- [111] M. V. Zagarola and A. J. Smits. A new mean velocity scaling for turbulent boundary layers. In *1998 ASME Fluids Engineering Division Summer Meeting*, 1998.
- [112] M. V. Zagarola, A. E. Perry, and A. J. Smits. Log laws or power laws: The scaling in the overlap region. *Physics of Fluids*, 9(7):7, 1997.
- [113] E.-S. Zanoun. *Answers to Some Open Questions in Wall-Bounded Laminar and Turbulent Shear Flows*. PhD thesis, Erlangen-Nürnberg, 2003.
- [114] E. S. Zanoun and F. Durst. Evaluating the law of the wall in two-dimensional fully developed turbulent channel flows. *Physics of Fluids*, 15(10):11, 2003.
- [115] E. S. Zanoun, F. Durst, and J. M. Shi. The physics of heat transfer from hot wires in the proximity of walls of different materials. *International Journal of Heat and Mass Transfer*, 52(15-16):3693–3705, 2009.
- [116] E.-S. Zanoun, M. Kito, and C. Egbers. A Study on Flow Transition and Development in Circular and Rectangular Ducts. *Journal of Fluids Engineering*, 131(6):10, 2009.

-
- [117] F. Zimmer, E. S. Zanoun, and C. Egbers. A study on the influence of triggering pipe on regarding mean and higher order statistics. *Journal of Physics: Conference Series*, 318(3), 2011.